Fast frontend electronics for high rate particle detectors

Dissertation

submitted to attain the academic degree
"Doctor of Natural Sciences"
at the Department of Physics, Mathematics and Computer Science of the Johannes Gutenberg University Mainz

Matteo Cardinali
born in Perugia, Italy

Mainz, 2015

Fast frontend electronics for high rate particle detectors[1]
Matteo Cardinali
PhD defence: July 10, 2015

[1] Angabe D77

[...] *"Humana ante oculos foede cum vita iaceret*
in terris oppressa gravi sub religione,
quae caput a caeli regionibus ostendebat
horribili super aspectu mortalibus instans,
primum Graius homo mortalis tollere contra
est oculos ausus primusque obsistere contra;
quem neque fama deum nec fulmina nec minitanti
murmure compressit caelum, sed eo magis acrem
inritat animi virtutem, effringere ut arta
naturae primus portarum claustra cupiret.
Ergo vivida vis animi pervicit et extra
processit longe flammantia moenia mundi
atque omne immensum peragravit mente animoque,
unde refert nobis victor quid possit oriri,
quid nequeat, finita potestas denique cuique
qua nam sit ratione atque alte terminus haerens.
Quare religio pedibus subiecta vicissim
opteritur, nos exaequat victoria caelo." [...]

Lucrezio, *De Rerum Natura*, 62-80.

Abstract

Future experiments in nuclear and particle physics are moving towards the high luminosity regime in order to access rare processes. In this framework, particle detectors require high rate capability together with excellent timing resolution for precise event reconstruction. In order to achieve this, the development of dedicated FrontEnd Electronics (FEE) for detectors has become increasingly challenging and expensive. Thus, a current trend in R&D is towards flexible FEE that can be easily adapted to a great variety of detectors, without impairing the required high performance.

This thesis reports on a novel FEE for two different detector types: imaging Cherenkov counters and plastic scintillator arrays. The former requires high sensitivity and precision for detection of single photon signals, while the latter is characterized by slower and larger signals typical of scintillation processes.

The FEE design was developed using high-bandwidth preamplifiers and fast discriminators which provide Time-over-Threshold (ToT). The use of discriminators allowed for low power consumption, minimal dead-times and self-triggering capabilities, all fundamental aspects for high rate applications. The output signals of the FEE are readout by a high precision TDC system based on FPGA. The performed full characterization of the analogue signals under realistic conditions proved that the ToT information can be used in a novel way for charge measurements or walk corrections, thus improving the obtainable timing resolution. Detailed laboratory investigations proved the feasibility of the ToT method. The full readout chain was investigated in test experiments at the Mainz Microtron: high counting rates per channel of several MHz were achieved, and a timing resolution of better than 100 ps after walk correction based on ToT was obtained. Ongoing applications to fast Time-of-Flight counters and future developments of FEE have been also recently investigated.

Zusammenfassung

Zukünftige Experimente in der Kern- und Teilchenphysik streben immer höhere Luminositäten an, um Zugang zu seltenen Prozessen zu erhalten. Unter diesen Bedingungen müssen Teilchendetektoren in der Lage sein, hohe Ereignisraten zu verkraften, sowie eine exzellente Zeitauflösung zur präzisen Ereignisrekonstruktion erzielen. Die Entwicklung spezieller Frontend-Elektronik (FEE) für Detektoren ist zunehmend anspruchsvoller und kostspieliger geworden um diese Ziele zu erreichen. Ein gegenwärtiger Trend in der Forschung ist daher die Entwicklung von vielseitiger FEE, die ohne großen Aufwand an eine Vielzahl von Detektoren angepasst werden kann, ohne die verlangte Leistungsfähigkeit zu beeinträchtigen.

In dieser Arbeit wird die Entwicklung einer solchen, neuartigen FEE für zwei unterschiedliche Detektorkategorien beschrieben: einerseits abbildende Cherenkov-Zähler und andererseits segmentierte Plastikszintillator-Detektoren. Die ersteren benötigen eine hohe Empfindlich- und Genauigkeit für den Nachweis einzelner Photonen, während die letzteren durch größere und langsamere Signale gekennzeichnet sind.

Das FEE-Designprinzip beruht auf breitbandigen Vorverstärkern und schnellen Diskriminatoren, die zusätzlich Informationen über die Länge des Signals liefern, die sogenannte Time-over-Threshold (ToT). Der Einsatz von Diskriminatoren ermöglicht einen niedrigen Energieverbrauch, geringe Totzeit und selbst-triggernde Fähigkeiten. Alle diese Eigenschaften sind für Anwendungen mit hohen Raten von großer Bedeutung. Die digitalen Ausgabesignale der FEE werden durch ein präzises, auf FPGAs beruhenden TDC-System erfasst. Ausführliche Untersuchungen im Labor konnten die Machbarkeit der vorgeschlagenen ToT-Methode bestätigen. Das komplette Auslesesystem wurde in mehreren Testexperimenten am Mainzer Mikrotron getestet. Dabei wurden sehr hohe Zählraten von mehreren MHz pro Kanal erreicht, sowie eine Zeitauflösung von unter 100 ps nach einer auf ToT-Informationen beruhenden Walk-Korrektur erzielt. Die umfassende Charakterisierung der Analogsignale der Detektoren unter realistischen Bedingungen hat gezeigt, daß ToT-Informationen in bisher nicht genutzter Weise zur Signalbestimmung und Walk-Korrektur zur Verbesserung der Zeitauflösung eingesetzt werden können. Abschließend wurde der Einsatz der entwickelten FEE in sehr schnellen Flugzeitzählern untersucht, sowie ein Ausblick auf zukünftige Trends in der FEE-Entwicklung gegeben.

Contents

Acronyms **iii**

Introduction **vii**

1 Electronics for High Rate Detectors **1**
1.1 Multi-purpose Frontend Electronics 2
1.2 The PANDA barrel DIRC 4
1.3 The Neutron Detector of A1 12
1.4 Trends in Frontend Electronics 18

2 Signal Characterization **23**
2.1 Single photon signals 23
2.1.1 Micro Channel Plate Photomultiplier Tubes 25
2.1.2 Single photon calibration of MCP-PMTs 29
2.1.3 Signal properties of MCP-PMTs 33
2.1.4 Time-walk 36
2.2 Characterization of scintillator signals 39
2.2.1 Laser calibration of the PMT 40
2.2.2 MIP signal properties 41

3 Frontend Electronics Concept **47**
3.1 The TDC Readout Board 3 48
3.1.1 Synchronization studies 51
3.2 Frontend Electronics Design 53
3.2.1 The NINO ASIC chip 54
3.2.2 Discriminator card 56
3.2.3 Preamplifier Add-on card 57
3.3 FEE characterization 58

3.3.1 Preamplifier characterization 59
3.3.2 Discriminator characterization 60

4 Readout Characterization 65
4.1 FEE response to Single Photon Signals 65
4.1.1 General response 66
4.1.2 Timing performance 72
4.2 FEE response to plastic scintillator signals 76
4.2.1 Characterization with cosmic muons 76
4.2.2 Characterization with a radioactive source 79

5 Experiments with Prototypes at MAMI 83
5.1 Beam test with an Imaging Cherenkov Counter 83
5.1.1 The Imaging Counter Prototype 85
5.1.2 General results 87
5.1.3 Imaging capabilities 90
5.1.4 FEE Timing Resolution 94
5.1.5 DIRC Timing Resolution 100
5.2 Beam test with a Scintillator Array 103
5.2.1 The NDet prototype 103
5.2.2 General results 106
5.2.3 Time-over-Threshold response 108
5.2.4 Timing performance 113
5.2.5 Rate Capability 114

6 Future Developments 117
6.1 A Fast Start Counter 117
6.2 FPGA-based FEE 121

7 Conclusion 125

A Signal Characterization 131

B Electronics layouts 137
B.1 TRB3 synchronization 137
B.2 FEE Schematics 138

Acronyms

ADC	Analogue to Digital Converter
ASIC	Application-Specific Integrated Circuit
BESIII	Beijing Spectrometer III
Belle	Belle (French word for beauty) experiment
CERN	Conseil Européen pour la Recherche Nucléaire (European Organization for Nuclear Research)
CTS	Central Trigger System
DAC	Digital to Analogue Converter chip
DAQ	Data Acquisition
DIRC	Detection of Internally Reflected Cherenkov light
EMC	Electromagnetic Calorimeter
FDIRC	Focussing Detection of Internally Reflected Cherenkov light
FAIR	international Facility for Antiproton and Ion Research
FEE	Frontend Electronics
FF	Form Factor
FPGA	Field Programmable Gate Array
GbE	Gigabit Ethernet controller
GEM	Gaseous Electron Multiplier

GPin	General Purpose input
GSI	Helmholtzzentrum für Schwerionenforschung GmbH
LVDS	Low Voltage Differential Signal
MAMI	Mainz Microtron
MAPMT	MultiAnode Photomultiplier Tube
MCP	Microchannel Plate
MCP-PMT	Microchannel Plate Photomultiplier Tube
MIP	Minimum Ionizing Particle
NDet	Neutron Detector
NDF	Neutral Density Filter
NeuLAND	new Large-Area Neutron Detector
NIM	Nuclear Instrumentation Modul-Standard
PANDA	Antiproton Annihilation at Darmstadt
PCB	Printed Circuit Board
PID	Particle Identification
PMT	Photomultiplier Tube
QCD	Quantum Chromo Dynamics
QDC	Charge-to-Digital converter
RICH	Ring-Imaging Cherenkov
SP	Single Photon
SPI	Serial Peripheral Interface
STT	Straw Tube Tracker
TDC	Time to Digital Converter

ToF	Time-of-Flight
TORCH	Time Of internally Reflected Cherenkov light
ToT	Time-over-Threshold
TOP	Time of Propagation
TRB3	TDC Readout Board version 3
TS	Target Spectrometer
TTL	Transistor-Transistor Logic
WLS	Wavelength Shifting Fibre

Introduction

How does the strong interaction confine quarks and gluons into hadrons? This is only one of the open key questions in modern physics. Over the years, increasingly complex experiments have been studying fundamental properties of the Standard Model of particle physics. Missing and elusive particles were discovered; the greatest example is the Higgs boson, which was recently found at CERN (Conseil Européen pour la Recherche Nucléaire) 40 years after its prediction [1, 2]. On the other hand, new puzzles emerged, like the unpredicted XYZ states observed by hadron spectroscopy experiments [3, 4]. The impressive advance of high energy and nuclear physics was made possible by the technological progress in detector instrumentation [5]. Powerful accelerators at various energy and luminosity scales were built to discover new particles, to probe the inner structure of matter or to synthesize heavy nuclei. At the same time, new and sophisticated detection techniques were developed to measure the signatures of rare decays. The complexity and the resolving capability of particle detectors has been constantly increasing. The Frontend Electronics (FEE), which processes the signals of these detectors, has likewise developed in complexity and performance to keep pace.

Nowadays, the frontiers of physics are calling for FEE which can cope with high count rates of several MHz and instrument large amount of channels at lowest possible cost. The solution is frequently based on custom-designed Application-Specific Integrated Circuits (ASICs), with small physical size, low power dissipation, and high radiation tolerance. However, the development of new ASICs has become very demanding in terms of cost and resources. Typically, 2-4 full-time designers need 2-4 years from the concept to the production of an ASIC [6]. This reason favours the development of multi-purpose FEE. High performance ASICs can be adapted to new tasks by using smart strategies in the design of FEE boards.

The FEE proposed in this thesis was originally developed to meet the chal-

lenging requirements of an imaging Cherenkov counter, the Barrel DIRC (Detection of Internally Reflected Cherenkov light) [7] of the PANDA (antiProton ANnihilation at DArmstadt) experiment [8]. The detection of Single Photons (SPs) is of fundamental importance to this detector. It will be equipped with Microchannel Plate Photomultiplier Tubes (MCP-PMTs) providing fast ($\sim$ 2 ns) but small ($<$ 5 mV) signals. High precision timing ($\sigma_{time} < 100$ ps) will be an asset for pattern reconstruction and background suppression. Moreover, the foreseen high luminosity (up to $2 \cdot 10^{32}$ cm^{-2}s^{-1}) sets a minimum requirement for the hit rate of 100 kHz per channel, with a total of about 15000 channels. Last but not the least, the PANDA Data Acquisition (DAQ) scheme imposes the use of triggerless FEE.

The high versatility of this FEE allowed the readout of plastic scintillator arrays. Compared to Cherenkov counters, these detectors are characterized by very different working conditions. Larger and slower signals are produced by the energy loss of charged particles. The highly segmented plastic scintillator array for the future Neutron Detector (NDet) of the A1 Collaboration [9] was chosen as test case. The NDet will be instrumented with MultiAnode Photomultiplier Tubes (MAPMTs), with a total of about 4096 readout channels. The future physics programme imposes high rate requirements (several MHz per channel). Particle Identification (PID) based on deposited energy (dE/dx) to distinguish neutrons and Minimum Ionizing Particles (MIPs) is an additional asset to reduce the considerable background.

The requirements set by general purpose FEE and by the considered detectors, as well as the state-of-the-art are described in Chapter 1. The detailed characterization of the expected input signals is presented in Chapter 2. The results lead to the FEE design in Chapter 3, which is based on a novel application of Time-over-Threshold (ToT). This allowed walk correction of fast MCP-PMT signals and a coarse but quick measurement of the deposited energy in plastic scintillators. Detailed laboratory tests of the full readout are presented in Chapter 4. Finally, the description and the results of prototype test experiments at the Mainz Microtron (MAMI) [10] are shown in Chapter 5. Ongoing and future developments are discussed in Chapter 6.

Chapter 1

Electronics for High Rate Detectors

During the last decades high luminosity experiments achieved important results in the field of nuclear and particle physics. Innovative and outstanding detection technologies were developed to cope with the associated high rates. In particular, the development of fast and precise electronics played a key role in obtaining the necessary high performance. The next generation of accelerators will boost the luminosity and, accordingly, the technological complexity and the cost of R&D programs for FEE will grow at a similar pace. Multi-purpose electronics designs offer a way for matching strong requirements and minimizing the resources. Nevertheless, particular attention must be paid to adapt the same hardware to the input of different detectors. For this reason, a detailed knowledge of the physics program, the experimental conditions and the detector technologies is required.
The FEE proposed in this thesis was originally developed for the read out of an imaging Cherenkov counter, the Barrel DIRC of the PANDA experiment. This is characterized by a SP environment which sets challenging requirements for the FEE.
The flexible design allowed the readout of plastic scintillator arrays too, which are characterized by significantly different working conditions compared to Cherenkov detectors. The NDet of the A1 Collaboration was chosen as test case.
In the next sections the main guidelines of the electronics development are presented, beginning with the concept of multi-purpose FEE itself, through the description as well as the requirements of the Barrel DIRC and the NDet.

1.1 Multi-purpose Frontend Electronics

The FEE is the interface between the sensing elements of particle detectors and the DAQ. It provides the first step of the signal processing (see the diagram in Fig. 1.1).

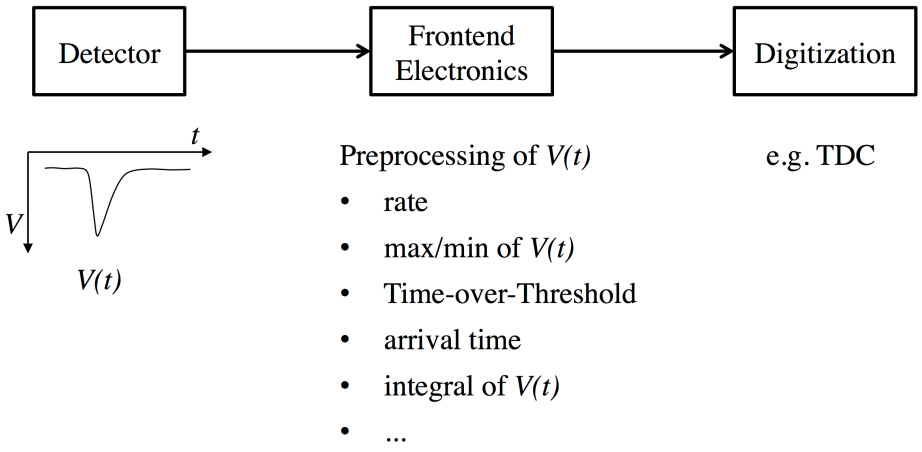

Figure 1.1: Block diagram of frontend signal processing. A detector produces short tension (or current) pulses which are preprocessed by the FEE and then digitized by the readout electronics (e.g. a TDC).

The output of detectors is typically a short current or tension pulse, $V(t)$, whose time response is processed by the FEE. The logic behind the electronics determines the information carried by the output signal. Discriminators, for example, return a rectangular pulse which can be proportional to the width of the input signal, while integrators return a pulse proportional to the integral of $V(t)$, thus to the deposited charge. Many other quantities can be encoded in the response, like event rate, arrival time, minimum/maximum signal, or some combination of these. However the simultaneous optimization of different measurements in the same FEE is usually difficult. As a consequence, some compromises in design cannot be avoided, e.g. a precise integrator has a low timing resolution. This does not represent a disadvantage for single-purpose FEE, because their response is tailored to the specific detector. Vice versa the information encoded by multi-purpose FEE must be carefully chosen; it could fit certain detectors and be inadequate for others. Some FEE designs overcome this limitation by storing the whole pulse

(waveform sampling digitizer), but they have drawbacks like high cost, long readout time and, above all, large amount of information to digitize (more details in Chapter 3). The choice of a proper processing logic is defined by the main detector requirements.

High rate detectors require specific features which do not depends on the FEE processing logic. The desired properties can be summarized as follows:

I. **High count rates**, (on the order of $1 - 10^3$ kHz/channel) to cope with the extremely high interaction rates of new experiments.

II. **Large number of channels**, to limit the rates per channel and to provide the necessary granularity (e.g. in imaging Cherenkov counter).

III. **Robustness** to guarantee a smooth operation for a long period of time. Radiation hardness is also required by several detectors exposed to high particle rates.

IV. **Small amount of data**, to minimize the information which has to be digitized and stored. This reduces computing resources and long dead times for the acquisition.

V. **Low power consumption** to reduce both dissipation and cost.

VI. **Low Cost** per channel is highly desirable and one of the main requirements of multi-purpose FEE.

Most of the requirements are closely connected, for example (IV), (V) and (VI) are a direct consequence of (I) and (II). The physical dimension of the FEE plays also a key role because, very often, the available space inside an experimental apparatus is limited.
The FEE development presented in this thesis had as main target the readout of imaging Cherenkov counters, which are fully described in Section 1.2. In addition, a main asset of the proposed FEE was a high versatility. Plastic scintillator arrays were therefore chosen to test the design under very different working conditions compared to Cherenkov detectors. In this case, the main requirements are described in Section 1.3.

1.2 The PANDA barrel DIRC

The PANDA experiment will be one of the major projects at the international Facility for Antiproton and Ion Research (FAIR) in Darmstadt [11]. FAIR, currently under construction at the Helmholtzzentrum für Schwerionenforschung GmbH (GSI), will provide to several experiment primary proton and ion beams as well as secondary beams of antiprotons and radioactive ions with high energy, quality and unprecedented intensity. The High Energy Storage Ring (HESR) will supply antiproton beams over a broad momentum range from 1.5 to 15 GeV/c, with a momentum resolution of 2×10^{-5} using stochastic and electron cooling. The PANDA detector will measure the collision between the antiproton beam and a fixed target with an average luminosity of 2×10^{32} $cm^{-2}s^{-1}$ (for H_2 target) and an interaction rate of 20 MHz with peaks up to 50 MHz.
The physics program of PANDA addresses several fundamental questions of Quantum Chromo Dynamics (QCD) [8]:

- Hadron spectroscopy up to the region of charm quarks. Here the search for exotic states like glueballs, hybrids and multi-quark states in the light quark domain and in the hidden and open charm region is the focus of interest. The recently found XYZ states will be further explored.

- Study of properties of hadrons inside nuclear matter. Mass and width modifications have been reported and will be investigated also in the charm region. PANDA will also study double Λ hypernuclei, which are of great importance for nuclear structure studies and for a deeper understanding of the $\Lambda\Lambda$ interaction. In particular, these investigations will require the use of a solid target.

- Hard exclusive antiproton-proton reactions can be used to study the structure of nucleons (time-like form factors). Interesting aspects of Transverse Parton Distributions will be studied in Drell-Yan production.

- Direct CP violation in hyperon decays and CP violation and mixing in the charm sector.

Of these different topics, hadron spectroscopy represents the most important field of investigation which PANDA will cover. In particular, the study of charmonium-like states XYZ will play a major role. In the last years, several

unpredicted states like the X(3872), the Y(4260) or the $Z_c(3900)$ were discovered using the e^+e^- colliders [3]. Their nature is still uncertain and points to non-conventional $c\bar{c}$ states like mesonic molecules, hybrids or tetraquarks. In order to study these states, PANDA will use both formation $p + \bar{p} \rightarrow X_{c\bar{c}}$ and production $p + \bar{p} \rightarrow X_{c\bar{c}} + M$ processes with one or more mesons M [12]. The $p\bar{p}$ collisions have the advantage that any quantum number can be formed, while in e^+e^- collisions only formation of $J^{PC} = 1^{--}$ is possible. Higher cross sections are therefore expected and this will considerably reduces the time necessary for collecting large data samples. For example, the Y(4260) will be produced with cross section approximately 30 times higher than at the BESIII (Beijing Spectrometer III) experiment. The high statistics for the Y(4260) (approximately 16,400 expected events per day) will enable the search for rare decays with unique precision [12].
This ambitious program requires an excellent detector, where particle identification (PID) assumes a central role. The PID is particularly important for final states containing several kaons and pions.

The design of the PANDA detector, reported in Fig. 1.2, has to achieve 4π acceptance, high resolution for tracking, PID and calorimetry, high rate capabilities, a versatile readout and event selection. To obtain a good momentum resolution the detector is composed of a Target Spectrometer (TS) and a Forward Spectrometer (FS). The former comprises a superconducting solenoid magnet surrounding the interaction point and it measures at large angles. The latter is composed by a dipole magnet for the reconstruction of small angle tracks. In both spectrometers tracking, charged particle identification, electromagnetic calorimetry and muon identification are available to allow the detection of the complete spectrum of final states relevant for the physics program. A detailed description of the detector elements can be found in [8].

As previously mentioned, PID over a large range of angles and momenta is an essential requirement for meeting the physics objectives of PANDA. The Electromagnetic Calorimeter (EMC) will perform energy measurements and PID especially for neutral particles. Several dedicated systems, complementary to the other detectors, will provide information to identify charged hadrons and leptons. For momenta below 1 GeV/c the tracking detectors will be used to measure the energy loss (dE/dx) [13, 14]. Here in particular the Straw Tube Tracker (STT) and the Gaseous Electron Multiplier (GEM) tracking detector will supply the PID information. Moreover a Time-of-Flight (ToF) barrel detector will identify slow particles. The main part of the momentum spectrum

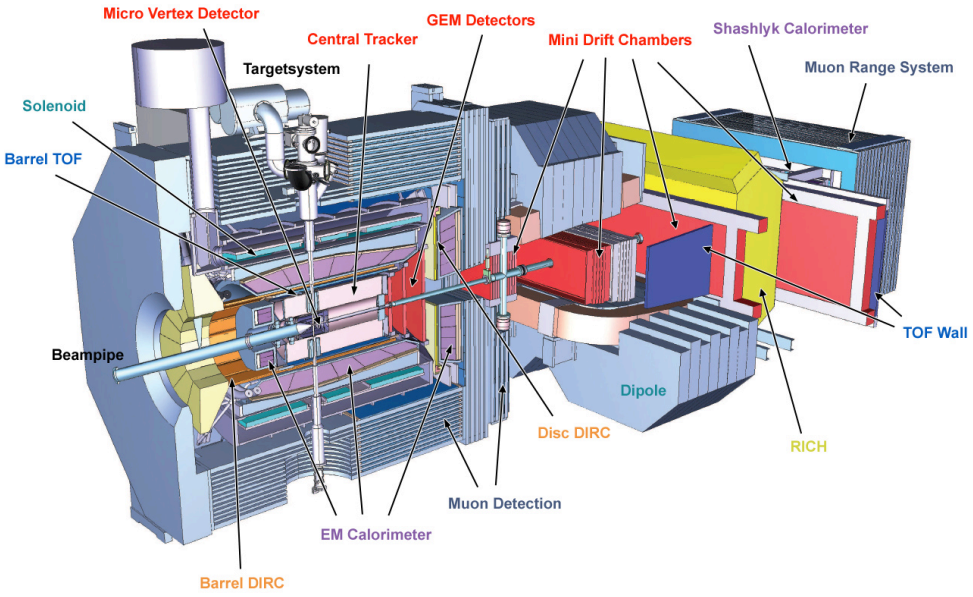

Figure 1.2: Layout of the PANDA detector consisting of a target spectrometer, surrounding the interaction region, and a forward spectrometer to detect particles emitted in the forward region. The antiproton beam enters the apparatus from the left side [8].

above 1 GeV/c will rely on two Cherenkov detectors, the Barrel DIRC and the Endcap DIRC, providing PID in the central ($22° < \theta < 140°$) and forward ($5° < \theta < 22°$) region respectively (see Fig. 1.3). The particular geometry of the Endcap DIRC requires a dedicated optimization of the FEE dimensions which was not performed in the presented case. A detailed description of this detector can be found in [15]. Before describing the details of the Barrel DIRC design and the requirements for the associated readout, the working principle of this detector will be briefly explained, to better clarify the motivation behind the need of high performance on SP detection.
As it is well known, charged particles traversing a medium with refractive index $n\,(\lambda)$ at a speed $\beta > 1/n(\lambda)$ emit Cherenkov radiation at a characteristic angle θ_c,

$$\cos\theta_c = \frac{1}{\beta n(\lambda)} \tag{1.1}$$

uniformly in azimuthal angle ϕ_c with respect to the particle path as shown in Fig. 1.4 (a). The emission spectrum, given by the Frank-Tamm equa-

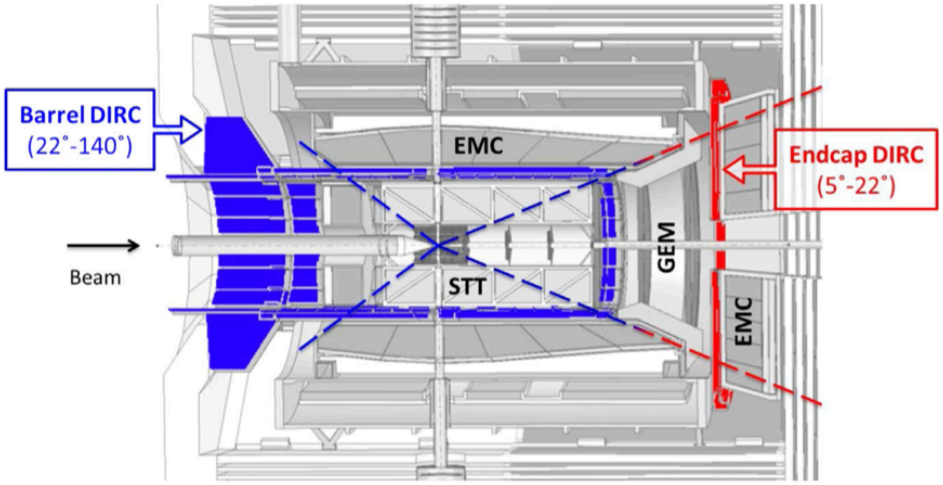

Figure 1.3: Schematic cross section of the PANDA TS. Both, the Barrel DIRC and the Endcap DIRC are highlighted (in blue and red, respectively) and their polar acceptance is indicated by the dashed lines. The STT adjoins the Barrel DIRC on the inside and the EMC on the outside. In the forward direction the GEM tracking detector and the Endcap EMC surround the Endcap DIRC [7].

tion [16] is continuous, mainly concentrated in the visible and UV region. Ring-Imaging Cherenkov (RICH) detectors use a thin layer of a suitable material (e.g. aerogel) as radiator for particle passing through it [17]. The light cone produced expands through a stand-off volume filled with a non-radiative material (with $n(\lambda) \approx 1$) and gets collected onto a photodetector plane.
The knowledge of the particle trajectory and the light pattern allows the reconstruction of the angle θ_c, and consequently the measurement of the particle speed, as suggested by Eq. 1.1. Thus, the mass of a particle can be determined by combining its speed with the momentum information given by tracking detectors.
The PID capability of a RICH can be expressed by considering the difference of the quantity $\sin^2\theta_c$ (derived from Eq. 1.1) for two particles with mass m_1 and m_2 at momentum p [18]:

$$\Delta \sin^2\theta_c = \frac{m_2^2 - m_1^2}{n(\lambda)^2 p^2} = \frac{\Delta m^2}{n(\lambda)^2 p^2}. \tag{1.2}$$

The number of standard deviations n_σ to describe the quality of the separation between m_1 and m_2 can be obtained from the previous equation:

$$n_\sigma = \frac{\beta^2 \Delta m^2}{2p^2 \tan\theta_c \sigma_{\theta_c}} \tag{1.3}$$

where σ_{θ_c} is the error on the reconstructed Cherenkov angle.

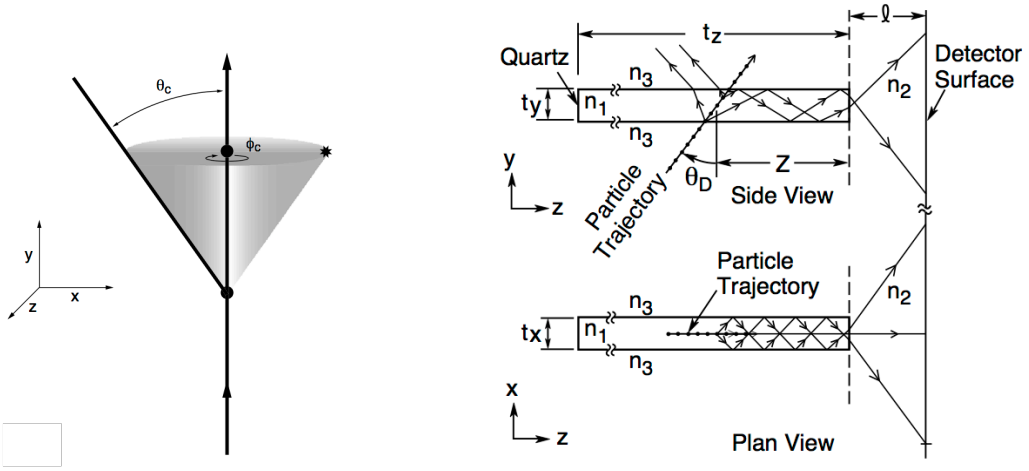

(a) (b)

Figure 1.4: (a) Schematic of typical Cherenkov reference frames with respect to the particle path. (b) Schematic of a radiator bar illustrating the DIRC reference frame. The particle trajectory is shown as a line connected by dots; representative trajectories of Cherenkov photons are shown by lines with arrows [19].

DIRC counters are a particular class of RICH detectors, and they were first developed for the BaBar experiment [20]. While RICHs usually require a considerable amount of space, DIRC detectors were specifically conceived to minimize the material budget, and to fit the compact design of detectors like BaBar. The principle, illustrated in Fig. 1.4 (b), exploits a fused silica bar which serves as radiator and light guide. Indeed, due to total internal reflection part of the Cherenkov light propagates inside in the radiator bar.The absolute value of θ_c is conserved because of the excellent surface polish of the radiator bar. The light exits at one of the two ends of the bar, which is coupled to a stand-off volume. At a distance l, a plane of photodetectors collects the incoming Cherenkov photons whose pattern is then used for the

reconstruction of θ_c. The DIRC of BaBar used the so called "pinhole" focusing scheme, where the path of the photon down the bar is ignored. The angular resolution is independent of the precise track location in the bar and can be expressed as follows:

$$\sigma_\alpha \approx \sqrt{\frac{t_x^2/12 + \sigma_x^2(detector)}{L^2}}, \tag{1.4}$$

where t_x is the size of the bar and $\sigma_x(detector)$ the spatial resolution of the photodetectors (approximately the pixel size) and $L = Z + l$ the distance from the track to the focal plane (see Fig. 1.4 (b)). Designs with a focussing scheme before the stand-off volume do not depend on t_x and allow higher resolutions:

$$\sigma_\alpha \approx \sqrt{\frac{\sigma_x^2(detector)}{L^2}}. \tag{1.5}$$

Both equations clearly highlight the importance of high granularity photodetectors, and show that for a fixed area, the larger the number of pixels, the higher the achievable resolution. However, a high granularity usually implies a large number of readout channels. This requires high channel density and low power FEE.

While a large L helps increasing the resolution as intuitively explained by Eq. 1.4 and 1.5, it also introduces a number of ambiguities due to the bounces inside the bar. This can be disentangled with an excellent timing resolution. Another drawback of a large L is the loss of photons, which affects the performance. Indeed, the total error on the Cherenkov polar angle scales as:

$$\sigma_{\theta_c} = \frac{\langle \sigma[\theta_i] \rangle}{\sqrt{N_\gamma}} \oplus c, \tag{1.6}$$

where $\langle \sigma[\theta_i] \rangle$ is the error on each individual photon, N_γ is the number of detected photons per track, and c is a correlated component combining contributions from several sources including tracking, alignment errors and multiple scattering. In general, N_γ strongly depends on the detector design, in particular on the material used for the stand-off volume as well as its dimension (the larger the volume, the higher the background). Several strategies can be adopted to improve the light yield, like providing the other end of the bar with a mirror, to recover the light in the backward direction. However, a large amount of channels together with the low photon statistics typical of these detectors ($\sim 20 - 30$ detected photons/track), implies the use of

photodetectors sensitive to SP signals. Therefore, the FEE has to read out small input signals (few mV).
The arrival time of Cherenkov photons can be used to improve the resolution of DIRC detectors, which are intrinsically 3-D devices (x-y position and time). For example the patterns are affected by a smearing caused by the chromatic dispersion. Indeed, photons produced at different λ propagate in the bar with slightly different angles as indicated by Eq. 1.1. The FDIRC (Focussing Detection of Internally Reflected Cherenkov light) prototype demonstrated that a timing resolution on SP of the order of 100-200 ps helps to substantially reduce the chromatic component in $\langle\sigma[\theta_i]\rangle$ [21]. To achieve that, the intrinsic resolution of the FEE needs to be well below 100 ps. An excellent timing can be also used for both background reduction and event reconstruction with a time-based likelihood approach. In particular, the latter is used by a new class of DIRC counters, like the Time of Propagation (TOP) counter of Belle II [22] and the proposed Time Of internally Reflected Cherenkov light (TORCH) of LHCb [23]. A detailed description of all the properties of DIRC detectors can be found in [19].

The PANDA barrel DIRC adopts a focussing design similar to the FDIRC. The detector has to fit within the TS magnet return yoke. Therefore, a small stand-off volume has to be used. In the current baseline design, shown in Fig. 1.5, 80 narrow radiator bars, with a thickness of 17 mm, a width of 32 mm, and a length of 2400 mm, made of synthetic fused silica will be grouped into 16 bar boxes, with a barrel inner radius of 48 cm, and coupled to a stand-off volume with a depth of 30 cm. Two options are still under investigation: a common oil-filled expansion volume or, as alternative, a segmented stand-off volume with one fused silica prism per bar box. Focussing optics, used to reach the desired PID performance, are composed of lenses with a high-refractive index material, e.g. N-Lak 33 [24], which avoids air-gaps thus minimising photon losses at the interfaces (see Fig. 1.5). The image plane will be instrumented with MCP-PMTs, since the photon detectors have to operate in the strong magnetic field ($\sim$1 T) of the TS and they have to provide sufficient gain to detect single photons. The large detection area of MCP-PMTs and their radiation hardness are highly advantageous. Moreover, they are designed to achieve high timing resolution ($<$ 100 ps). The PHOTONIS Planacon MCP-PMT is an excellent photon detector candidate for the Barrel DIRC. It provides 64 channels in a 8×8 matrix with pixel dimensions of 6×6 mm^2. Recent improvements in its lifetime, with up to 6 C/cm^2 integrated

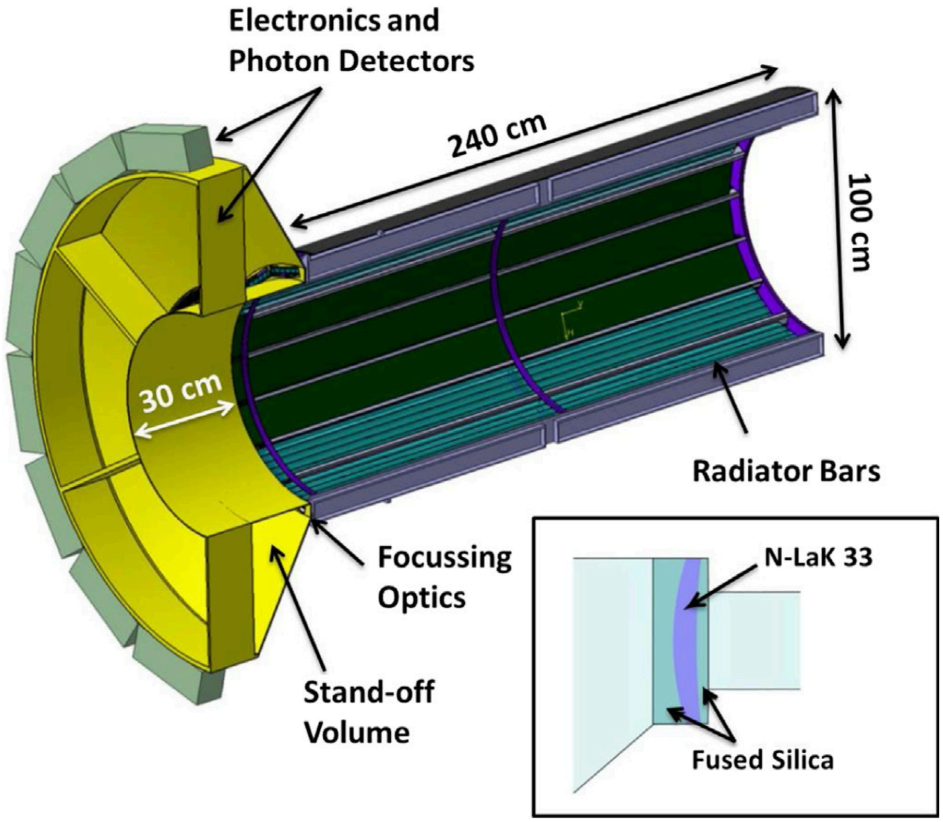

Figure 1.5: Schematic drawing of the Barrel DIRC baseline design. The focussing optics using high-refractive index material is shown in the inset. [7]

anode charge without deterioration [25], fulfil the Barrel DIRC requirements. Its fast timing response, with a single photoelectron resolution $\sigma_{SP} < 50$ ps, aids in pattern recognition as well as in chromatic dispersion correction. The detailed description and characterization of MCP-PMT signals is addressed in Chapter 2 (Section 2.1). The anticipated timing resolution of the full readout chain is required to be $\sigma_t < 100$ ps. This calls for high precision FEE. In total, the Barrel DIRC will have approximately 15,000 readout channels. As a consequence, the FEE must be compact with low power consumption and high channel density in order to fit the limited available space. Taking into account the interaction rate of PANDA, the final rate per channel will be on the order of 50-100 kHz. The number of channels to equip and the high rates

will also require a minimization of the amount of transmitted data per event. Last but not the least, the PANDA DAQ scheme imposes the use of trigger-less FEE. Table 1.1 summarizes the main requirements that the FEE has to meet.

Table 1.1: Summary of the Barrel DIRC and the corresponding FEE requirements.

Requirements	FEE requirements
SP signal detection	∼2 mV peak, 2 ns width input pulses
15,000 channels	compact, low power, high channel density
Excellent timing resolution	$\sigma_t < 100$ ps for the full readout
High rate per channel	50-100 KHz/channel

1.3 The Neutron Detector of A1

The 3-spectrometer-facility of the A1 Collaboration [26] is one of the main experimental setup at MAMI. MAMI is a continuous wave electron accelerator [10]. A cascade series of three Race Track Microtrons (RTMs) and a Harmonic Double Sided Microtron (HDSM) accelerate electrons from 180 MeV/c up to 1.6 GeV/c [27, 28]. Polarized electron beams (polarization degree typically 80%) of more than 20 μA beam current and unpolarized electron beams of up to 100 μA can be achieved. The accelerator provides a well-defined beam with a diameter of a few 0.1 mm and an energy uncertainty of less than 13 keV.

The detector setup of the A1 Collaboration is composed of three high resolution magnetic spectrometers, labeled A, B and C, which can be operated in single, double or triple coincidence mode. A photograph of the experimental hall with the spectrometers is shown in Fig. 1.6. Each spectrometer can be rotated around a central pivot to measure at different scattering angles. The magnetic system of spectrometer A and C includes a quadrupole, a sextupole, and two dipoles. It enables high resolution measurements of particle momentum and angle within a relatively large acceptance (up to 28 msr). A single dipole in a clamshell configuration is used for spectrometer B, providing a slim design with higher spatial resolution but smaller acceptance (5.6

msr). In addition, spectrometer B can be tilted for out-of-plane measurements. The spectrometers can achieve a momentum resolution of 10^{-4}, with a position resolution of 3-5 mm, 1 mm and 3-5 mm respectively.

Each spectrometer is equipped at the focal plane with similar detector sys-

Figure 1.6: The A1 hall. The three big spectrometers A (red), B (blue), C (green) are visible. The thin upstream beam pipe comes in from the right [29].

tems: two scintillator planes, two packets of two vertical drift chamber layers (VDC) and a threshold Cherenkov detector. The scintillator arrays provide

trigger information, a time reference and particle identification through ToF and energy loss (dE). The timing information can be used for the coincidence logic between the spectrometers. The drift chambers measure the particle trajectory inside the spectrometers with high precision ($\sim$200 μm FWHM) and together with the magnetic field they give information about the particle momentum. The Cherenkov detectors are filled with gas (decafluorobutane R3-1-10) as radiator material, and use a system of mirrors and Photomultiplier Tubes (PMTs) to collect the Cherenkov light. Electrons and positrons with energies higher than 10 MeV emit Cherenkov radiation, while pions with energies lower than 2.7 GeV do not: the detector provides therefore a discrimination between light leptons and heavier particles. Moreover, other equipment can be used for different experiments, e.g. a Møller polarimeter for spin-dependent cross section measurements in elastic scattering.
The target system is enclosed in a vacuum scattering chamber located on the rotation axis of the spectrometers. A cryogenic target system allows the use of liquified hydrogen, helium, and deuterium. Solid targets can be used as well. A detailed description of the experimental setup can be found in [26].

The A1 physics program is focussed on the study of hadron physics. Nowadays, one of the open questions is, among others, the complete characterization of the nucleon structure. The determination of nucleon Form Factors (FFs) is a key ingredient of this study. In particular, the measurements of electromagnetic (e.m.) FFs in elastic and inelastic scattering, as well as the structure functions in deep inelastic scattering of leptons, have been a precious source of information since the 1960s. In recent years, the achievable precision of experiments improved significantly showing shortcomings in the consistency and interpretation of the data [30].
The proton FFs have been investigated with high precision using several electron accelerators which combine high-current with high-polarized electron beams: e.g. MIT-Bates [31], ELSA [32], and the Continuous Electron Beam Accelerator Facility (CEBAF) of the Jefferson Laboratory (JLab) [33]. In this framework, the A1 Collaboration has reached the best precision so far [34]. While high-quality data are available for the proton, the experimental status of the neutron is still dominated by large uncertainties. This is clearly visible in Fig. 1.7, where the present data of electric, G_E^n (a), and magnetic, G_M^n (b), neutron FF over the whole four-momentum transfer range are shown. In the Sachs parametrization [35] G_E^n and G_M^n are interpreted as the Fourier transforms of the spatial charge and the current distributions in the nucleon.

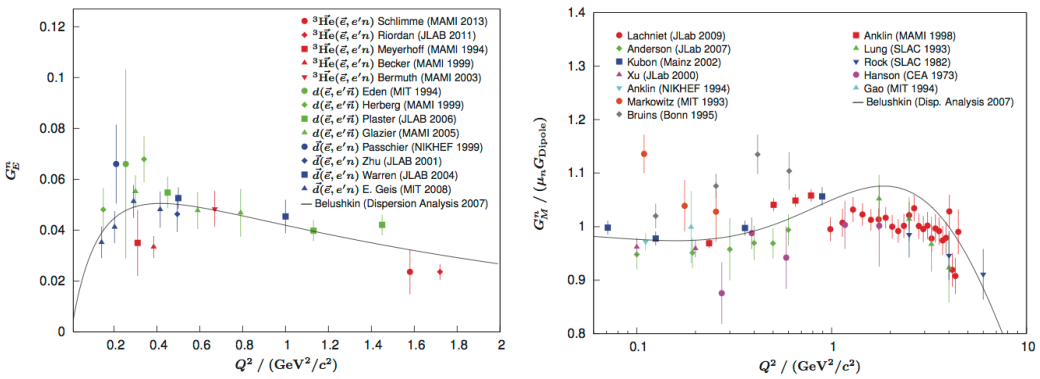

(a) (b)

Figure 1.7: Existing data on neutron FFs, G_E^n (a) and G_M^n (b) [30].

The absence of a free neutron target makes the experimental determination of the neutron FFs challenging. Nevertheless, electron scattering on light nuclei like ^{2}H and ^{3}He have been employed to extract information about the neutron FF. Experiments use both, elastic scattering on the nucleus and quasi-elastic scattering on the bound nucleons. Intuitively, the presence of protons constitutes a strong source of background, thus calling for methods to disentangle the contributions of the two nucleons. Different experimental techniques have been developed (see [30] for a detailed review on the subject). For example, quasi-elastic e^--d and elastic e^--p cross sections were compared to determine G_M^n. Other methods made use of polarized ^{3}He targets [36]. Concerning G_E^n, several measurements with polarized electron beams were performed at MAMI starting in the early 1990s. The latest result at a momentum transfer $Q^2 = 1.58$ GeV$^2/c^2$ has proven the feasibility of such a measurement in this Q^2 regime at MAMI [37]. Nevertheless, the existing data on the neutron FFs have several serious restrictions:

- G_M^n is relatively accessible because the experimental methods do not suffer from low count rates. However, the systematic errors dominate the measurements, as the discrepancies between the existing data reveal, especially for low momentum transfers (see Fig. 1.7 (b)). The systematic errors of nearly all existing experiments are dominated by the uncertainty of the neutron detection efficiency.

- G_E^n is much smaller than G_M^n in the Q^2 range explored up to now. The strong magnetic contribution to the cross section limits the available statistics and it is source of a large background (depending on the momentum transfer range). For this reason, alternative techniques using polarization degrees of freedom have been developed. In particular the measurement of the FF ratio G_E^n/G_M^n has been employed to gain information using G_M^n from other experiments or parametrizations. In this case, the polarization of the scattered neutrons has to be determined [38, 39].

A considerable improvement in the neutron detection is of crucial importance. In particular high rate capability assumes a central role because of the small G_E^n cross section and the large background. At the same time a detection efficiency of 80% is required. A high versatility to provide neutron polarimetry and to cover a large Q^2 range is an asset. In the coming years, one of the main physics goals of the A1 Collaboration is an improvement by a factor of two in systematic and statistical errors of the neutron FFs determination.

For this purpose, the experimental setup will be upgraded with a new Neutron Detector (NDet). A highly segmented design based on plastic scintillators has been proposed to cope with the high rates necessary for the G_E^n measurement. The NDet will have a volume of approximately one cubic meter. The system consists of scintillator bars[1] (960 mm length, 15 mm height, 30 mm width, decay time approximately 2.4 ns) to achieve a high granularity. The spatial resolution will be increased by arranging the bars in consecutive layers, alternating between vertical and horizontal orientation. The NDet design comprises 32 layers with 64 bars/layer and allows a configuration geometry with two units (16 layers each) placed side by side for measurements of the neutron polarization. For example, Fig. 1.8 (a) shows a GEANT4 simulation [40] of a cubic design hit by a proton. The design will also allow a relocation of the NDet inside the experimental hall, depending on the chosen kinematic, e.g. Fig. 1.8 (b) shows a possible position for coincidence measurements with Spectrometer B. Each scintillator bar is composed by two sections glued together and read out by three Wavelength Shifting Fibres (WLSs)[2] (decay time approximately 12 ns) placed in between

[1] BC-400, Saint-Gobain Ceramics & Plastics
[2] Y10, Kuraray

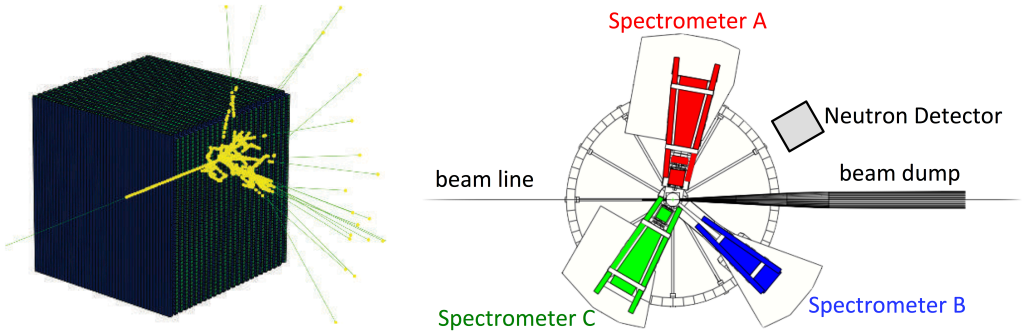

(a) (b)

Figure 1.8: (a) GEANT4 simulation of the neutron detector hit by a proton [40]. (b) schematic of the A1 spectrometer arrangement. The grey square shows a possible position of the A1 NDet (not drawn to scale).

(see Fig. 1.9). The WLSs are connected via commercial optical connectors to three clear fibres (on both sides). The clear fibres are then connected to one pixel of a MAPMT[3] (64 ch, 2×2 mm^2 pixel size). Depending on the configuration, the NDet will be instrumented with up to 4096 channels. A spatial resolution of less than 1.5 cm (FWHM) and a timing resolution (left-right differences) of less than 0.5 ns is achievable in this geometry. The released energy per bar will be used to disentangle neutrons from MIPs, together with tracking information in the NDet and spectrometer data. The characterization of the expected input signals will be presented in Chapter 2. More details about the NDet can be found in [40].
The NDet requires a FEE design which can deal with several MHz per channel, performing accurate timing measurement ($<<$ 0.5 ns) and providing charge information as well. Compared to the Cherenkov detectors, described in the previous section, the typical signal of scintillators is much larger (several tens of mV) and slower ($>>$ 10 ns compared to $\sim$ 2 ns). For this reason, a high dynamic range of the FEE is required. The considerable number of channels and the high rate need a reduction of the amount of transmitted data per event, like in the case of the Barrel DIRC. Moreover, the experimental conditions of A1 require robust FEE, which needs to be operated close to the beam dump (see Fig. 1.8 (b)), under high radiation conditions. The main FEE requirements are summarized in Table 1.2.

[3]H7546, Hamamatsu

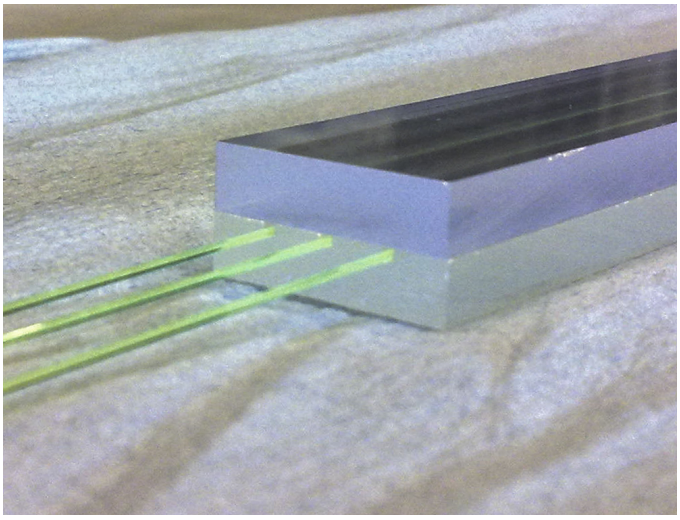

Figure 1.9: Picture of one bar end with three WLSs.

Table 1.2: Summary of the NDet and corresponding FEE requirements.

Requirements	FEE requirements
Readout scintillator signals	>>10 mV peak, >> 10 ns width input pulses
4096 channels	compact, low power, high channel density
High rate per channel	several MHz/channel
PID information	input charge measurement
Possible high radiation	robustness

1.4 Trends in Frontend Electronics

Single-use or multi-purpose approaches have been adopted for the readout of detectors similar to the cases presented in the previous sections. Two relevant FEE designs are reported below.
In the field of Cherenkov counters, a significative example is the TOP of Belle II [22]. As previously mentioned, this detector, based on the DIRC principle, will perform PID using the time of propagation of Cherenkov photons as main observable. The goal is to achieve a timing resolution on the order of $\sigma_t < 50$ ps for the full readout. The chosen MCP-PMTs[4] will contribute with 40 ps transit-time spread. To meet the desired timing resolution, the intrinsic contribution of the electronics must be less than 30 ps. The FEE

[4]R10754-07-M16(N), developed by Belle II and Hamamatsu

will be realized with the IRSX ASIC [41], whose main characteristics are:

– eight channels of switched-capacitor array memory, allowing the capture and storage of time-sampled analogue waveforms;

– an analog storage of 32,768 samples for each channel;

– a nominal sampling rate of 2.7 GSample/s, corresponding to 12 μs of waveform in a circular buffer;

– on-die comparators to digitize only hit channels.

In addition, a preamplifier[5] is used to cope with the small SP signals. To deal with the expected data rate, a recent generation of Field Programmable Gate Array (FPGA)[6] will be used to control and digitize the ASIC output. The FPGA will also extend the usability of the FEE with future firmware upgrades. The last published results of the TOP group report a timing resolution for the full readout below 65 ps [41].
Such waveform-sampling FEE is by definition versatile and it fits multiple applications (see [42] for examples). Indeed, the possibility of storing the entire waveform is the greatest advantage of this design. All the characteristics of the signal can be extracted offline (arrival time, charge, amplitude and pedestal, among others). On the other hand, the large amount of data together with the 8000 channels of the TOP demand a minimization of the digitized information. In particular, only the charge and the time (extracted by the FPGAs) will be delivered to the DAQ of Belle II.
A major drawback of this electronics is the requirement of a trigger and the dead time for the readout depending on the signal processing. While the 30 kHz trigger of Belle II and the beam dead time allow the use of waveform-sampling, triggerless schemes and CW beams like in case of PANDA, exclude it. Moreover, the cost of waveform-sampling chips is higher compared to "standard" electronics like discriminators.

The FEE developed for the new Large-Area Neutron Detector (NeuLAND) detector is an important example for the readout of plastic scintillator arrays [43]. NeuLAND is designed for studies of Reactions with Relativistic Radioactive Beams (R^3B) at FAIR. It features high detection efficiency, high

[5]LMH6629, Texas Instruments
[6]Xilinx Zynq

resolution, and large multi-neutron-hit resolving power. This is achieved by a highly granular design of plastic scintillators, avoiding insensitive converter material. The detector consists of 3000 individual submodules with a size of $5 \times 5 \times 250$ cm^3, arranged in 30 double planes providing an active area of 250×250 cm^2 and a total depth of 3 m. The spatial resolutions is $\sigma_{x,y,z} \approx 1.5$ cm, corresponding to a time resolution $\sigma_t \approx 150$ ps. The main design goal includes also a detection efficiency above 95% for single neutrons. The design and the performance of NeuLAND are thus very similar to the A1 NDet (apart from the use of light-guides instead of WLSs).
The detector is readout by the TacQuila electronics [44]. TacQuila was developed at GSI specifically for time measurements of ToF detectors with several thousand channels. The electronics feature:

– 16 channels/board, with a high resolution Time-to-Amplitude Converter ASIC (TAC) stage and a 12 bit Analogue to Digital Converter (ADC) for each channel;

– a piggy-back board with a Charge-to-Digital converter (QDC) to measure the charge simultaneously to the time;

– an external trigger input for the readout.

TacQuila can achieve a timing precision of about 20 ps RMS (between two channels in the same board). A frontend control and trigger card, named TRIPLEX, enables the communication, monitoring and control of each individual channel and delivers the output necessary for NeuLAND [45]. The electronics was tested up to 300 kHz/channel event rate, even though the expected rates are much lower. The FEE of NeuLAND cannot sustain rates of several MHz per channel. Therefore, it cannot be used for the readout of the A1 NDet.

Both the IRSX ASIC and TacQuila are high performance electronics. While the former is multi-purpose, the latter is a classic single-purpose electronics. These FEE do not meet some requirements of the detectors which have been described in Section 1.2 and 1.3.
Discriminators are a valid option for the FEE design. Their fast processing logic can provide high timing resolution with self-triggering capability. Their low power consumption and low cost are other important advantages. A clever FEE architecture can provide high flexibility to discriminator chips

and it can improve their original features.
The charge measurement in discriminator can be implemented encoding the ToT of the original pulse in the output signal. The ToT can be then used to correct the time-walk of MCP-PMTs and to determine the dE of particles in plastic scintillators.
The signal characterization which guided the development, the design and the proof of concept are described in the next chapters.

Chapter 2

Signal Characterization

The first step for the electronics design is the detailed study of the expected input signals. The main target of the FEE development was originally the readout of Imaging Cherenkov counters. The challenging requirements of this type of detectors include high performance on the detection of SP signals (see Section 1.2). These are usually small and fast voltage pulses which demand a careful characterization. Particular attention must be payed on the timing performance.
A high versatility of the FEE was an asset for different applications. Plastic scintillators were chosen as test case for their larger and slower signals compared to Cherenkov detectors (see Section 1.3). For this reason, the signal shape is different and it calls for dedicated studies.
The typical input signals of both cases were studied with dedicated setups in laboratory. The detailed characterization, which served as input for the FEE R&D, is presented in this chapter.

2.1 Single photon signals

The SP detection capability is of fundamental importance for a large number of particle detectors (e.g. Cherenkov PID detectors and fast time-of-flight detectors, among others). In general, the use of standard PMTs precludes the achievement of high precision timing for SP events. To accomplish such a task, characteristics like transit time spread and rise time of the PMTs need to be as small as possible (< 100 ps). High gain ($\sim 10^5$ to 10^6) and high signal-to-noise ratio are of crucial importance as well. Among the currently available

photon detectors, MCP-PMTs offer the best timing response characteristics and magnetic field resistance (more details in Section 2.1.1). As mentioned in Section 1.2, they were chosen for the readout of the Barrel DIRC.

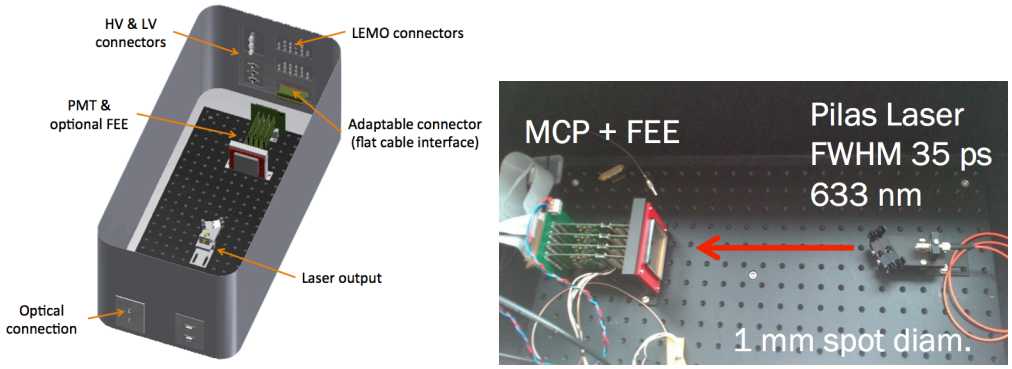

(a) (b)

Figure 2.1: (a) 3D CAD-Model of the light-tight box. (b) photo of the box interior with laser collimator and MCP-PMT (plus optional electronics) fixed on the optical breadboard.

Rigorous studies for testing the MCP-PMT response to SP required the use of a dedicated setup. A metal light-tight box, see Fig. 2.1 (a), is used to shield the photodetector from ambient light and to reduce possible electrical noise. The interior is furnished with an optical breadboard which is used to place sensors, electronics and laser head for systematic studies. The opening top panel allows operation inside the box. The closing mechanism relies on latches and the sealing is enhanced by a rubber band applied on the edge. Adhesive black felt is applied to the inner surface in order to improve light absorption and reduce internal reflections. A configurable interface panel is placed in one side of the box and equipped with various cable connectors for data taking and two power supply masks (for high and low voltage). The opposite side of the box is provided with additional connectors for optical fibres. Each mask is isolated with black silicone for light shielding. Sufficient light-tightness for precision measurements with SP was proved using standard PMTs and a flashlight.
A picosecond pulsed laser[1] was used for the MCP-PMT characterization [46].

[1]EIG1000D, Advanced Laser Diode Systems GmbH

The system consists of a control unit and an optical head with an electrical driver and a laser diode. Trigger input and output are available as Transistor-Transistor Logic (TTL) signals. The chosen optical head produces short laser pulses with a full width half maximum (FWHM) of 35 ps and a wavelength of 633 nm. The repetition rate can be varied up to 1 MHz. The laser light is guided into the box via optical fibres. A collimator, fixed on an adjustable support, focuses the laser light on the MCP-PMT, which is placed at a distance of approx. 20 cm and held by a dedicated frame (see Fig. 2.1 (b)). The initial intensity of the laser I_0 can be attenuated by using Neutral Density Filters (NDFs) with an optical density d:

$$I/I_0 = 10^{-d}, \tag{2.1}$$

where I is the output intensity. The NDF holder can accommodate up to four filters, with a 60° angle compared to the beam axis in order to prevent back reflections into the laser collimator. The illuminated area on the MCP-PMT can be adjusted between one and several mm spot diameter.

2.1.1 Micro Channel Plate Photomultiplier Tubes

Microchannel Plates (MCPs) are planar electron multipliers used for charged particle detection. Fig. 2.2 (a) shows the schematic structure of a MCP [47]. A slab made from highly resistive material (e.g glass) of typically 2 mm thickness, contains a large number of capillaries (channels) bundled in parallel and equally distributed. The internal diameter of the channels ranges from 6 to 20 μm and it is realized through chemical etching. The inner wall has a suitable electrical resistance and secondary emissive properties. Each channel acts as an independent electron multiplier. Fig 2.2 (b) shows the cross section of a channel and its principle of multiplication. An electron impinging on the inner wall of a channel produces secondary electrons. The voltage V_D applied across both ends of the MCP accelerates the secondary electrons which collide with the wall again and, in turn, produce additional secondary electrons. The process is repeated many times along the channel and, as a result, an electron avalanche reaches the output end. MCP-PMTs are realized by incorporating two MCP layers to increase the gain between a photocathode and a multi-anode matrix, as shown in Fig. 2.3. The photoelectrons emitted from the photocathode generate electron avalanches through the MCPs which are collected by the anode. The typical distance between

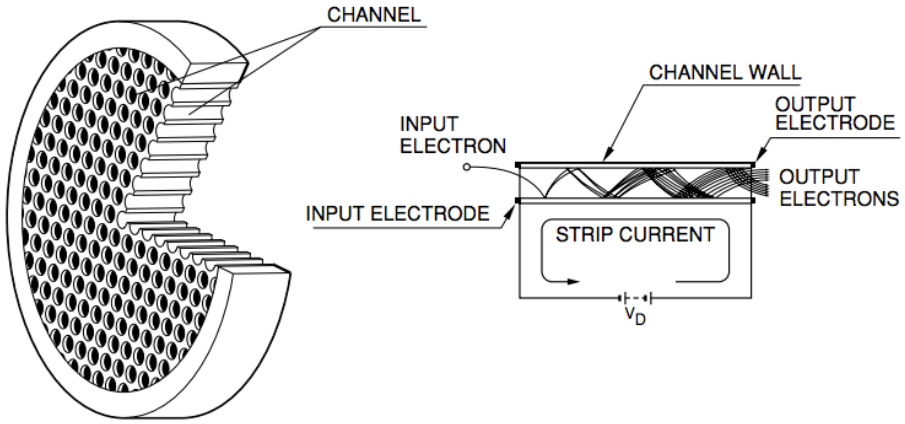

(a) (b)

Figure 2.2: (a) schematic structure of an MCP. (b) multiplication process along an MCP channel; an electron hits the channel wall and produces a cascade proportional to the voltage V_D up the output electrode [47].

photocathode and MCP is 2 mm. The input side can be covered by a thin film called "ion barrier", in order to prevent ions generated inside the MCP from bombarding the photocathode. The production mechanism of the avalanche with respect to conventional discrete dynodes provides outstanding features like [47]:

I. high gain ($\sim 10^6$) in a compact package;

II. fast timing response (< 100 ps);

III. capability of 2D detection with good spatial resolution (few $\sim$mm);

IV. high magnetic fields resistance (up to several T);

V. low power consumption.

No other photodetectors can currently provide these characteristics together with a long lifetime.
The MCP-PMT considered for the PANDA Barrel DIRC is the Planacon XP85012[2]. The XP85012 features a bialkali photocathode and 64 square pixels, arranged

[2]PHOTONIS USA Pennsylvania, Inc.

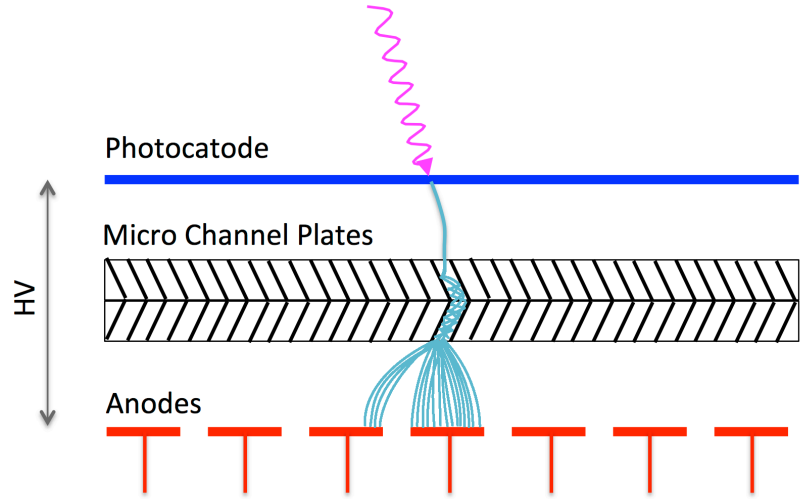

Figure 2.3: Schematic structure of an MCP-PMT. A photon (purple) hits the photocathode and produces an electron which generates an avalanche of secondary electrons which is collected by the anodes matrix.

in a 8×8 matrix (see Fig. 2.4). The size of a pixel is 5.9 mm with a pitch of 6.5 mm. The active area is 53×53 mm^2 with a total area of 59×59 mm^2. The MCP are manufactured with 25 μm channel diameter. The spectral sensitivity ranges from 200 to 650 nm with the maximum quantum efficiency of $\sim$ 24% at 380 nm, as shown in Fig. 2.5 (a). The common working voltage is between 1800 and 2400 V, with a corresponding gain between 10^5 and 10^7 (see Fig. 2.5 (b)). The average rise time of the PMT signal is 600 ps with a almost constant pulse width of 1.8 ns. The lifetime can reach up to 6 C/cm^2 when the MCP are coated using atomic layer deposition techniques [25]. The best timing resolution achieved for SP detection is $\sim$ 39 ps [49]. Further information about its lifetime, characterization and gain properties can be found in [25, 49].

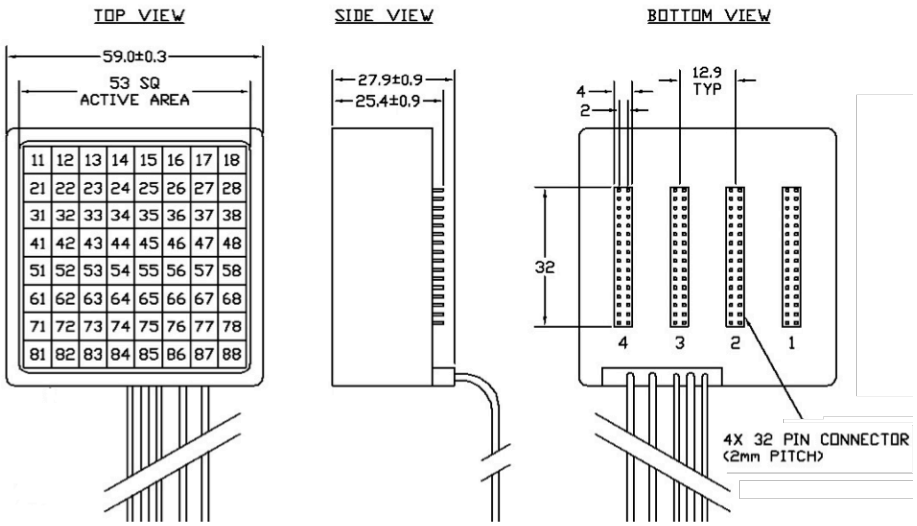

Figure 2.4: Design of the Planacon XP85012 MCP-PMT (units: mm): the 8×8 pixel matrix is shown in the top view. The output pins are grouped into four columns with 2 mm pitch [48].

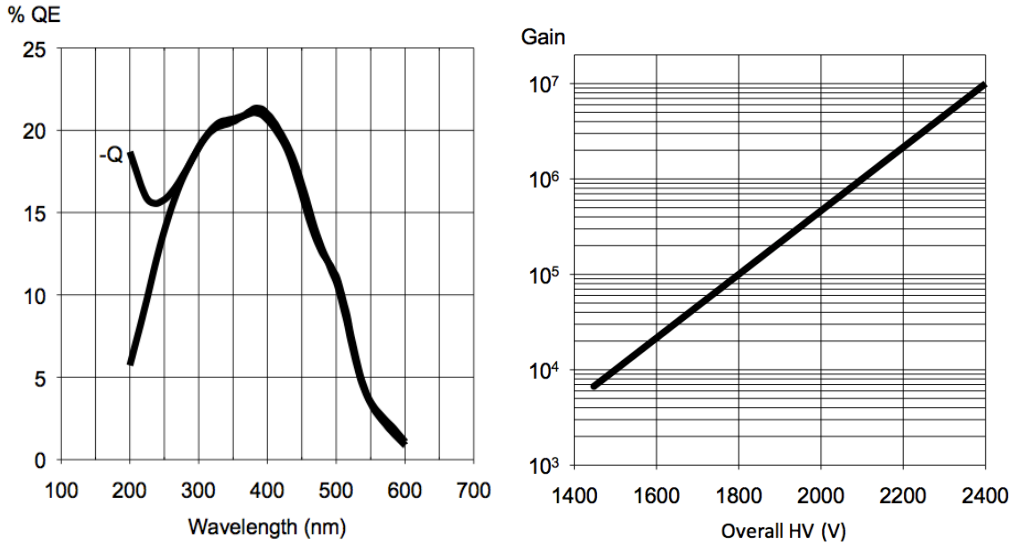

(a) (b)

Figure 2.5: Typical spectral response (a) and gain curve (b) of the XP85012 MCP-PMT [48].

2.1.2 Single photon calibration of MCP-PMTs

The characterization of MCP-PMTs was performed using the laser setup described in Section 2.1. A special mask designed to fit the rear pins of the XP85012, gave access to the readout of 32 (out of 64) channels through LEMO cables. A fast oscilloscope[3] with 2 GHz bandwidth and 10 GSample/s was used to acquire the output signals. The TTL signal provided by the laser control unit triggered the oscilloscope. The complete waveform of each signal was stored for detailed offline analysis. A dedicated software package developed in C++ for the ROOT framework from CERN [50] was employed for this test.

The first and essential test for SP measurements is the calibration of the

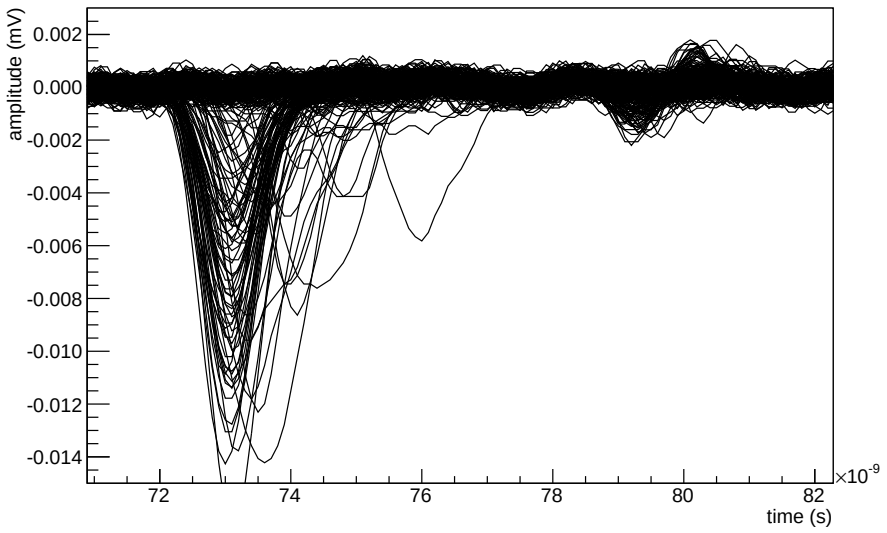

Figure 2.6: Typical MCP-PMT response for SP signals (overlay of 100 pulses) [51].

laser intensity to such low light levels. A NDF with a magnitude of 5.0 was used, for a corresponding attenuation of 10^5 according to Eq. 2.1. The laser frequency was set to 10 kHz, and the beam spot was centred on one of the central pixels of the MCP-PMT. Fig. 2.6 shows the overlay of 100 waveforms, $V(t)$ of the illuminated pixel. The deposited charge, Q, of a SP in the pixel

[3]Tektronix DPO5204 Digital Phosphor Oscilloscope

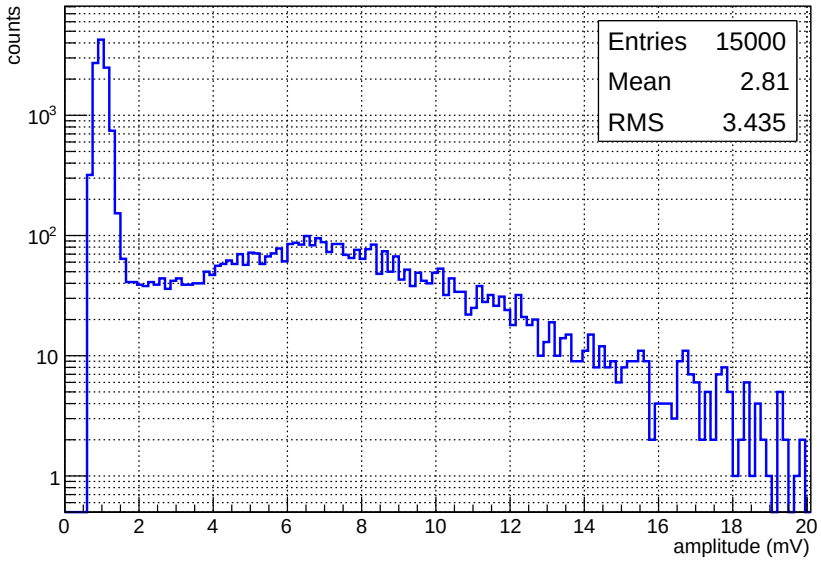

Figure 2.7: Amplitude spectrum of SP events [51].

anode can be expressed as:

$$Q = \int \frac{V(t)}{R} dt, \tag{2.2}$$

where R is the termination resistivity, which is 50 Ω. As first approximation, considering a triangular shape, the integral can be evaluated as follows,

$$Q = \frac{V_{max} \cdot t_{width}}{2 \cdot R} \;\rightarrow\; V_{max} = \frac{2 \cdot R \cdot Q}{t_{width}}, \tag{2.3}$$

where V_{max} is the maximum amplitude of a pulse and t_{width} its time width. Running the MCP-PMT at a gain $g \sim 10^6$ the expected charge for an SP event is $Q = e \cdot g \approx 160$ fC, with $e \approx 1.6 \cdot 10^{-19}$ C, the elementary charge. Taking the typical value of 1.8 ns for t_{width}, V_{max} is expected to be on average around 8-9 mV, which is qualitatively confirmed by the waveforms overlay (Fig. 2.6). The logarithmic spectrum of the amplitude shows an average amplitude of about 7 mV (see Fig. 2.7). The peak at ~ 1 mV is due to pedestal and refers to low voltage signals, which may occur, for example, due to leakage currents. Considering NDF>5.0 the position of the SP peak does not move and

together with the previous calculation qualitatively proves that a SP level is achieved with a 5.0 NDF.
The rigorous calibration of the absolute amount of light impinging on the MCP-PMT was performed exploiting the technique described in [52]. The idea of this method consists in a deconvolution of the photodetector charge spectrum and in the use of some of the extracted parameters for calibration purposes. Under real circumstances, only a fraction of the incident photons on the photocathode is picked up by the PMT. As a consequence, the number of converted photons is not a constant but a Poisson distributed variable. The conversion of photons into electrons and the subsequent collection by the MCP structure can be considered as a random binary process. Thus, the distribution of the number of photoelectrons can be described as a convolution of Poisson and binary processes, leading to the expression:

$$P(n;\mu) = \frac{\mu^n e^{-\mu}}{n!}, \tag{2.4}$$

with μ defined as

$$\mu = mq, \tag{2.5}$$

where μ is the mean number of photoelectrons collected by the MCP, $P(n;\mu)$ the probability of observing n photoelectrons, m the average number of photons hitting the photocathode and q the quantum efficiency of the MCP-PMT. The response of the MCP avalanche mechanism is described by a Gaussian distribution:

$$G_1(x) = \frac{1}{\sigma_1\sqrt{2\pi}} \exp\left(-\frac{(x-Q_1)^2}{2\sigma_1^2}\right), \tag{2.6}$$

where x is the extracted charge, Q_1 the average charge output of the MCP process for SP electrons, and σ_1 its standard deviation. Q_1 can be expressed as $Q_1 = e \cdot g$. The charge distribution for a process where n independent photoelectrons are considered, is the convolution of n SP electrons:

$$G_n(x) = \frac{1}{\sigma_1\sqrt{2\pi n}} \exp\left(-\frac{(x-nQ_1)^2}{2n\sigma_1^2}\right). \tag{2.7}$$

The response of an ideal MCP-PMT can be defined as a convolution of Eq. 2.4 and 2.7:

$$S_{ideal}(x) = P(n;\mu) \otimes G_n(x) \tag{2.8}$$

$$= \sum_{n=0}^{\infty} \frac{\mu^n e^{-\mu}}{n!} \frac{1}{\sigma_1\sqrt{2\pi n}} \exp\left(-\frac{(x-nQ_1)^2}{2n\sigma_1^2}\right). \tag{2.9}$$

Possible noise sources usually are divided into two categories:

I. low charge processes which affect all events and are responsible for the non-zero level of the signal distribution (e.g. leakage current, among others);

II. discrete processes which can accompany the real signal (like thermionic-emission, radioactivity, etc.).

A Gaussian can describe (I) while an exponential decay can be used for (II). The detailed calculation shown in [52] leads to an expression for a realistic response of the photomultipliers:

$$\begin{aligned} S_{real}(x) \approx \Big\{ & \frac{1-w}{\sigma_0\sqrt{2\pi}} \exp\left(-\frac{(x-Q_0)^2}{2\sigma_0^2}\right) \\ & + w\Theta(x-Q_0)\cdot\alpha\exp\left(-\alpha(x-Q_0)\right)\Big\} e^{-\mu} \\ & + \sum_{n=1}^{\infty} \frac{\mu^n e^{-\mu}}{n!} \cdot \frac{1}{\sigma_1\sqrt{2\pi n}} \cdot \exp\left(-\frac{(x-Q_0-Q_{sh}-nQ_1)^2}{2n\sigma_1^2}\right), \end{aligned} \tag{2.10}$$

where w is the probability that a noise signal of type (II) occurs within a SP event, α is the coefficient of the exponential decay (for (II)), Θ is a step function and σ_0 is the standard deviation of type (I) background. $Q_{sh} = w/\alpha$ is interpreted as the effective spectrum shift due to noise.

The charge spectrum of the MCP-PMT has been fitted with Eq. 2.10. Fig. 2.8 shows the result for a NDF of 5.0, where $n_{max} = 3$ photoelectrons was considered for the fit because higher contributions are negligible. The results show an average number of photoelectrons per laser pulse of $\mu \approx 0.35$, confirming the calibration of the setup to SP level.

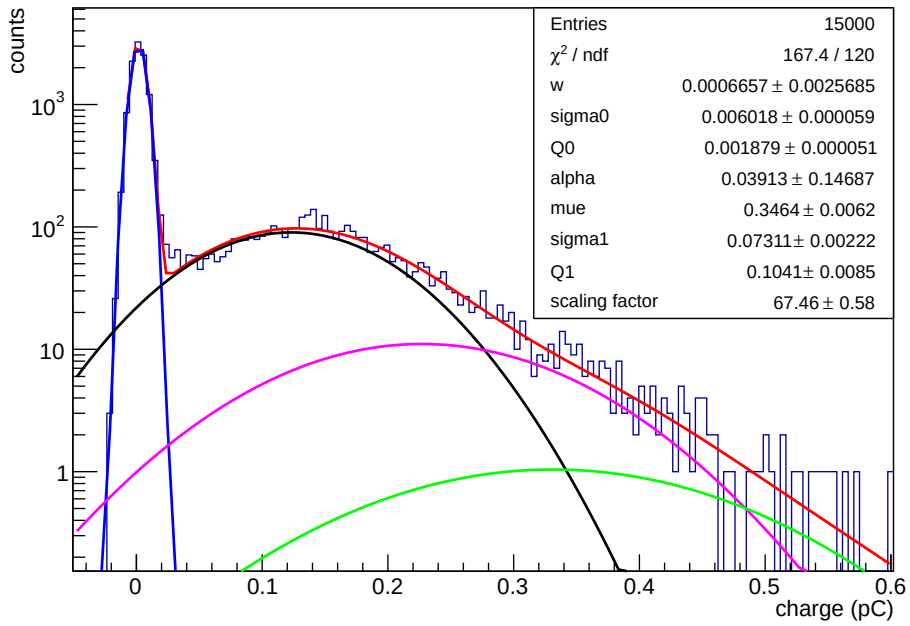

Figure 2.8: Logarithmic charge spectrum of the MCP-PMT under SP laser illumination. The data have been fitted with Eq. 2.10 and they show on average 0.36 photoelectrons per event [51].

2.1.3 Signal properties of MCP-PMTs

The established SP level allowed a systematic study of the signal characteristics expected in Cherenkov detectors. As the data-sheet of XP85012 reports [48] , the pulse width of the signals is expected to be almost constant. The waveforms overlay shown in Fig. 2.6 qualitatively confirms this and allows the definition of a simple mathematical approach, using the assumption that MCP-PMT signals can be described by an isosceles. Fig.2.9 shows an ideal signal, where b is the constant pulse width, A the signal amplitude and T the threshold level. As Eq. 2.3 states, the amplitude is proportional to the charge Q and can be written as follows:

$$Q = \frac{b}{2} \cdot A, \tag{2.11}$$

where R has been neglected for simplicity. This hypothesis is demonstrated by a straight line fit to the charge profile as a function of the amplitude, as

shown in Fig. 2.10 (for the scatter plot see Fig. A.1). The practical consequence is the equivalence between the measurement of charge and amplitude, which has to be taken into account for the FEE realization. For NDFs smaller

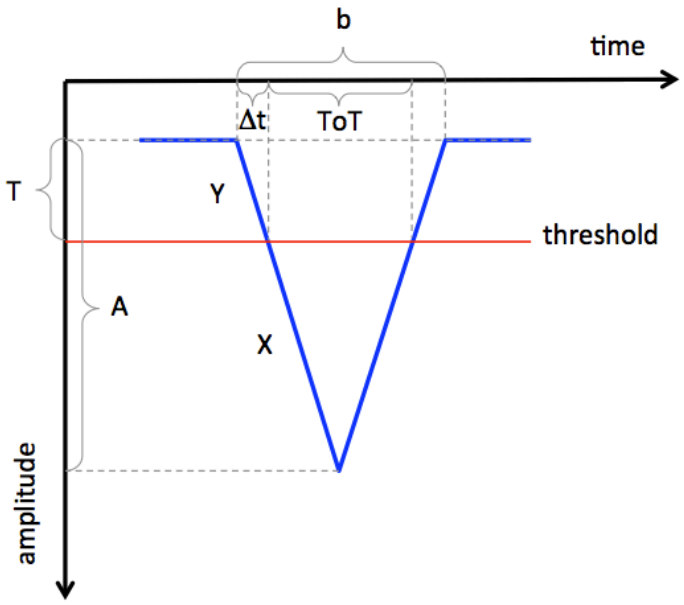

Figure 2.9: Schematic view of an MCP-PMT signal. In this model the pulse shape is considered as an isosceles triangle.

than 5.0 it was possible to observe the same linear relation between charge and amplitude, extending the validity of the assumption to higher photon statistics. The results for NDF 4.0 are shown in appendix A, Figs. A.2 and A.3; for NDF 3.0 see Figs. A.4 and A.5. The same model allows the definition of ToT with the following expression:

$$\frac{ToT}{b} = \frac{X}{X+Y}, \tag{2.12}$$

where X and Y are two parts of the oblique side (see Fig. 2.9). The equation can be rearranged by applying Pythagoras's theorem. Carrying out the

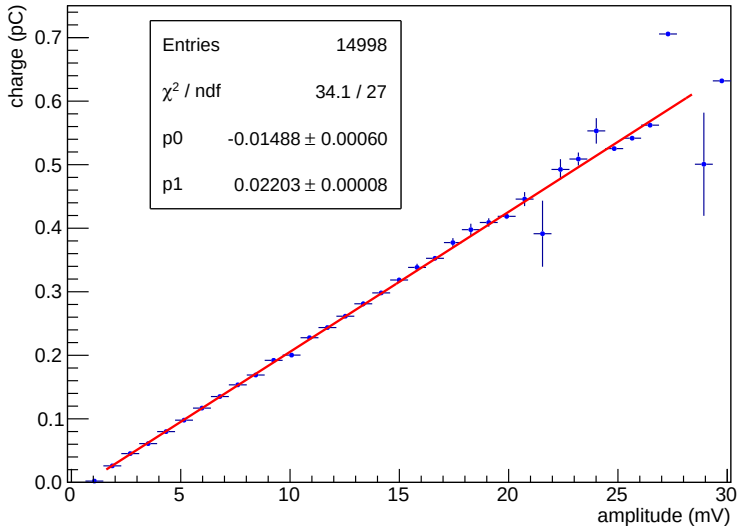

Figure 2.10: Charge profile as function of the signal amplitude. The linear fit demonstrates the equivalence between the two quantities [51].

calculations,

$$\frac{ToT^2}{b^2} = \frac{(A-T)^2 + (ToT/2)^2}{A^2 + (b/2)^2} \rightarrow ToT = b \cdot \left(1 - \frac{T}{A}\right) \rightarrow$$
$$ToT = b \cdot \left(1 - \frac{2bT}{Q}\right), \quad (2.13)$$

which expresses the relation between ToT and charge Q. The equation was used to fit the ToT profile as a function of the charge, shown in Fig. 2.11, where the parameter p0 is the pulse width b, p1 the threshold level T and p2 a possible offset of the charge. The result displays a good agreement with the model, especially at low charge values. The gradual change in the slope reduces the sensitivity, making it more difficult to reconstruct the charge from the ToT. The shape is also threshold dependent as shown in Appendix A (Fig. A.6–A.7), making the charge measurements more difficult for a discriminator-based FEE.

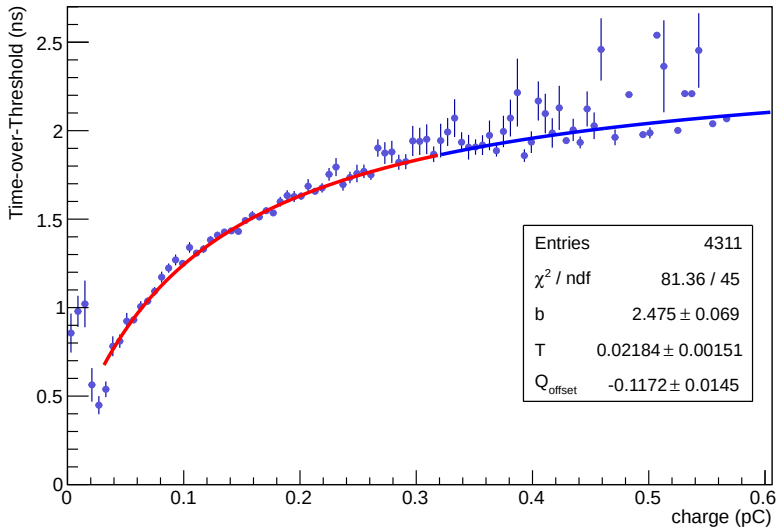

Figure 2.11: ToT as a function of the signal charge. Curve is a fit according to Eq. 2.13 where the red part indicates the fit range [51].

2.1.4 Time-walk

The phase of a discriminator output for signals with constant rise time depends on the amplitude of the input itself. This effect is known as "time-walk" and it usually limits the achievable timing resolution. The spread generated by time-walk on the threshold crossing point is illustrated in Fig. 2.12.

The model presented in the previous section was used to study the relation between the time-walk and the amplitude. Defining Δt as the time interval from the real start of the signal to the start defined by the threshold (see Fig. 2.9), it is possible to write:

$$\Delta t : T = \frac{b}{2} : A, \tag{2.14}$$

which with the result of Eq. 2.11 gives:

$$\Delta t = \frac{Tb^2}{4Q}. \tag{2.15}$$

This shows an inverse proportionality of Δt with respect to the charge Q. The equation was used to fit the profile of the arrival time shown in Fig. 2.13.

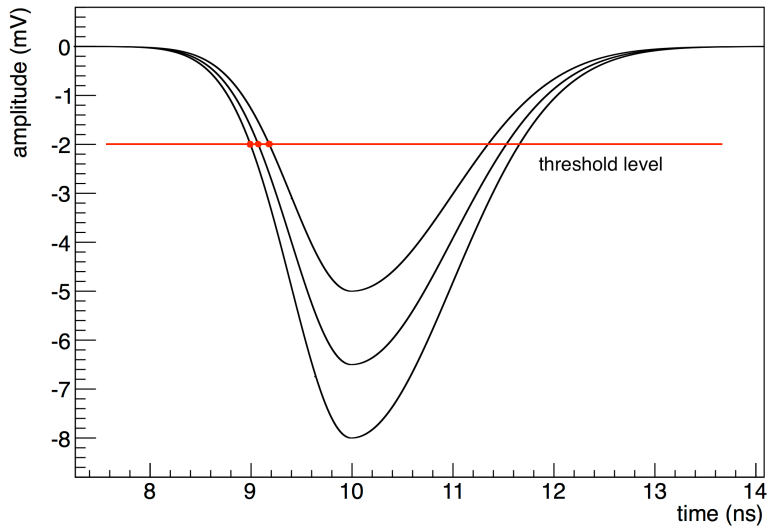

Figure 2.12: Time-walk effect for threshold triggering in case of MCP-PMT-like signals.

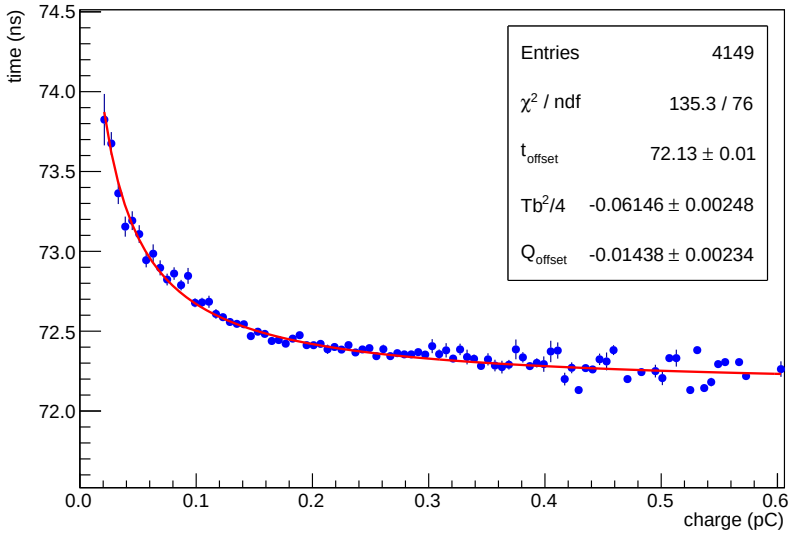

Figure 2.13: Profile of the arrival time as function of the deposited charge. A fit with Eq. 2.15 is performed (red line).

The agreement is good and it indicates that the charge can be used for walk correction. The result shows also that the time-walk is less important at high charge values.
The unique characteristics of the MCP-PMT signal enable another approach to the time-walk. The isosceles shape allows to express Δt directly through the ToT:

$$\Delta t = \frac{1}{2}\left(b - ToT\right). \tag{2.16}$$

The relation is linear and the scatter plot of the arrival time as function of ToT in Fig. 2.14 supports this. Focussing to a ToT range between $\sim 1-2$ ns, characterized by higher statistics, the profile of the arrival time shows a good agreement with the model (see Fig. 2.15). The outcome clearly demonstrates that a FEE with discriminator logic and ToT is not only enough for MCP-PMTs but also desirable when a time-walk correction is needed.
The bandwidth of the oscilloscope used for the tests was enough for the characterization of the photomultipliers, but was not ideal for the measurement of timing resolutions under 100 ps. This investigation is better described in Chapter 4, together with the effect of time-walk corrections.

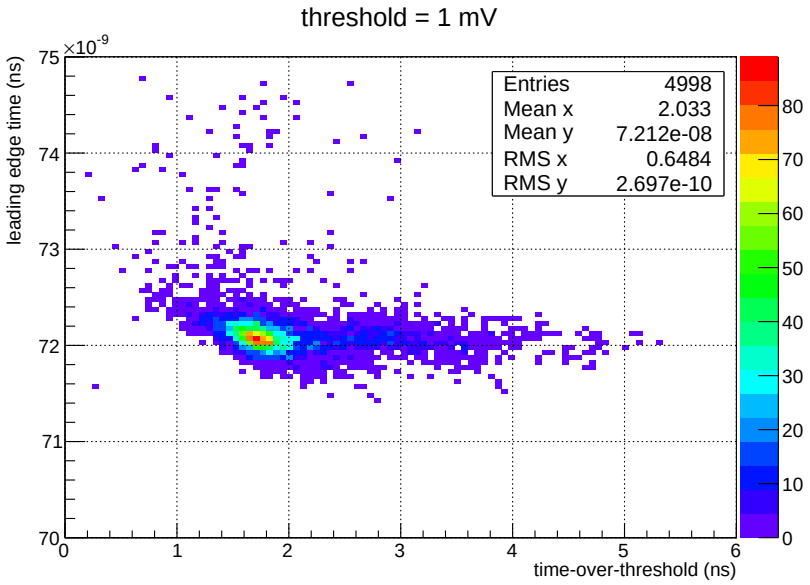

Figure 2.14: Scatter plot of the arrival time as function of the ToT for an MCP-PMT under SP conditions (colors according to the intensity).

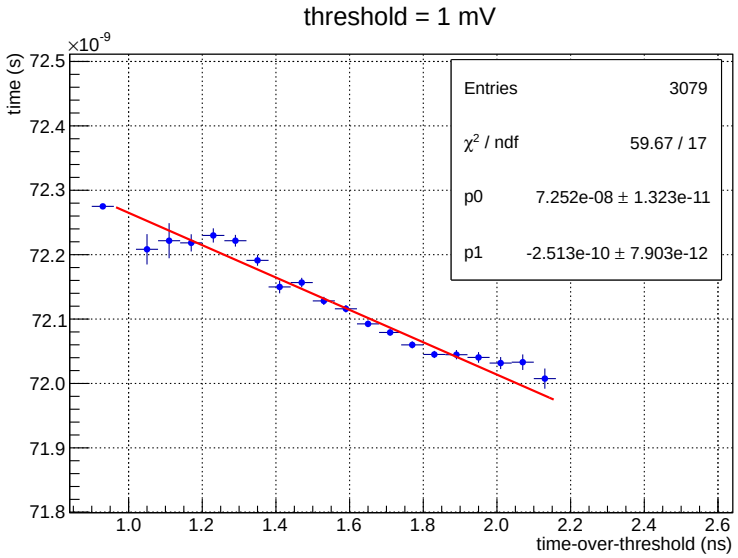

Figure 2.15: Profile of Fig. 2.14. A linear fit shows a good agreement between the data and the triangle-like model for MCP-PMT signals.

2.2 Characterization of scintillator signals

Scintillation light collected by a photomultiplier, unlike SP events, usually produces large and long output signals. In this case, the choice of fast PMTs is not important because the characteristics of the signals are mainly driven by the considered scintillators. For this reason, the characterization of such signals was done using a standard PMT, coupled to one bar of the neutron detector described in Chapter 1. The studies were performed using a single channel PMT in order to remove any possible effects stemming from cross-talk. In particular, the 64 channel MAPMT foreseen for the neutron detector was replaced by a Photonis XP2900 featuring similar gain, spectral and time response.

The MIP signals produced by cosmic muons were used for a detailed analysis of the detector response. The schematic view of the cosmic ray setup used for the characterization is shown in Fig. 2.16. The three WLSs coming from the scintillator bar were directly connected to the PMT window with a simple adapter. Optical grease was applied to improve the connection. The PMT was readout by a fast oscilloscope (same as in Section 2.1.2). Two scintilla-

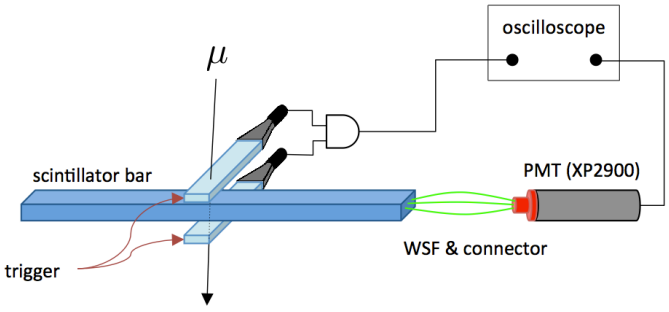

Figure 2.16: Schematic view of the cosmic ray setup.

tor strips, readout by standard PMTs, were placed above and below the NDet bar in order to select muons with a vertical direction. The small dimensions (H × L, 1 cm × 4 cm) of these strips allowed the definition of a restricted acceptance area. A coincidence generated by muons triggered the oscilloscope. Because of the low muon rate at sea level ($I \approx 1$ cm^{-2}min^{-1} [53]) and the narrow acceptance area, several days of running were required to collect sufficient statistics. The whole setup was made light-tight with a dark cover to exclude possible noise sources arising from ambient light. Although the rate is quite low, cosmic muons are optimal to study the scintillator response under light conditions similar to a test experiment. They provide MIP-like signals very similar to background electrons in the NDet. Therefore, the response to MIPs is of key importance to the understanding of the detector.

2.2.1 Laser calibration of the PMT

The PMT response was first investigated with SP signals. The information obtained in this section was later used for an estimation of the absolute amount of light produced by MIPs in a prototype bar. Knowing the charge collected by the anode in SP events allows the evaluation of the light yield by measuring the charge for MIP events. The laser system described in Section 2.1 was used to characterize the response of the XP2900, set to an operating voltage of 1400 V. A NDF of 5.0 was used to achieve SP conditions.

The calibration of the PMT response was performed with the same technique presented in Section 2.1.2. The logarithmic charge spectrum under SP laser illumination is presented in Fig. 2.17. The fit function is described by Eq. 2.10, under the hypothesis of observing a maximum number of pho-

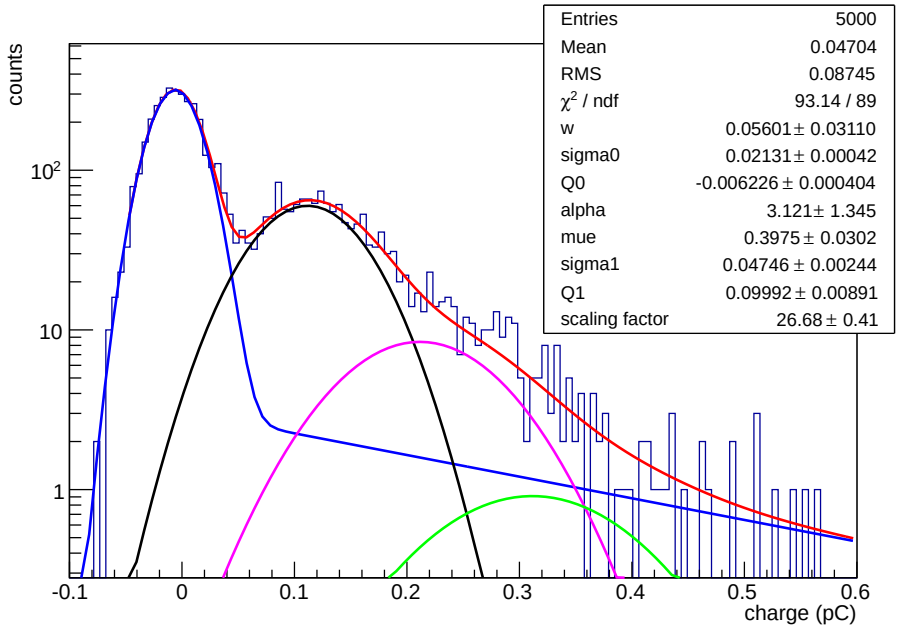

Figure 2.17: Logarithmic charge spectrum of the XP2900 under SP laser illumination. The data are fit with Eq. 2.10 and show an average of 0.39 photons per event.

tons n=3. The result shows a good agreement with the data. The charge associated with SP events was calculated as:

$$Q_{SP} = Q_0 + \frac{w}{\alpha} + Q_1 \approx 0.11 \text{ pC}, \tag{2.17}$$

where Q_0, w, α and Q_1 were extracted by the fit. The obtained value is used in the next section to extract the amount of light associated with MIP signals.

2.2.2 MIP signal properties

The high voltage of the XP2900 was set to 1400V in order to match the gain of the Hamamatsu 64 ch PMT. The trigger scintillators were placed around the middle of the prototype bar (approximately at 40 cm from the phototube). Two days of data taking were necessary to collect sufficient statistics. An overlay of 100 MIP signals is shown in Fig. 2.18 (a). Compared to the SP

waveforms observed for the MCP-PMTs, the signals do not appear regular and with a clear defined shape. The intensity chart in Fig. 2.18 (b) shows a better view of the average shape. The pulse width is in general larger than 20 ns while the amplitude can reach values up to 30 mV (with peaks larger than 40 mV). The largest signals also indicate the presence of after pulses in the decay tail, which could deteriorate the resolution of discriminator-based FEE. In general, the scintillator output cannot be represented by a simple triangular shape. Instead, the rising part is usually described with an inverse gaussian and the falling part is modelled with the combination of a fast and a slow exponential decays [54].

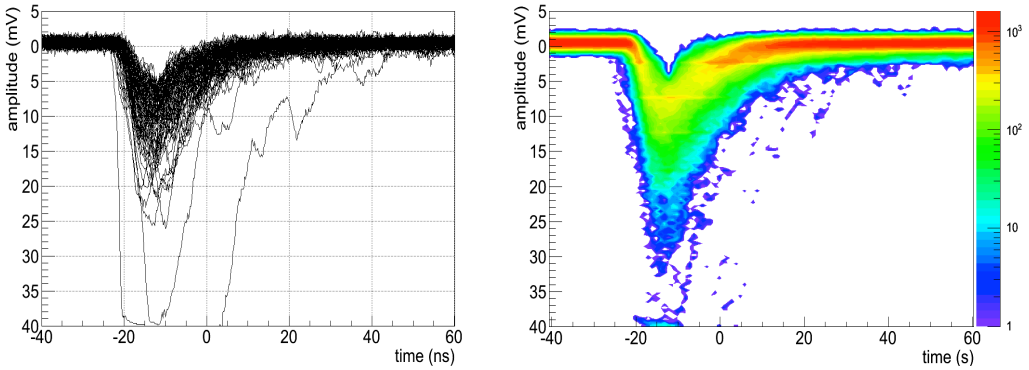

(a) (b)

Figure 2.18: (a) response of the PMT to MIP signals (overlay of 100 waveforms). (b) intensity chart of the same overlay.

Nevertheless, as first approximation a simple exponential function can be used to describe the pulse shape $V(t)$ (see Fig. 2.19):

$$V(t) = \begin{cases} 0 & t < 0 \\ V_0 \cdot e^{-t/\tau} & t \geq 0 \end{cases} \tag{2.18}$$

where V_0 is the maximum amplitude and τ a decay constant. Neglecting impedance, the integral of $V(t)$ determines the charge and is proportional to the maximum amplitude. The hypothesis is confirmed by Fig. 2.20, in which the charge obtained by waveform integration is drawn as function of the absolute amplitude. A fit with a quadratic polynomial shows negligible impact of the parameter $p2$, confirming the expectations. As in the SP case,

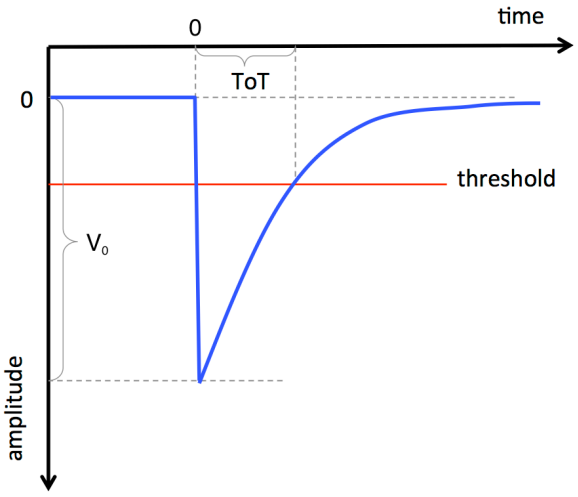

Figure 2.19: Simple exponential model for scintillation signals.

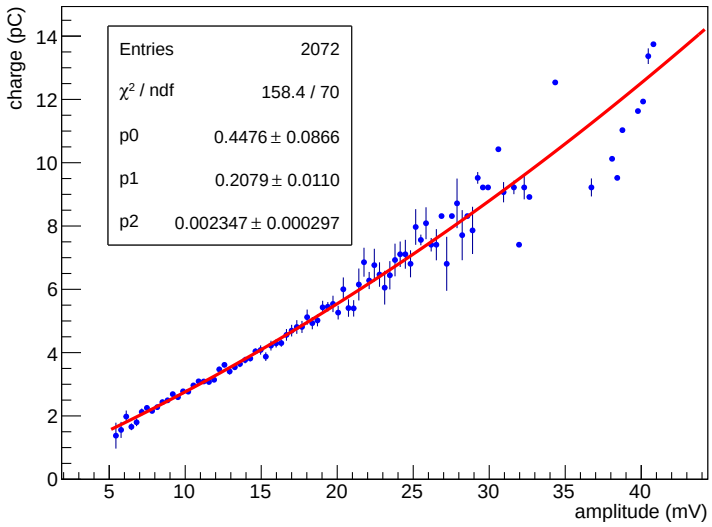

Figure 2.20: Charge distribution for MIPs as function of the pulse amplitude. The quadratic polynomial shows negligible impact of $p2$ proving a good linearity.

the results prove that the amplitude measurement is equivalent to the integral

of the signal. Considering a fixed threshold, V_{thr}, Eq. 2.18 can be written as

$$V_{thr} = V_0 \cdot e^{-ToT/\tau} \tag{2.19}$$

which leads to:

$$V_0 = V_{thr} \cdot e^{ToT/\tau}. \tag{2.20}$$

The last equation connects the maximum amplitude V_0 with the ToT of the signal. The charge Q is proportional to V_0, therefore:

$$Q \propto e^{ToT/\tau}. \tag{2.21}$$

Using the MIP data, the charge distribution as function of the ToT was measured by applying a threshold cut at -5 mV. The result (see Fig. 2.21) shows a good agreement with Eq. 2.21 and the parameter τ qualitatively fits the decay constant of WLSs. Further tests revealed that the linear approximation can be used also at different threshold levels, as qualitatively shown in Appendix A.8. This result shows that the ToT can be used as a simple ADC. Of course the precision cannot be compared to a direct charge measurement but opens a possibility for discriminator-based FEE. A recent study [55] shows how dynamic thresholds and trapezoidal shaping can substantially increase the performance of ToT for scintillator signals.

The absolute amount of light produced by MIP events can be estimated with the charge spectrum of the signal (see Fig. 2.22). Using the mean value of the spectrum and the PMT calibration for SP (see Eq. 2.17), the number of photons per MIP, N_{ph}, is:

$$N_{ph} = \frac{Q_{MIP}}{Q_{SP}} \approx \frac{3.679 \text{ pC}}{0.11 \text{ pC}} \approx 33, \tag{2.22}$$

where Q_{SP} is the average charge for SP and Q_{MIP} the corresponding value for MIPs. The result clarifies the requirement of a high dynamic range for the FEE, which must be able to detect signals from a few dozens fC up to several pC.

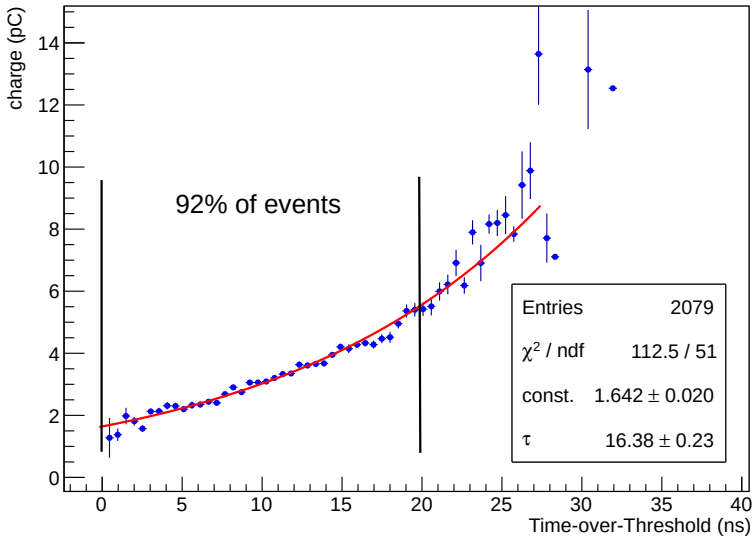

Figure 2.21: Charge distribution for MIPs as function of the pulse ToT. The data agree with the exponential model of Eq. 2.21. Within the grey lines also a simple straight line can be used for the fit.

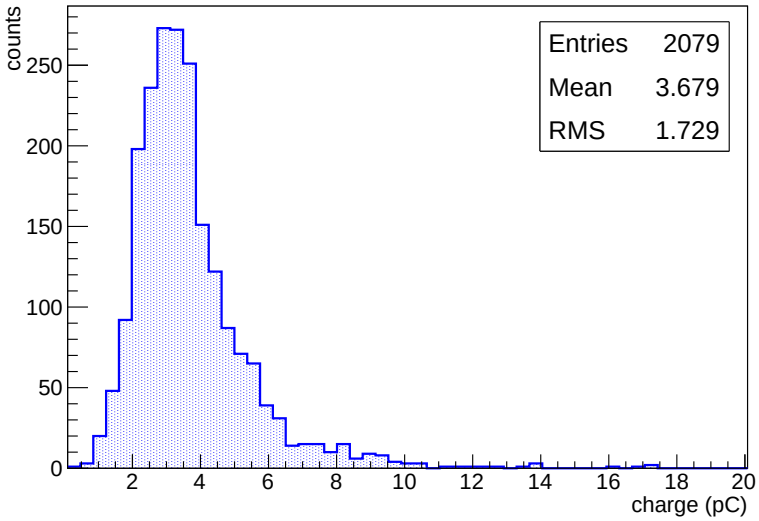

Figure 2.22: MIP charge spectrum of the PMT.

The obtained results are of crucial importance for the FEE design presented in the next chapter. The signal characterization defines the dynamic range of the FEE which has to cope with significantly different signals. These studies demonstrated that the ToT method can be successfully used for walk corrections of SP signals. The deposited charge in plastic scintillator can be measured with the signal ToT which acts as a simple ADC-method.

Chapter 3

Frontend Electronics Concept

The result of the signal investigation defined the fundamental requirements for the FEE design. In particular, high timing resolution needed for the DIRC requires walk correction which can be obtained with ToT. The readout of plastic scintillators with the same electronics, requires a large dynamic range as well as the capability to measure the charge. In addition, as summarized in Table 1.1 and 1.2, high count rates up to several MHz per channel are necessary.
The achievement of high performance does not only depend on the FEE but also on the digitization process which must be fast and precise too. In 2011 at the beginning of this thesis a novel DAQ system became available, the TDC Readout Board version 3 (TRB3). The TRB3 was chosen for its unique properties, high efficiency and versatility. The behaviour of the TRB3 was carefully investigated. Indeed, this was its first application requiring very fast timing. In consequence of the TRB3 choice, the FEE output has to be time-encoded and transmitted with Low Voltage Differential Signal (LVDS) logic, as schematically shown in Fig. 3.1.
In the following sections, after a detailed description of the TRB3, the FEE design and its basic characterization are presented.

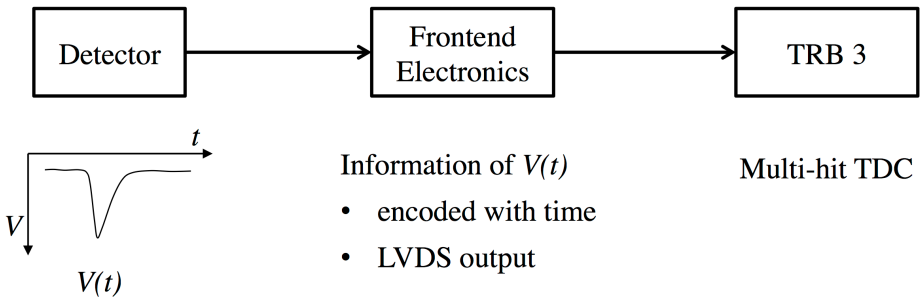

Figure 3.1: Block diagram of the FEE concept. The pulse $V(t)$ produced by a detector is processed by the FEE which encodes the information with a time signal in LVDS logic. The TRB3 acquires the FEE output with a precise TDC.

3.1 The TDC Readout Board 3

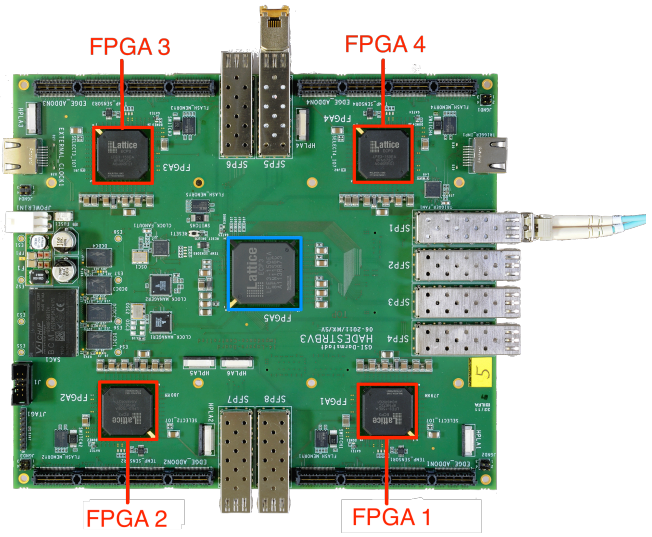

Figure 3.2: Photo of the TRB3 board. Four peripheral FPGAs (red) can be programmed as TDC or hub. A central FPGA (light blue) controls the board and acts as a CTS unit. Several connectors allows high versatility. Two ethernet sockets provide input and output trigger connections.

The TRB3 is a multi-purpose board based on TDCs implemented in FPGAs [56]. The board has been developed at GSI, with the intention to build a versatile

and low-cost system using commercial components. The innovative approach consists in "misusing" digital FPGAs in the analogue domain for the measurement of time, amplitude, and charge. Compared to traditional TDC ASICs with long and costly development cycles, FPGAs are readily available. The firmware of FPGAs can be easily adjusted to specific uses without the need for new hardware, opening the door to multiple applications. Last but least, they offer a high channel density at low cost. The TRB3, shown in Fig. 3.2, has five FPGAs, manufactured by Lattice[1] in 65 nm technology. The central FPGA acts as the Central Trigger System (CTS) and Gigabit Ethernet controller (GbE), providing data transfer and slow control connections. In this way, no CPU is needed keeping the system simple. The four peripheral FPGAs are programmed as TDCs. A total of 256 channels plus four for reference (64 + 1 per FPGA) can be achieved. The board features:

- a maximum hit rate of 50 MHz;
- a maximum trigger rate of 700 KHz for data readout;
- a maximum data rate transfer of 50 MBytes/s;
- eight Small Form-factor Pluggable (SFP) connectors for data transfer and control on board, each with 2 GBit/s;
- accepted input signals $\geq$500 ps;
- dead time $<$ 25 ns.

Several Add-on connectors (40/80-pin connectors, general purpose connectors, ADC Add-on and CTS Add-on) are available enhancing the versatility of the TRB3. The peripheral FPGAs can also be configured as hub, allowing the control of multiple TRB3 boards. The connection is realized via a specific Add-on board with SFP connectors. Several TRB3 boards can be easily connected together through one or more hubs. In this case, one TRB3 is configured as master and used for the trigger distribution and the slow control of the additional TRB3s (slaves). The data transfer can be configured both via the master TRB3 or with parallel GbE connections to a switch. The last option guarantees the highest data transfer rates. The system can be controlled via dedicated software (Trbsoft [57]) and the TrbNet protocol. The latter is a slow control system and a network set up with a DHCP server

[1]Lattice ECP3-150EA

running on a computer which also takes care of the event builder.
The readout can be set up in many different ways, either using an external source or an independent random pulser generated by the TRB3. A time window to filter the interesting events can be configured for each FPGA separately. The data are transmitted to the event builder through a dedicated User Datagram Protocol (UDP).
The TDC architecture is based on an interpolation method to guarantee high

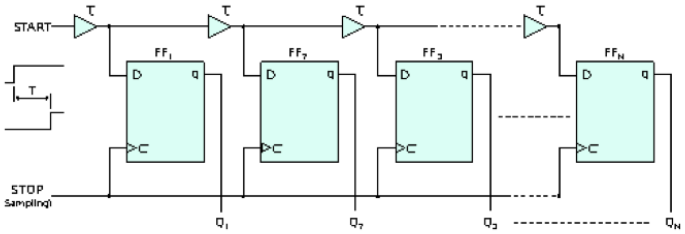

(a)

Figure 3.3: Tapped delay line method [56].

precision for a long measurement range. High timing performance is obtained by using a combination of a fine and a coarse time interpolator. The fine time measurements utilize the Tapped Delay Line method (TDL), fully explained in [58] and well suited to modern FPGAs. The intrinsic delays of logic elements inside the FPGAs are used to implement the TDL (see Fig. 3.3). When an LVDS pulse is received, the start signal propagates through the logic elements along the delay line. The rising edge of the stop signal (the coarse counter) samples the state of the delay line. The time t_f between start and stop is calculated as:

$$t_f = N_d \cdot t_d, \tag{3.1}$$

where N_d is the number of logic elements sampled by the stop signal and t_d the propagation time of a single logic element. The coarse time interpolator consists of a coarse counter and an epoch counter. The coarse counter is triggered by the system clock with a 5 ns period. The epoch counter is driven by the coarse counter overflow, occurring every $\sim$10.24 μs. Together, epoch and coarse counters extend the measurement range to $\sim$45 minutes. The information of fine (t_f), coarse (t_c) and epoch (t_e) time are used to calculate the time interval between two signals (1 and 2):

$$\Delta_t = (t_{e2} + t_{c2} - t_{f2}) - (t_{e1} + t_{c1} - t_{f1}), \tag{3.2}$$

The TRB3 requires a time calibration because the intrinsic propagation times (t_d) along the delay chain are not uniform. Typically, look up tables (N_d to time) are built using the raw data itself, so that each data file has its own calibration table. The time calibration, fully described in [57], is affected by temperature and voltage changes, thus requiring frequent updates. In general, the TRB3 achieves a typical timing precision of 7.2 ps RMS on a single channel, with a global timing better than 14 ps. However, for time differences it is important to emphasize that these outstanding performances can be obtained only between channels which belong to the same FPGA. When comparing channels from different FPGAs, a synchronization term must be considered (more detail in Section 3.1.1).
During the FEE development, a framework has been developed to unpack, calibrate and analyse the TRB3 data. All the presented results in the following chapters were obtained using this framework based on C++ and ROOT libraries. More information about the TRB3 and its applications can be found in [56, 59, 60].

3.1.1 Synchronization studies

The timing performance of the TRB3 depends on the position of the considered channels on the board. In particular, when the channels are within the same FPGA, the resolution is higher because the synchronization does not play any role on the time definition. On the other hand, channels on different FPGAs are affected by the precision of their respective reference channels. The synchronization precision was measured using a setup with a master and a slave TRB3. The random pulser from the CTS in the master board was used as trigger. The pulser was distributed to the slave board and sampled by the reference channels of the four peripheral FPGAs. The time differences between the different FPGA channels were computed and the timing precision was defined as the standard deviation of the data fit with a Gaussian distribution. Fig. 3.4 summarizes the results for the different combinations, where FPGA 1, 2, 3 and 4 are named according to Fig. 3.2. Fig. 3.5 **(a)** shows the best case which occurs between FPGA 1 and 4, providing an excellent $\sigma_{sync} \approx 13$ ps. The worst case is between FPGA 2 and 4 with $\sigma_{sync} \approx 42$ ps , and is shown in Fig. 3.5 **(b)**. A double peak structure is clearly visible and degrades the timing precision. The Gaussian fit does not represent a good description and for this combination (as well as for 2-3 and 2-1), the timing precision is defined by the RMS of the data. The other combinations are

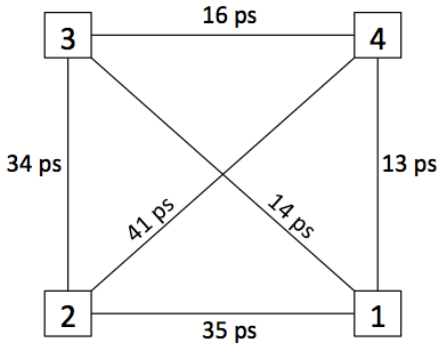

Figure 3.4: Synchronization time precision between the different FPGAs.

shown in appendix B.1 (Fig. B.1).

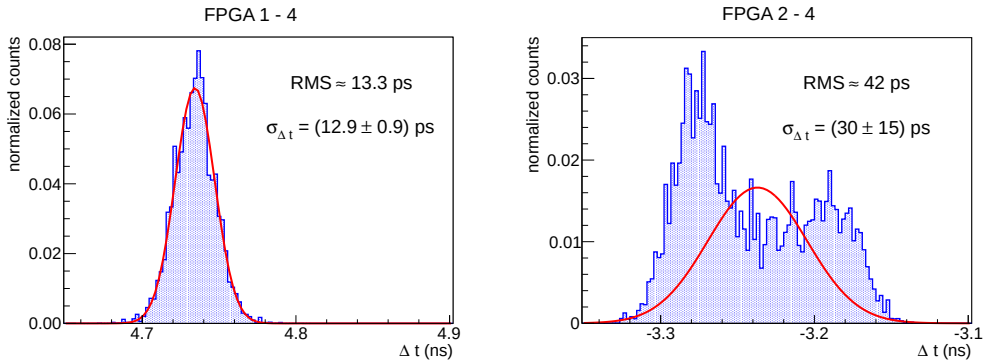

(a) **(b)**

Figure 3.5: Synchronization precision between FPGA 1 & 4 **(a)** and 2 & 4 **(b)**. The double peak structure in **(b)** is caused by the power supply close to FPGA 2.

The deterioration of the synchronization performance appears only when FPGA 2 is involved. After discovery of this behaviour, the reason was found to be a jitter induced by the DC-DC converters of the TRB3 (close to FPGA 2). Using an external linear power supply improves the average precision to approximately $\sigma_{sync} \approx 10$ ps. Future developments of the TRB3 will solve the issue directly on-board.
The synchronization between different TRB3 boards was measured in a similar

way. Precisions on the order of 100 ps were found. The best case (see Fig. 3.6) between FPGA 1 of the two TRB3s achieves 93 ps RMS. Further studies of the TRB3 group revealed the possibility to improve the synchronization to 30-40 ps by using an external reference clock distributed across the setup.

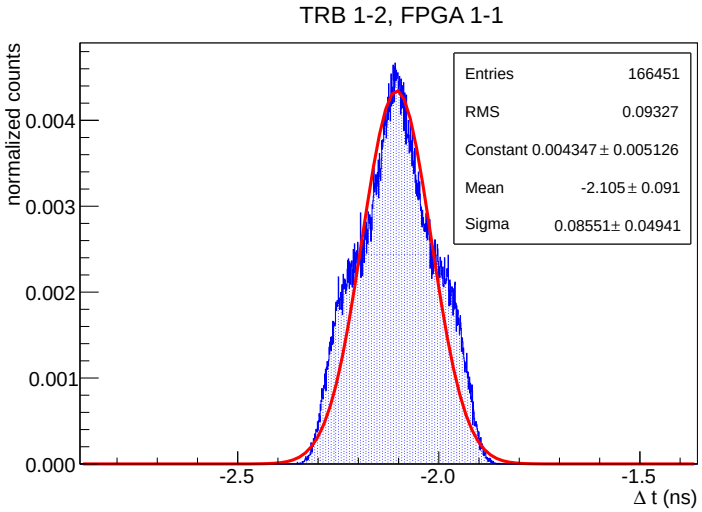

Figure 3.6: Synchronization precision between FPGA 1 of the two TRB3s.

3.2 Frontend Electronics Design

The key ingredients for the development of a multi-purpose FEE have been already discussed in Chapter 1.1. In particular the requirements set by imaging Cherenkov counters and plastic scintillator arrays were summarized in Table 1.1 and 1.2, respectively. In addition, the signal characterization in Chapter 2 showed that:

I. the FEE has to cope with small signals ($\approx$ 5 mV) typical of SP events;

II. a high dynamic range will be mandatory for the readout of plastic scintillators;

III. the measurement of ToT will enhance the timing performance for SP events by allowing a time-walk correction (see Section 2.1);

IV. the ToT can be used as a simple ADC, which especially for scintillator signals has not been considered before;

Ideally, electronics based on Waveform Digitizing ASICs would maximize the achievable timing resolution and give complete access to the pulse shape. However, extreme count rates ($\sim$ MHz) and a large amount of channels would demand a drastic reduction of the digitized information, also to avoid massive storage resources. Moreover, these ASICs are currently limited to triggered experiments with moderate rates. Indeed, the dead time for digitization does not allow a continuos readout, which is fundamental for high rate experiments [61, 62]. Last but not least, the cost of this relatively new technology is still high.

The easiest solution is an FEE logic based on discriminators. This choice requires no external trigger and offers small dead time of a few ns. Compared to common ADCs, a discriminator does not need any gate, and the threshold level is typically the only value to be defined. On the other hand, the charge measurement through ToT is not as precise as for an ADC and needs validation with the full readout. A modular design including Add-on cards enhances its versatility, e.g. the SP detection will benefit from a preamplifier to provide higher pulses to the discriminator. Alternatively, signal-shaping can improve the charge resolution via ToT measurements.
The selection of a suitable discriminator chip is of fundamental importance.

3.2.1 The NINO ASIC chip

Nowadays, high costs are inevitable for the development of new ASICs, as well as several years development for the realization of a stable product [6]. Furthermore, the present generation of available ASICs has already met high standards and performance. For this reason, it was decided to use a well known ASIC and upgrade its features according to the detector requirements. The NINO chip was selected as core component for the discriminator. This chip was developed by the Lepton Asymmetry Analyzer project at CERN [63, 64] and used for the resistive plate chambers of the ALICE ToF system.
The main specifications of the NINO chip are given in Table 3.1. The functional block diagram of one NINO channel is shown in Fig. 3.7. The input stage of the chip consists of a low-noise large-bandwidth circuit. A robust current-to-voltage converter sends the input signal to four identical cascaded

Table 3.1: Main characteristics of the NINO chip [63].

Parameter	**Value**
Peaking time	1 ns
Signal range	100 fC - 2 pC
Front edge time jitter	<25 ps RMS
Power consumption	30 mW/ch
Discriminator threshold	10 fC to 100 fC
Differential Input impedance (In)	$40\ \Omega < In < 75\Omega$
Output interface	LVDS
Sustained rate	$\gg$ 10 MHz

amplifiers, which provide enough gain to operate as a discriminator. The threshold is set by a voltage difference applied on two symmetrical inputs. A positive loop feedback adds a small hysteresis on the discriminator threshold. The whole circuit is differential and generates an LVDS output. The NINO chip has eight channels which fit in a 2×4 mm^2 ASIC processed in IBM[2] 0.25 μm CMOS technology. The NINO was chosen for its unique timing

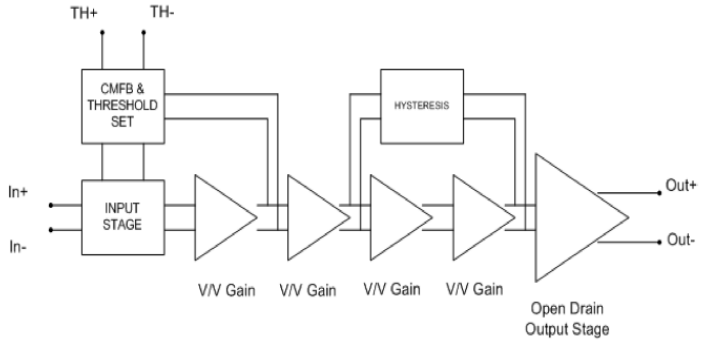

Figure 3.7: Functional block diagram for one channel of the NINO chip [63].

performances, low noise and low power consumption. There are no similar chips featuring triggerless logic, possibility to implement ToT measurement and radiation hardness. Several other experiments chose the NINO for the same reasons, among others the RICH of NA62 at CERN [65], the GRINCH detector of Hall A at JLab [66] and the future TORCH detector of LHCb at CERN [23]. Another reason to choose the NINO chip is its future develop-

[2]International Business Machines corporation

ment and availability. In particular, an improved 32 channels version is now available.

3.2.2 Discriminator card

The FEE was developed at the electronic department of the Institute of Nuclear Physics in Mainz. The characterization presented in Chapter 2 determined the specifications of this electronics.
The discriminator card was designed to be as compact as possible and to fit the Planacon MCP-PMT connectors. The discriminator card is a Printed Circuit Board (PCB) 8 cm long and 6 cm wide. A picture of the discriminator card is shown in Fig. 3.8, while the layout drawing can be found in appendix B.2. Two NINO chips per card (one per layer) are used for a total of 16 readout channels.
The output of common PMTs, including MCP-PMTs, is usually single-ended,

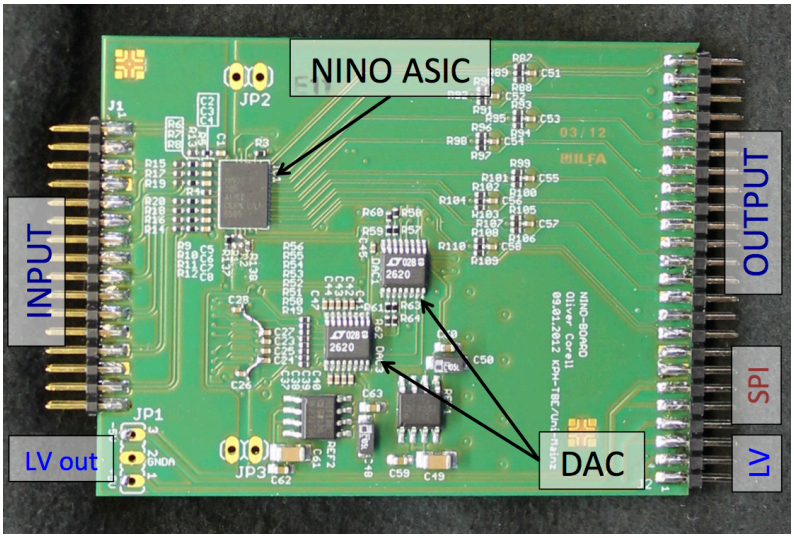

Figure 3.8: Top view of the discriminator PCB (8 cm long, 6 cm wide).

while the input of the NINO chip is differential. However, the chip can work in "single-ended mode" [67], where one channel input is connected to the PMT output while the other is left open (and internally grounded to the reference voltage).
Three commercial Digital to Analogue Converter chips (DACs) set the working parameters of the NINO chips: common thresholds, hysteresis and pulse

stretcher (offset for the input ToT). In addition, the DACs define voltage offsets (from 0 to 3.3 V) which are added to the inputs of each NINO channel. These offsets allow, for the first time, setting individual thresholds for every NINO channel, which, by design, only has one common threshold per chip. The communication with the DACs is via a Serial Peripheral Interface (SPI) connection. The output is fed through a specific adapter to the TRB3 DAQ. The card requires an operating voltage of +5V. The power consumption was measured to be about 70 mW/channel. Furthermore, the card provides the facility to power Add-on cards with ±5 V. As previously mentioned, this solution increases the possible uses of the discriminator; e.g. a preamplification stage or charge-to-time circuit could be easily connected. The detailed schematics of the discriminator card can be found in Appendix B.3, B.4, B.5 and B.6.
A backplane, whose drawings can be found in Appendix B.7, connects four discriminator cards (an entire MCP-PMT) together for the readout with the TRB3 via two 40 pin ribbon cables (16 pins are reserved for the SPI). The mother board takes also care of the power supply distribution to the boards. This solution was specifically designed for use with MCP-PMTs, but simple adapter boards can be used for the connection with different PMTs, as it will be shown in Section 4.2 and 5.2.

3.2.3 Preamplifier Add-on card

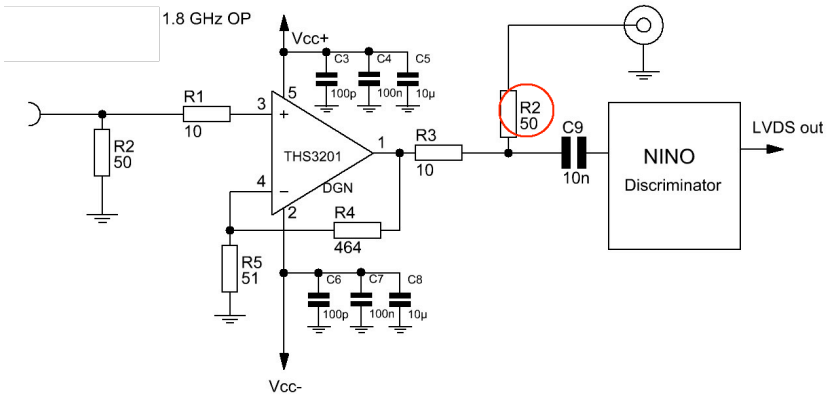

Figure 3.9: Preamplifier schematics for one channel. A 50 Ω termination is applied before the NINO chip.

SP measurements with MCP-PMTs, as seen in Section 2.1, usually deliver small and fast signals which require an amplification stage before the discriminator. A preamplifier Add-on card was designed for this scenario. The card, 4 cm long and 6 cm wide, has 16 channels (eight channels per layer) equipped with commercial CFAs[3] (Texas Instruments, THS3201, detail in [68]). An exhaustive explanation about the CFA working principles can be found in [69]. The schematics for one channel is shown in Fig. 3.9. Each channel provides about 20 dB gain, with 1.8 GHz unity-gain bandwidth. The card requires an operating voltage of +10 V, provided by the +5/-5 V connection to the discriminator PCB. Fig. 3.10 shows the preamplifier Add-on and the discriminator card together. The layout drawing and the complete board schematics are reported in Appendix, Fig. B.8, B.9, B.10 and B.11 respectively.
In SP events, the preamplifier shifts the input charge into a region ($>$ 200 fC) where the intrinsic charge-dependent jitter of the NINO is small [63].

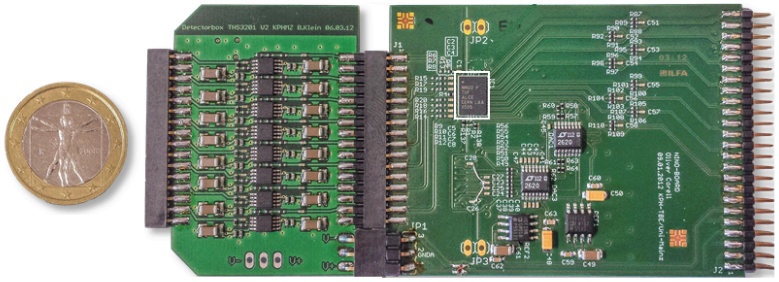

Figure 3.10: Preamplifier Add-on and discriminator cards connected.

The FEE design has an high versatility. Simple adapter masks can be realized for connecting the FEE to the pin layouts of different PMTs. The modular design allows the tuning of the dynamic range to the desired input.

3.3 FEE characterization

The FEE cards were characterized under controlled conditions to understand their basic properties, as well as to investigate the behaviour of the single-

[3]Current Feedback Amplifier

ended scheme with individual thresholds. Moreover, effects like charge saturation can be better studied using a stable pulse rather than PMT signals. The discriminator and the preamplifier cards were tested using a programmable fast pulse generator[4] (2 GS/s and 250 MHz bandwidth). The readout was realized with a fast oscilloscope (same as in Section 2.1.2), so that the complete waveforms were available for offline analysis. The characterization of the full readout chain will be discussed in Chapter 4.

3.3.1 Preamplifier characterization

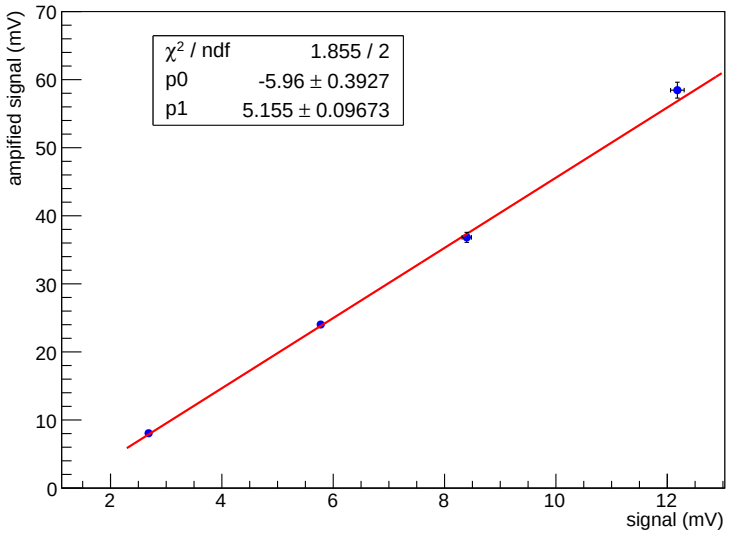

Figure 3.11: Amplitude response of the preamplifier Add-on card to MCP-PMT-like pulser signals.

The preamplifier cards are designed for the SP detection. Consequently, the characterization with fast and small signals is of particular interest. The typical shape of the MCP-PMT response to single photons was reproduced with the pulser using two Gaussian distributions. The standard deviation of the first gaussian represented the rising part of the signal and was set to $\sigma_1 = 0.6$ ns. The second distribution took into account the decay time of the signal, with a standard deviation set to $\sigma_2 = 1.2$ ns.

[4]Tektronix AFG3252

The pulse generator was set to "burst mode", in which a single pulse per trigger was sent to the FEE with an adjustable frequency. In particular, a value of 100 kHz was used to study the performance with a rate similar to the Barrel DIRC requirements.
The data in Fig. 3.11 show the amplitude response to different pulse heights. The trend is linear and returns a gain value $p_1 \approx 5.2 \pm 0.1$. The result agrees with the design value of 20 dB considering the 50 Ω termination before the output (see Fig. 3.9).

3.3.2 Discriminator characterization

The NINO chip, as explained in 3.2.2, has four amplification stages. The common threshold is not applied at the input stage and setting the levels is not straightforward. Neither the NINO documentation [64] nor the main publication [63] clarify the conversion factor between the voltage required by the chip and the effective threshold level. Moreover both of them express the threshold in terms of input charge instead of voltage. For these reasons the discriminator card had to be carefully characterized. Particular attention was given to the calibration of the individual thresholds described in Section 3.2.2. The discriminator card was tested together with the preamplifier to check the FEE response for SP applications.
Ideally, if a signal with a given amplitude exceeds the set threshold, the FEE produces an output signal, whereas smaller signals are rejected. This step response is commonly described by the Heaviside Step Function $H(t)$ [70], which in this case can be expressed as:

$$H(t) = \begin{cases} 1 & \text{if } t < A \\ \frac{1}{2} & \text{if } t = A \\ 0 & \text{if } t > A \end{cases} \tag{3.3}$$

where t is the threshold and A is the signal amplitude. For real signals, the slope becomes a ramp which depends on the circuit characteristics. The FEE step function $H(t)$ was measured as the ratio between the number of accepted signals and the number of input pulses. Short (ToT ~2 ns) rectangular pulses with variable amplitude were used as input. The results for five different amplitudes are shown in Fig. 3.12.

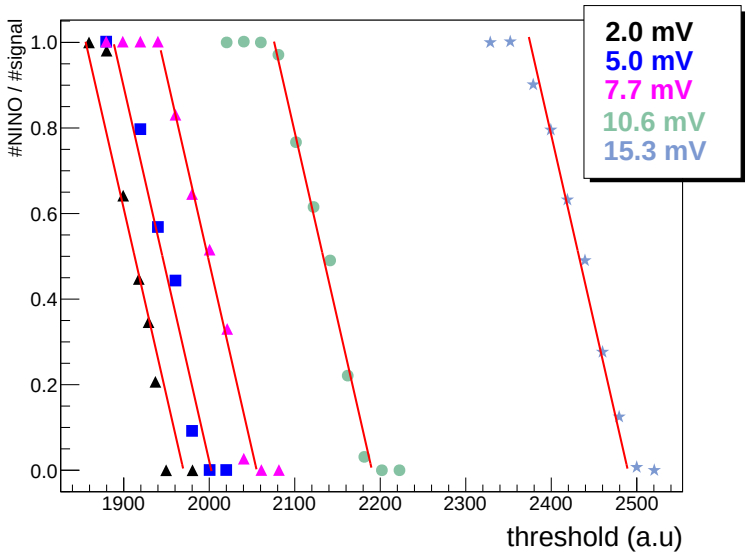

Figure 3.12: FEE feedback to signal inputs at different threshold levels, in agreement with the model of Eq. 3.3. Linear fits denote the characteristic slope of the circuit from which t_{amp} is extracted.

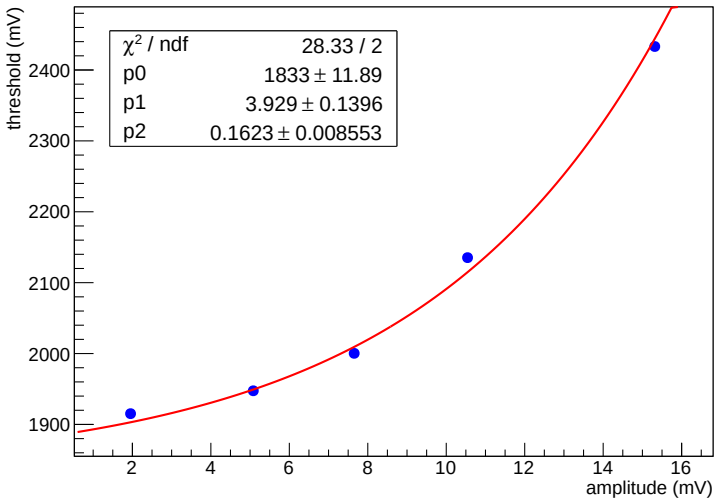

Figure 3.13: Correlation of signal amplitude and individual threshold voltage setting for a single channel.

In first approximation, the slopes can be described by straight lines. In particular, a fit using a fixed slope parameter shows good agreement for all amplitudes. The calibration between voltage levels and real input thresholds was measured defining t_{amp} as $H(t_{amp}) = 1/2$. The value of t_{amp} was then plotted as function of the pulse amplitude, as shown in Fig. 3.13. The relation is clearly non-linear and can be approximated with the following exponential function:

$$t = p_0 + \exp(p_1 + p_2 \cdot amplitude). \tag{3.4}$$

The equation allows the precise setting of the threshold levels to the desired input amplitude.

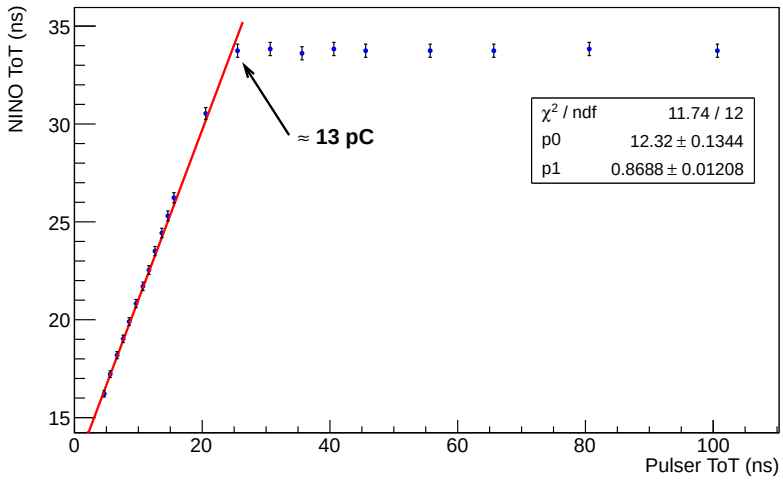

Figure 3.14: NINO response to a square pulse with different widths. The saturation of the FEE (preamplifier and discriminator cards) occurs at 13 pC.

The NINO chip has a 2 pC charge input limit [63]. However, the range measurement reported in [63] shows the response up to $\sim$ 1 pC only. Moreover, the behaviour of the chip for signals exceeding this limit is not clear, and the simulation used in the paper does not describe input charges larger than 1 pC. The ToT behaviour of the discriminator cards was analyzed choosing rectangular pulses with fixed amplitude and variable width as input. Fig. 3.14 shows the ToT of the NINO output as function of the input width of the pulser signal. The data are perfectly linear up to almost 25 ns, which corresponds to an input charge of 13 pC, well above the reported 2 pC. At this

value, the FEE exhibits a saturation effect on the ToT. The dynamic range is thus 13 pC/100 fC = 130. This result is particularly useful for multi-purpose applications where high dynamic range is desiderable.
Observations showed a linear response for $ToT \gg 100$ ns with $q < 13$ pC. More tests revealed that the leading edge time at saturation can be used up to an input charge of about 300 pC, while higher charge values introduce after-pulse effects on the output. Of course, the input charge can be tailored by using appropriate Add-on cards.

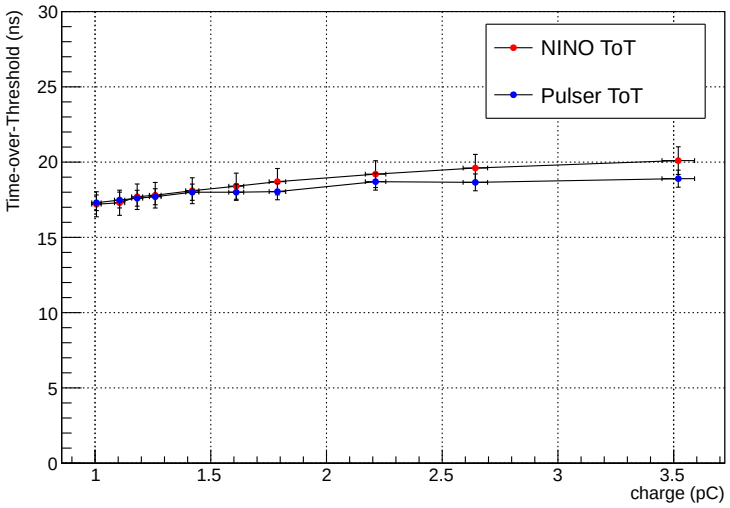

Figure 3.15: NINO ToT response as function of the input charge generated by a pulse generator.

Another characteristic not well clarified by the available literature on the NINO is whether its response is proportional to the input charge or to the signal width [64, 67]. The proof that the NINO chip encodes only the signal width was found using a square pulse with fixed width and variable amplitude. Varying the amplitude corresponded to varying the input charge, which was measured directly by an oscilloscope. Fig. 3.15 shows the NINO output ToT as function of the input charge. As expected, the ToT of the NINO output signals does not depend on the input charge. The original width is well reproduced by the NINO output within the error bars, demonstrating that a simple discrimination is performed by the chip.

The performed studies prove that the FEE works properly. The threshold levels were calibrated and the response of the electronics, as expected, is proportional to the width of the input signals. The FEE has a high dynamic range which is useful for several applications. The results lead to the characterization of the full readout chain which is presented in the next chapter.

Chapter 4

Readout Characterization

The full readout chain was studied to determine the performance of the FEE. Similar investigations to those presented in Chapter 2 were carried out using the FEE and the TRB3 DAQ, which were introduced in Chapter 3. The tests were particularly focussed on the SP performance, which is the most challenging requirement and needs fine tuning of the electronics parameters (e.g threshold level). The timing response was thoroughly studied, especially the viability of time-walk corrections using ToT information.
Furthermore, a characterization of the system using scintillator arrays was performed. In this case, attention was paid to the dynamical range of the discriminator card and possible effects from saturation of the NINO chip.

4.1 FEE response to Single Photon Signals

Investigations of the FEE using SP signals were carried out with the pulsed laser setup described in Section 2.1. A scheme of the setup is shown in Fig. 4.1. An MCP-PMT was instrumented with four FEE cards including preamplifier Add-ons. The DAQ system comprised two TRB3 boards, one master and one slave. The former was programmed as CTS and hub for data taking and slow control. Two of the four peripheral FPGAs from the slave board were connected via a specific Add-on to the MCP-PMT with two 40-pin flat cables. The FPGAs were programmed with a 64 channel TDC design[1], in which each input channel is split into two TRB3 channels: even and odd channels measure the leading edge time and the trailing edge time, respectively.

[1]Version 1.5, peripheral FPGA TDC (June 2013)

A third peripheral FPGA was connected to a General Purpose input (GPin) Add-on, with LEMO input connectors and Nuclear Instrumentation Modul-Standard (NIM) to LVDS converters [57]. The TTL trigger of the laser source was first converted to NIM logic and then split. The first output was translated to LVDS logic with a Levcon box (developed at GSI [71]) and sent to the external trigger of the TRB3. The second output was connected to the GPin Add-on for a precise measurement of the trigger time.

SP conditions (∼0.3 γ/trigger) were guaranteed by the optical scheme de-

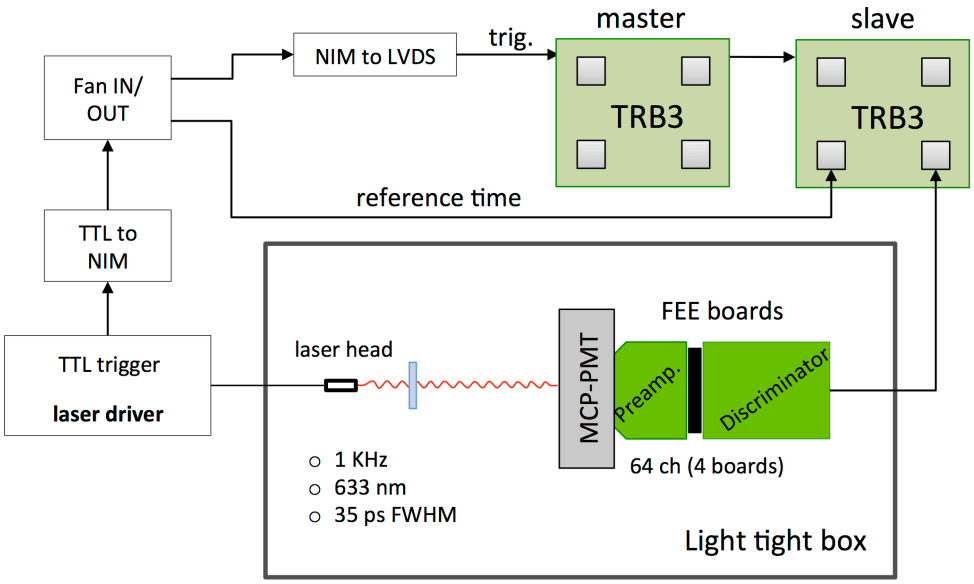

Figure 4.1: Schematics for the full readout test using fast laser setup calibrated to SP.

scribed in Section 2.1.2. For all the tests, the MCP-PMT was set to a gain of 10^6.

4.1.1 General response

The laser setup was first used to investigate the global properties of a MCP-PMT. A test of the cross talk was performed by focussing the laser beam onto a central pixel. The result is shown as an intensity histogram in Fig. 4.2 (a). The colours and numbers represent the number of hits registered for pixel, in a run of approximately 8 minutes at a rate of 1 kHz (approximately 480,000 events). The central pixel, as expected, collects the majority of the events,

while the other pixels have a low number of counts. In particular, the ratio between its number of events $N_p = 161712$ and the total $N_{tot} \approx 480000$ is

$$N_p/N_{tot} \approx 0.33, \tag{4.1}$$

which agrees with the expected photon statistics. Fig. 4.2 (b) shows the imaging for ND 3.0, which corresponds approximately to 30 photons per trigger (for a total of about 50,000 events). In this case the peripheral pixels have a higher number of counts, as intuitively expected from the higher photon statistics. Defocussing of the laser was also performed to verify the correct response of the MCP-PMT, as shown in Fig. 4.3.
In general, the results show small cross talk between the channels. This is of major importance for imaging detectors like the Barrel DIRC. The imaging response of the full readout chain to Cherenkov patterns will be described in Chapter 5.

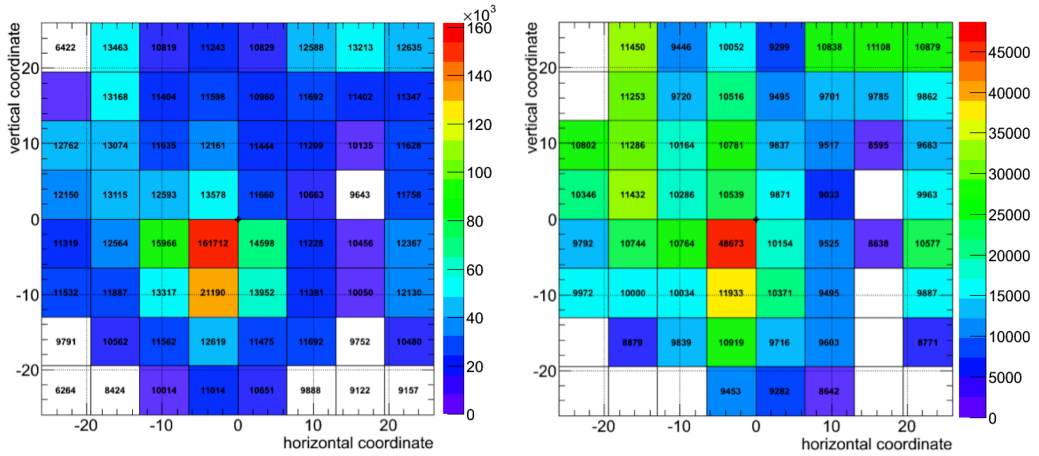

(a) (b)

Figure 4.2: Intensity plot of the MCP-PMT with the laser spot focussed in the centre: (a) at ND 5.0 (approximately 500,000 events), (b) at ND 3.0 (approximately 50,000 events).

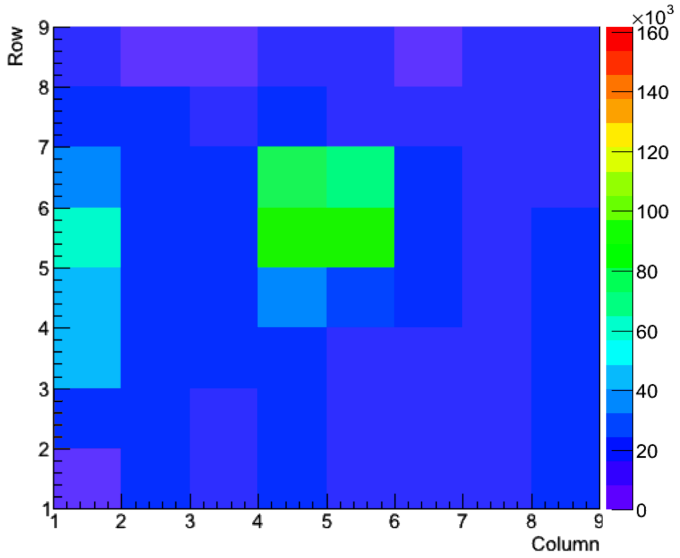

Figure 4.3: Intensity plot of the MCP-PMT with the laser defocussed laser spot around the centre. This image was produced using Go4, another analysis software package available for the TRB3 [72]

The general timing response of the MCP-PMT was investigated considering all the channels. The arrival time of the photons on the pixels was defined as:

$$t_{arr} = t_{pix} - t_{trig}, \tag{4.2}$$

where t_{pix} is the synchronized time of a chosen pixel and t_{trig} is the trigger time. Fig. 4.4 shows t_{arr} as a function of the channel number. The correlation between the laser trigger (red spot at [128, 0 ns]) and the entire MCP-PMT is clear, allowing the definition of a tight window around the relevant hits. In this way, dark count events can be significantly reduced in the analysis. The average arrival time differs for each pixel. The effect is caused by:

I. the different response of the NINO chips;

II. the different circuit paths inside the TRB3;

The misalignment can be solved for I and II by an offline calibration with the laser data.

In general, the ToT spectrum depends on the threshold level as shown by the simple MCP-PMT model introduced in Chapter 2. The ToT can be expressed as a function of the threshold T according to Eq. 2.13. Ideally for SP

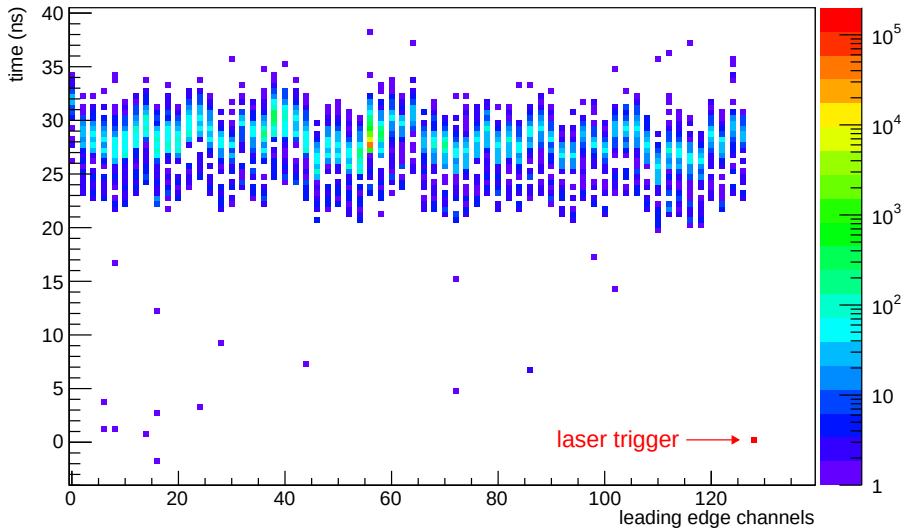

Figure 4.4: Scatter plot of the photon arrival time as a function the channel number.

signals the measured ToT is constant at the lowest threshold settings, while for higher levels the ToT should decrease linearly with the threshold as shown in Eq. 2.13. Fig. 4.5 shows the result for an individual threshold of 1.9 V, which corresponds to 2 mV at the FEE input (see Fig. 3.13). The average value is almost 13 ns, where 12 ns are due to the NINO pulse stretcher. Similar spectra were produced at different threshold levels. The average ToT as function of the threshold level is shown in Fig. 4.6. The plateau at low thresholds indicates a pulse width of about 2.5 ns, qualitatively in agreement with the parameter of the XP85012 MCP-PMT (see Section 2.1.1). Starting at ∼1.1 V the decrease of the measured ToT is clearly linear, as predicted by the model. At higher thresholds like 2.5 V (16 mV at the input stage) almost no signal is left.

The definition of a proper working threshold is driven by detection efficiency. This is particularly important for detectors like the Barrel DIRC, where the low light yield per track demands to detect as many photons as possible.

As already done for the NINO characterization in Section 3.3.2, the Heaviside function $H(t)$ can be used as model for the detection efficiency. In this

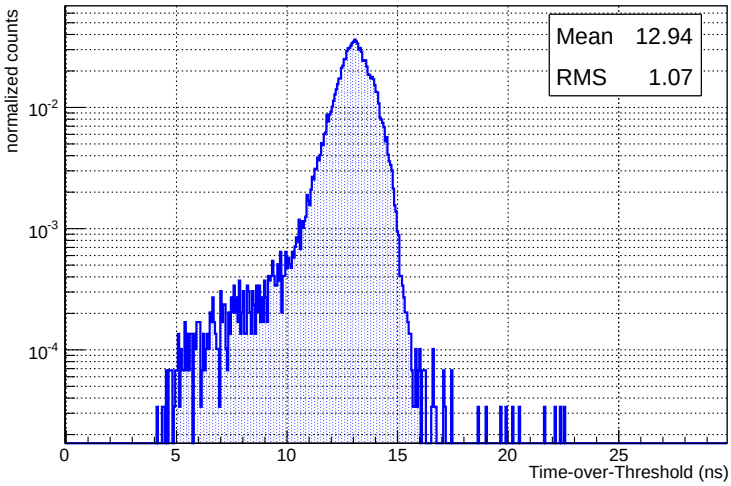

Figure 4.5: Time-over-threshold spectrum of a single MCP-PMT channel at a threshold level of 1.9 V.

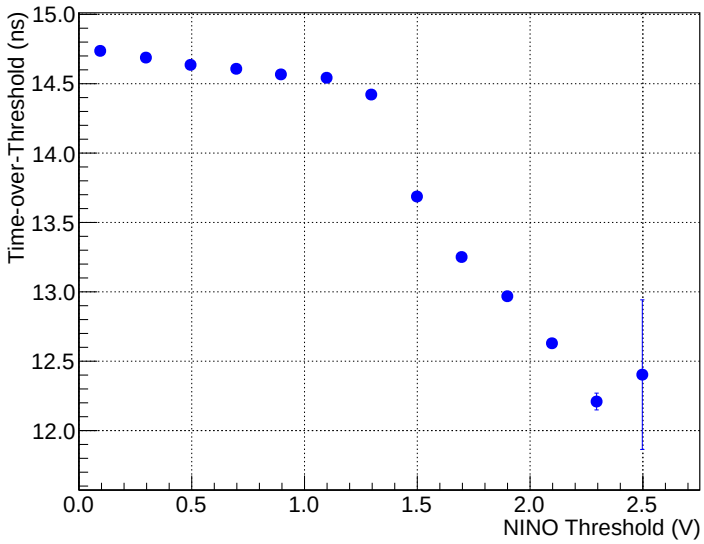

Figure 4.6: Time-over-Threshold response to MCP-PMT signals as a function of the NINO threshold.

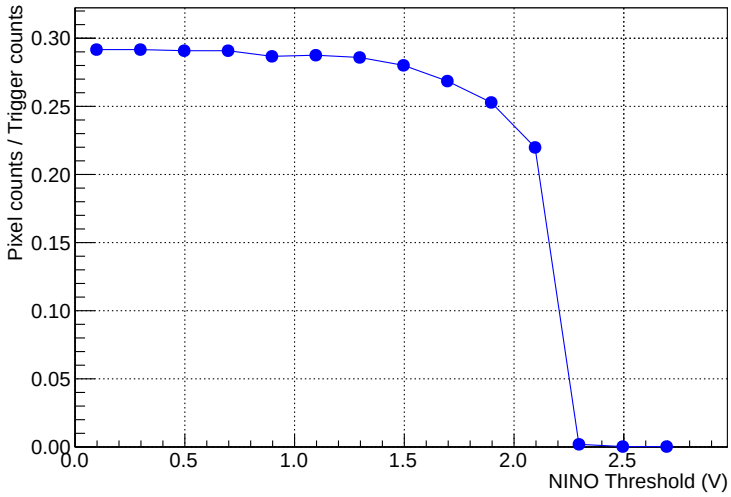

Figure 4.7: Detection efficiency at different threshold levels.

case H(t) is defined as:

$$H(t) = \begin{cases} \mu & \text{if } t < A \\ \frac{\mu}{2} & \text{if } t = A \\ 0 & \text{if } t > A \end{cases} \tag{4.3}$$

where μ is the average number of photoelectrons per laser pulse (see Section 2.1.2) and A is the average SP signal amplitude. Varying the thresholds, $H(t)$ was measured by the ratio:

$$H(t) = \frac{\text{registered hits}}{\text{number of triggers}}. \tag{4.4}$$

The result in Fig. 4.7 shows a good agreement with the model. In particular, $\mu \sim 0.3$ agrees with the photon level found in the calibration of the MCP-PMT in Section 2.1.2, and demonstrates a FEE efficiency for SP close to one.
Taking into account $H(t)$ and the result in Fig. 4.6, thresholds on the order of 1.1-1.3 V can be considered optimal for SP detection.
These studies are crucial for the follwing test experiment which is described in Chapter 5.

4.1.2 Timing performance

The small FWHM of the laser pulse ($\sigma_{laser} \approx 35$ ps) allows a precise study of the timing performance. In first approximation, ToT can be considered proportional to the arrival time of the photon, as previously shown in Section 2.1.4. The high precision of the laser trigger signal allows to define Δt

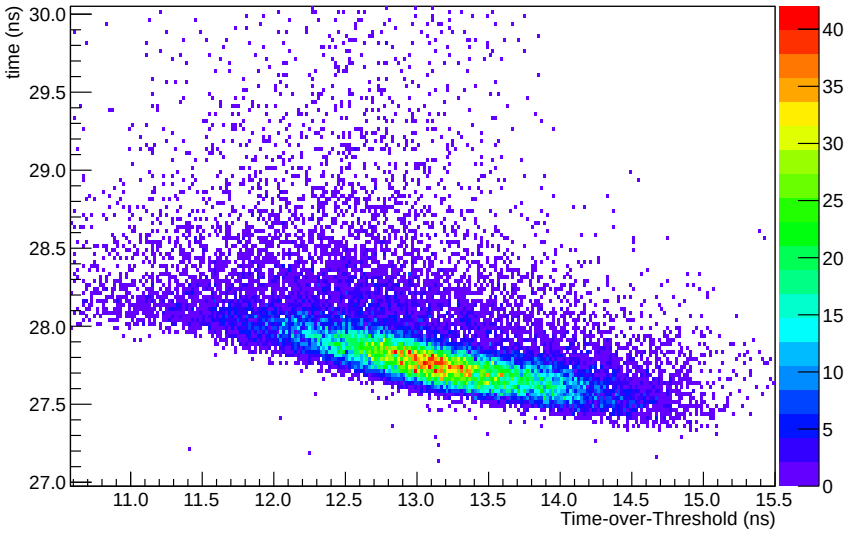

Figure 4.8: Arrival time of photons as function of measured ToT [73].

of Eq. 2.16 with the time difference $t^{'}$ between the arrival time of the photon and the trigger time:

$$t^{'} = \frac{1}{2}\left(b - ToT\right) + \text{const.} \tag{4.5}$$

Fig. 4.8 shows the time $t^{'}$ as a function of the ToT for a threshold level of approximately 2 mV. The plot clearly demonstrates that the FEE is able to reproduce the result obtained by the oscilloscope studies. A similar behaviour was found for different threshold levels. The profile of the distribution in Fig. 4.9 was used to extract the parameters for a time-walk correction. The linear fit is in good agreement with the data, especially for 12 ns $< ToT <$ 14 ns (around 90% of the events). The corrected time t_{cor} can be expressed as:

$$t_{cor} = t^{'} - q - m \cdot ToT, \tag{4.6}$$

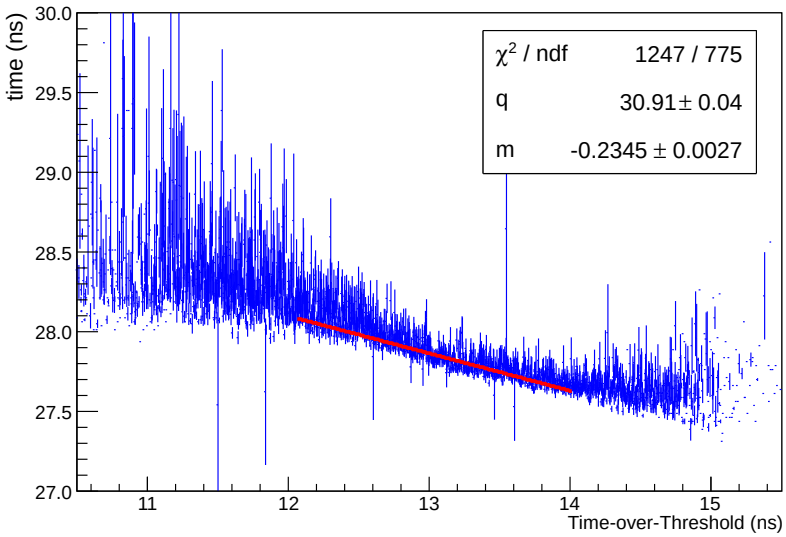

Figure 4.9: Profile of Fig. 4.8. A linear fit is applied in a range containing 90% of the events.

where q and m are the fit parameters. Fig. 4.10 (a) shows the uncorrected arrival time $t^{'}$ of the laser photons on the MCP-PMT. A fit of the narrow peak up to 28 ns with a Gaussian function gives a standard deviation $\sigma_{fit} = 134.6 \pm 0.9$ ps. The time spectrum after the time-walk correction is depicted in Fig. 4.10 (b). The peak after correction is distinctly narrower and a gaussian fit returns a standard deviation $\sigma_{fit} = 90.9 \pm 0.5$ ps. In both cases the fit is limited to the peak region in order to exclude the back scattered photoelectrons inside the MCP-PMT, which generate the tail in the right part [49]. The exclusion of the tail limits the detection efficiency, but for detectors like the Barrel DIRC the photon statistics are sufficient to compensate this. In first approximation, σ_{fit} can be considered as the quadratic sum of independent components:

$$\sigma_{fit} = \sqrt{\sigma^2_{MCP} + \sigma^2_{FEE} + 2 \cdot \sigma^2_{TDC} + \sigma^2_{sync} + \sigma^2_{laser} + \sigma^2_{trigger}}, \qquad (4.7)$$

where $\sigma_{MCP} \approx 39$ ps [49] and $\sigma_{sync} \approx 13$ ps (see the synchronization studies in Section 3.1.1). The TDC resolution is $\sigma_{TDC} < 11$ ps [60] and needs to be considered twice because of the relative timing between MCP-PMT and laser. The laser contribution is described by both the $\sigma_{laser} \approx 35$ ps FWHM and

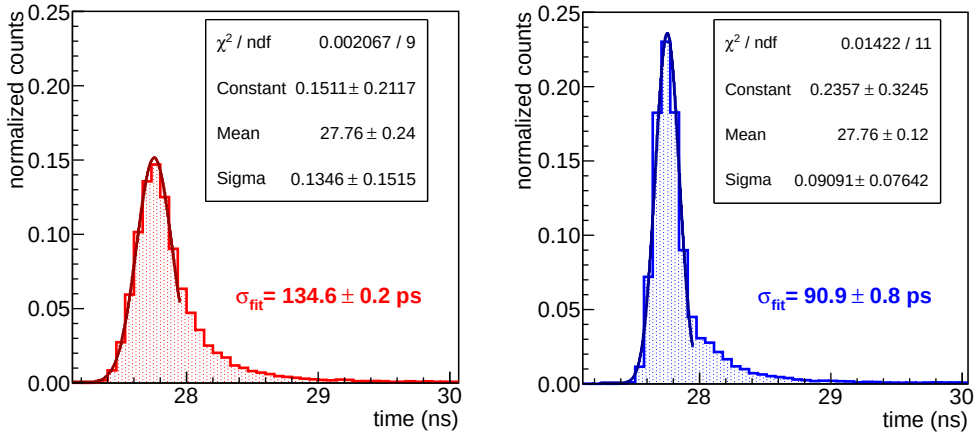

(a) (b)

Figure 4.10: Time spectrum before (a) and after (b) time-walk correction. Back-scattered electrons inside the MCP-PMT generate the tail on the right.

$\sigma_{trigger}$. The latter arises from the trigger logic which was used to convert the TTL trigger of the laser pulser into the NIM input for GPin connector. Its value is unknown and could not be calculated with the used setup. The SP timing resolution for the full readout can be written as:

$$\sigma_t = \sqrt{\sigma_{fit}^2 - \sigma_{laser}^2 - \sigma_{trigger}^2} < 84 \text{ ps}. \tag{4.8}$$

The upper limit is calculated for $\sigma_{trigger} = 0$ ps and $\sigma_{laser} \approx 35$ ps. In a similar way the resolution of the FEE cards can be estimated as:

$$\sigma_{FEE} = \sqrt{\sigma_t^2 - \sigma_{MCP}^2 - 2 \cdot \sigma_{TDC}^2 - \sigma_{sync}^2} < 72 \text{ ps}. \tag{4.9}$$

The timing resolution for the full readout is already below the limit of 100 ps demanded by the PANDA Barrel DIRC. The different timing contributions and resolutions are summarized in Table 4.1.

The presented results were obtained under stable working conditions of the FEE. During a beam experiment, these could change and they might influence the timing performance. Gain variations, ageing, and temperature fluctuations could modify the MCP-PMT response, and, consequently, the time-walk correction function. In particular, a wrong slope parameter m in

Table 4.1: Summary of the timing contributions and resolutions.

Parameter	Description	Value
σ_{MCP}	MCP-PMT intrinsic resolution	39 ps
σ_{TDC}	TDC timing precision	11 ps
σ_{sync}	Synchronization precision between FPGAs	13 ps
σ_{laser}	Laser source uncertainty	35 ps
σ_{FEE}	FEE intrinsic resolution	<72 ps
σ_t	SP timing resolution	<84 ps

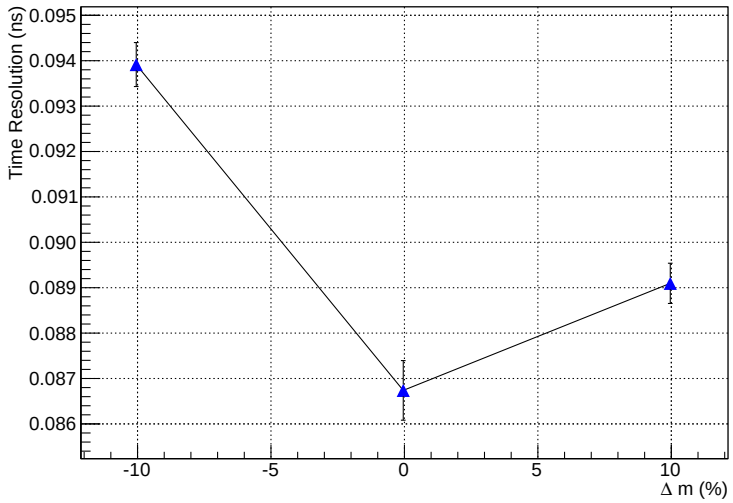

Figure 4.11: Time resolution optimization by varying the slope parameter (m) of equation 4.6.

Eq. 4.6 may substantially decrease the effectiveness of the method.
The timing resolution should have a minimum at the correct parameter m. This behaviour was verified by arbitrary varying the slope m by $\pm 10\%$. The result (see Fig. 4.11) shows a noticeable worsening of the resolution for wrong parameters and, as expected, a minimum at the original value of m.
The search of a minimum in the timing resolution can be used for optimizing the time-walk correction when the correct parameter m is unknown. This is particularly useful when no precise timing references (like the laser trigger) are available to calibrate the time-walk correction. Further results about this technique are presented in Section 5.1.4.

4.2 FEE response to plastic scintillator signals

The characterization of the full FEE chain for plastic scintillators is presented in this section. Compared to SP signals, scintillation signals are larger and slower as shown for MIPs in Section 2.2. In the case of the A1 NDet, neutrons and protons were expected to produce even larger signals. Excessive charge could lead to saturation effects of the NINO ASIC. For this reason, a dedicated test with MIPs was performed. In addition, a timing study was conducted using a radioactive source to investigate the tracking capability.

4.2.1 Characterization with cosmic muons

The readout of plastic scintillators with the FEE and the TRB3 was investigated with the same cosmics setup used for the signal characterization in Section 2.2. In this case the output of the single channel PMT was fed into one channel of the FEE, as shown by the schematic in Fig. 4.12. The FEE

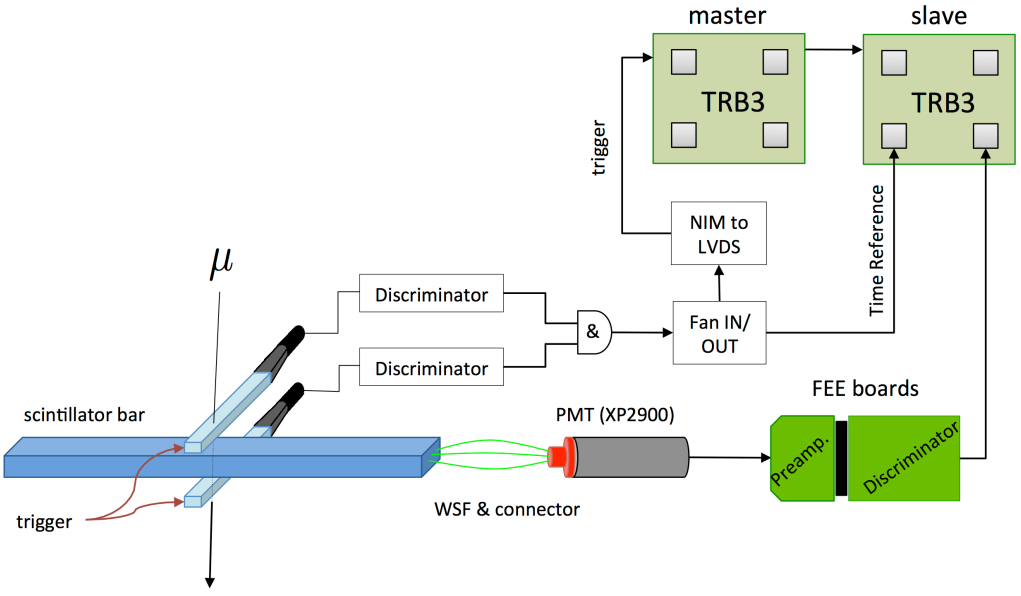

Figure 4.12: Signal characterization using cosmics. A scintillator bar is readout with a single channel PMT and the full electronics chain. Two small scintillator strips provide the trigger.

output was acquired by one FPGA of a slave TRB3 board. The coincidence signal of two small scintillator strips provided the trigger to the TRB3 system, with an average rate of 2-4 events/minute. The data taking required several days to collect sufficient statistics for the analysis.
The time correlation between the reference signal of the trigger (the peak at 0 ns) and the PMT response is shown in Fig. 4.13, in which all the hits of the PMT channel are displayed. As previously found in Section 4.1.1, the timing spectrum allows an easy definition of time window for the analysis. In particular, the time cuts are important when using multi-hit TDCs, like the TRB3, and allow a substantial reduction of the uncorrelated background.

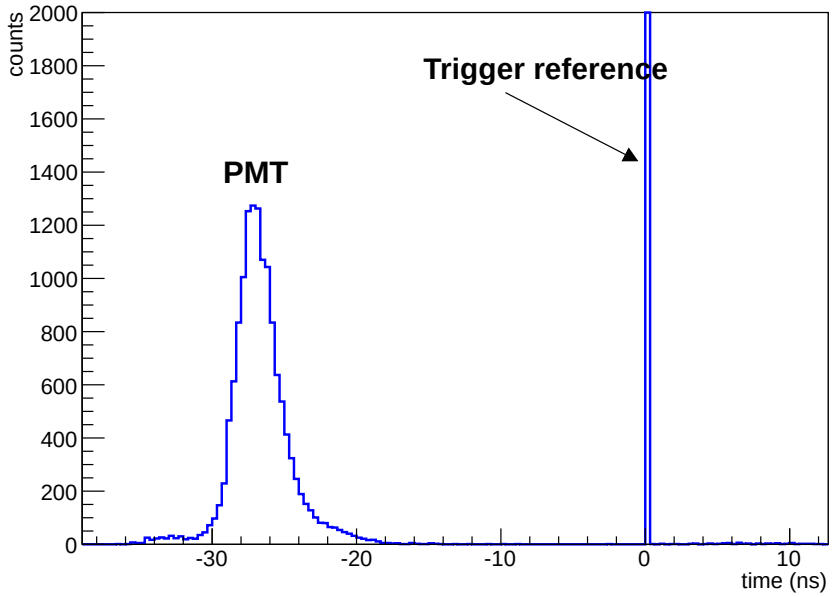

Figure 4.13: Time spectrum of cosmic muons traversing a scintillator bar measured with the full readout chain. The peak at 0 ns belongs to the trigger reference channel.

The response of the FEE was investigated with and without preamplifier Add-on cards to understand if MIP signals exceed the charge limit of the NINO (see Section 3.3) thus causing saturation effects. The ToT spectrum in Fig. 4.14 shows the results for the two configurations. The presence of

the preamplifier shifts the distribution by about 10 ns to higher ToT, as intuitively expected. Qualitatively, the shape of the distributions is similar apart from the peak at around 12 ns. Plotting the arrival time as a function of the ToT (see Fig. 4.15) helps understanding the nature of this peak. The 12 ns component has a time delay from the main structure, due to after-pulses stemming from the discriminator. The same behaviour was observed using a oscilloscope with a pulse generator, indicating a charge saturation effect.

Although, the easiest solution is a direct connection of the PMT to the FEE

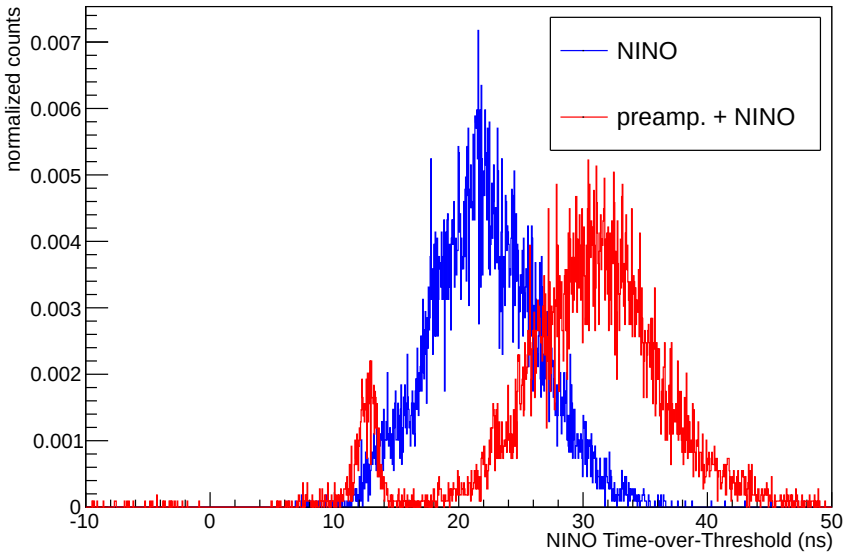

Figure 4.14: Time over threshold spectrum with (red) and without (blue) preamplifier card. After-pulses caused by saturation of the discriminator produce the peak at 12 ns.

without any amplification stage, the same effect could arise in test experiments due to higher energy depositions. The problem was solved by adding an additional resistor at the discriminator input. Of course, a lower gain can help too, with the drawback of a lower sensitivity to small signals.

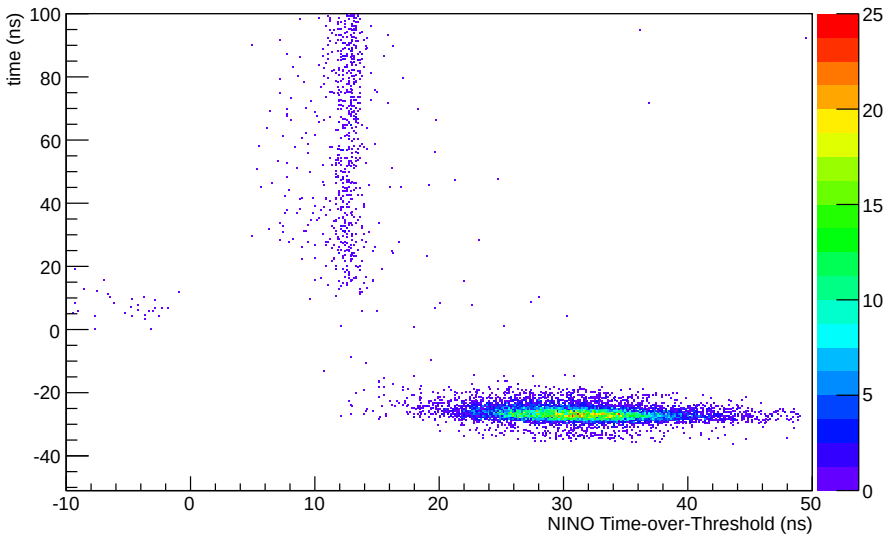

Figure 4.15: Scatter plot of the arrival time of muons as a function of the measured time over threshold. The structure at positive time (>20 ns) is due to charge saturation phenomena of the discriminator.

4.2.2 Characterization with a radioactive source

The study of the timing response requires a high precision on the position of charged particles hitting the bar. The cosmics setup was not suited for this measurement, and simple modifications on the geometry to achieve a higher precision, would have led to even smaller count rates. Conversely, the use of a radioactive source allowed an easy definition of the interaction point, as well as enough statistics in a short period. In particular, a ^{90}Sr source was chosen for the test and placed directly over the bar (see Fig. 4.16). The β decays of the ^{90}Sr releases an end-point energy of 546 keV [53]. Its daughter ^{90}Y follows a β decay with an end-point energy of 2.281 MeV and an average energy for the electron of approximately 1 MeV (considered for this test). The source was enclosed in a lead collimator which provided electrons with a position uncertainty at less than 5 mm. In this case, the bar was readout on both sides to measure the time difference at various positions of the source. The three WLSs (per side) were coupled through a plastic connector to clear fibres. The latter were connected with a dedicated adapter to two 64 channel MAPMTs (see Section 1.3). A previous alignment assured the matching of fibres and

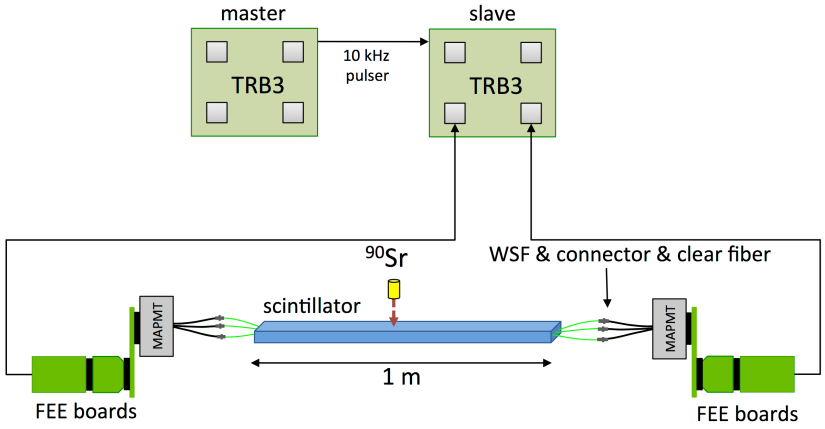

Figure 4.16: Experimental setup with a ^{90}Sr source.

pixels. Each MAPMT was attached to an adapter board and readout by the discriminator cards, using a total of 8 FEE cards and one TRB3. The master TRB3 board controlled the data acquisition using the internal pulser, which was set to a high clock rate (50 kHz) to avoid multiple hits. The result in

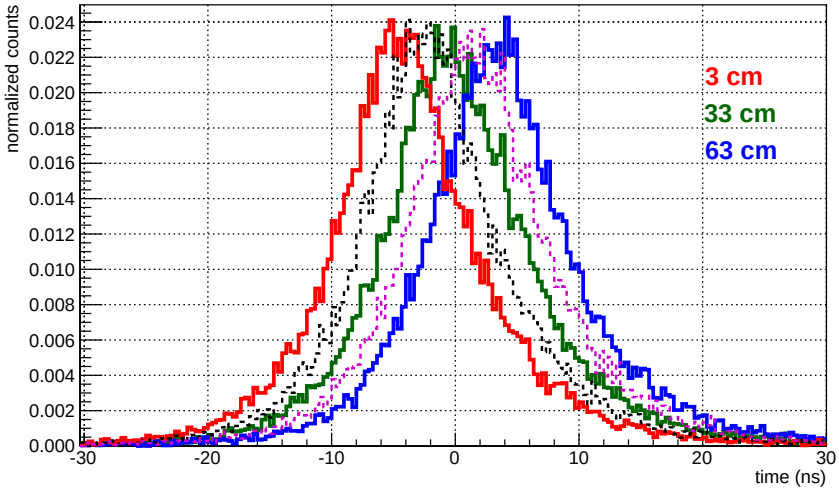

Figure 4.17: Left-right timing differences at different positions of the radioactive source. The dashed lines belong to intermediate positions (18 cm in black and 48 cm in purple).

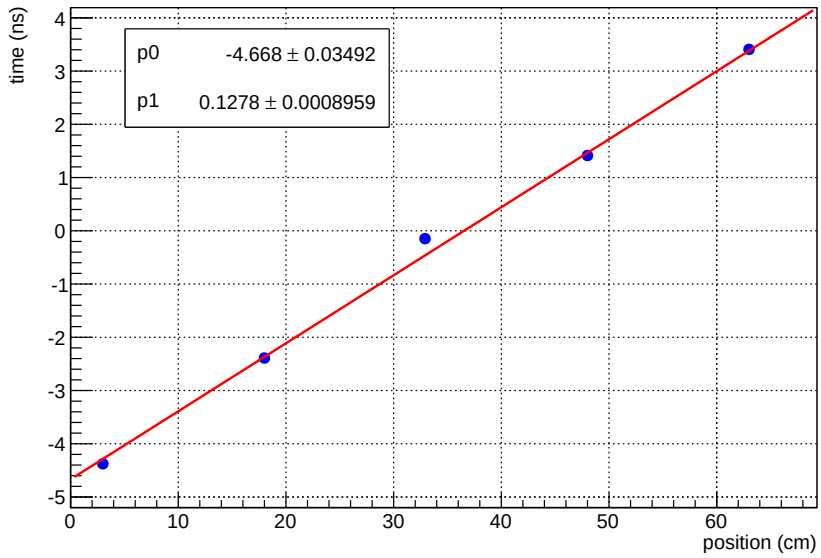

Figure 4.18: Correlation between time difference and position of the strontium source along the bar. A linear distribution is used for the fit.

Fig. 4.17 shows the measured time differences of the two MAPMTs at different positions of the ^{90}Sr source along the bar. Even if the position of the source was well defined, the data show a poor timing resolution between 5 and 6 ns, which does not depend on the position. The resolution is qualitatively comparable with the length of the bar, and is caused by a poor photon yield. Further studies revealed imperfections of the scintillator surface which affected the timing performance of the NDet. Nevertheless, the average time for every source position allowed to measure the correlation between the two quantities. As expected for plastic scintillators, the result in Fig. 4.18 shows a linear behaviour, with a time constant of approximately 128 ps/cm.

Chapter 5

Experiments with Prototypes at MAMI

The performance of the full electronics chain comprising photodetectors, FEE and TRB3 was extensively analyzed during several test experiments at the MAMI accelerator in Mainz.
The stable and controlled properties of its electron beam were used for a complete characterization of a small scale prototype of the PANDA Barrel DIRC. The setup was tuned to SP detection for detailed studies of the timing performance.
The three spectrometer setup of the A1 Collaboration allowed a detailed test of the NDet prototype. The plastic scintillator array was studied in a coincidence experiment allowing an almost background-free investigation. The PID performance using ToT and the rate capability of the FEE were investigated in depth.
The experimental areas, the setups and the results of the different experiments are described in this chapter.

5.1 Beam test with an Imaging Cherenkov Counter

The study of FEE for imaging Cherenkov counters requires particular attention due to their complexity. A small scale DIRC prototype was used to produce correlated Cherenkov photons like in the final detector (see Section 5.1.1). Stable and well known beam conditions are an asset for sys-

tematic studies of FEE. This is particularly important for complex DIRC detectors, where many parameters have to be tuned (e.g. beam dimension, impact point and incidence angle). While mixed hadron beams are optimal for the study of its PID performance, electron beams are well suited for electronics characterization. Indeed, mono-energetic and well focussed electrons produce a clear Cherenkov pattern without ambiguities. The characteristics of the MAMI accelerator provided a unique environment for these investigations. In particular the X1 experiment beam line was chosen for the test experiment of the DIRC prototype (see Fig. 5.1). In the this area, the continuous wave beam of electrons, delivered by MAMI, offers an energy of up to 855 MeV, a spot diameter of 1 mm and negligible divergence [10, 74]. An

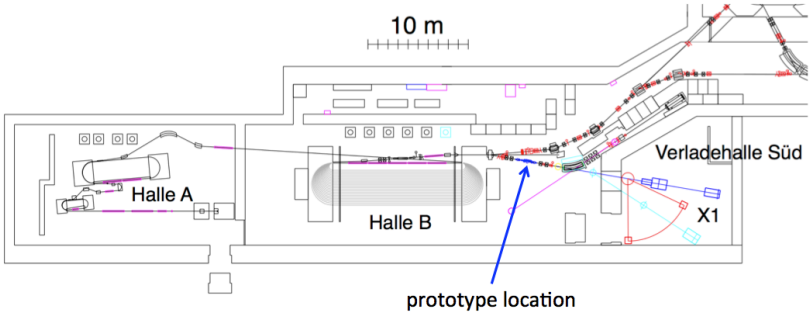

Figure 5.1: MAMI-B accelerator floor plan [75]. The arrow indicates the test area of the DIRC prototype.

aluminium plate approximately 2 m long and 2 m wide, was installed below the beam pipe to support the prototype. A pivot was placed on the beam axis to be able to rotate the prototype. During the experiments the path length of the beam in air was less than 0.5 m before hitting the prototype.
Two plastic scintillator strips were used to monitor the beam conditions. They were placed downstream, in order to reduce the material budget before prototypes. The size of the two strips excluded events with large scattering angles. The strips were instrumented with PMT and standard NIM electronics to measure their signals.
The coincidence rate of the strips was logged throughout the experiment. The result for a period of 11 hours (see Fig. 5.2) shows a very good stability, where the small fluctuations were caused by optimizations or maintenance of the accelerator and changes of the prototype setup.

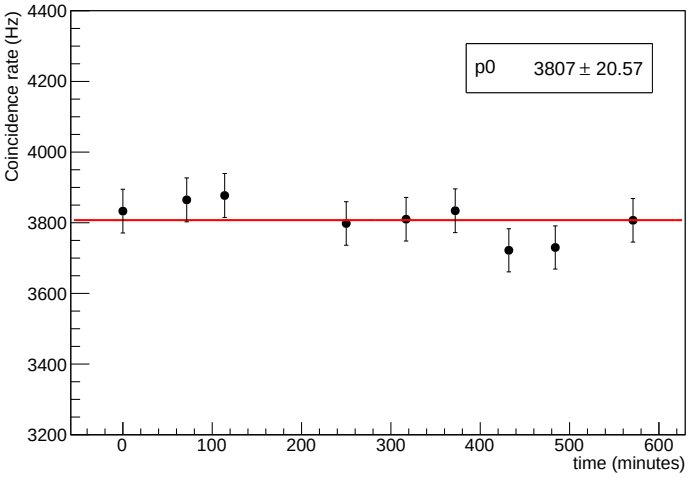

Figure 5.2: Coincidence rate of trigger scintillators over an 11 hour period.

5.1.1 The Imaging Counter Prototype

A small scale DIRC prototype (see Fig. 5.3) was built to study the full electronics chain comprising MCP-PMTs, FEE and TRB3. A synthetic fused silica bar[1] ($33 \times 17 \times 830$ mm^3, with $n \approx 1.47$ at $\lambda \approx 400$ nm [76]) was used as radiator and light guide as described in Section 1.2. The bar was mounted on a movable support structure made from aluminium with two holders made from plastic to prevent damage of the surfaces; the holders were symmetrically placed on the Airy points (175.4 mm from the edges) to minimize distortions caused by gravitational sag.

One of the two edges of the bar was optically coupled to a planoconvex lens (focal length $f = 250$ mm), followed by a variable air-gap. A glass tank ($800 \times 600 \times 300$ mm^3) filled with mineral oil[2] ($n \approx 1.47$) was used as stand-off volume. Two adjustable and movable towers were placed on the opposite side of the stand-off volume to mount four MCP-PMTs[3] at specific positions. The air-gap was adjusted in order to focus the Cherenkov light onto the photodetector plane. For some tests a mirror was placed on the opposite end of the radiator bar to detect backward going photons with longer path lengths.

[1] Heraeus Quartzglass, Carl Zeiss SMT AG
[2] Marcol82
[3] Burle XP85012, see Section 2.1.1

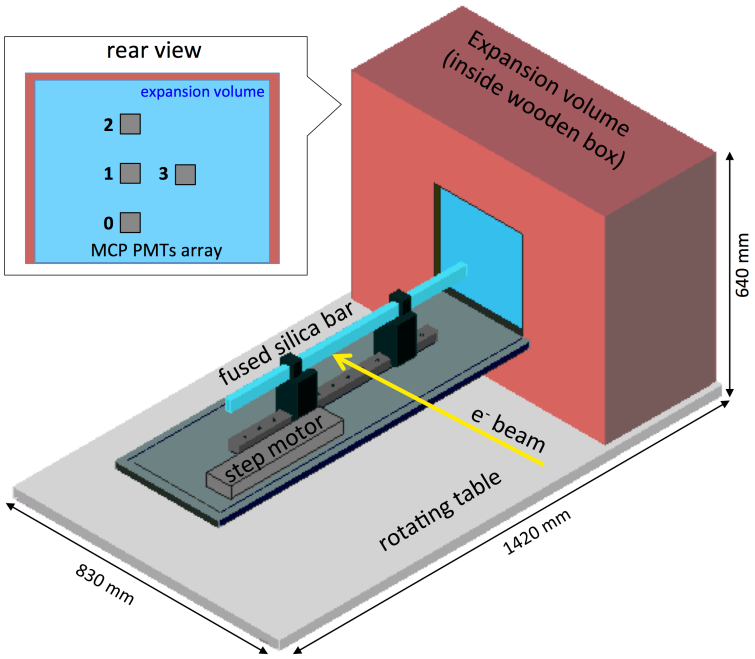

Figure 5.3: Schematic view of the DIRC prototype setup and rear view of the expansion volume.

The whole prototype was shielded from ambient light. An aluminium table supported the prototype, and allowed easy horizontal rotations around the pivot.
A total of 16 FEE cards was connected through custom-made feed through panels to the TRB3 setup. The operating voltage of the MCP-PMTs was tuned to a gain $G \approx 10^6$, the corresponding values are given in Table 5.1 (a). Two different series of MCP-PMTs (a low and a high gain series) cause the HV differences. The DAQ was set up with three TRB3 (one master + two slave boards), for a total of 256 readout channels (512 TDC channels). The mapping of photodetector to TRB3 channels was chosen to optimize the synchronization precision between the central MCP-PMTs (1 and 3 in Fig. 5.3). Two flat ribbon cables, *a* and *b*, connecting the FEE mother board to the FPGAs were connected according to Table 5.1 (b). The FPGA numbering follows the convention described in Section 3.1.1 (see Fig. 3.4).
The trigger was realized with the two plastic scintillator strips which were used to monitor the beam. The coincidence signal was translated to LVDS and used as external trigger for the TRB3. More details about the prototype

setup can be found in [51, 77].

Table 5.1: (a) MCP-PMT high voltages for a gain $G \approx 10^6$. The FPGA numbering follows the scheme on Fig. 5.3. (b) MCP-PMT to TRB3 channel mapping.

MCP-PMT	High Voltage (V)
0	-2150
1	-2082
2	-1610
3	-1970

(a)

MCP	FPGA a	FPGA b
0	2^{TRB1}	3^{TRB1}
1	1^{TRB1}	4^{TRB1}
2	2^{TRB2}	3^{TRB2}
3	1^{TRB2}	4^{TRB2}

(b)

5.1.2 General results

The beam test delivered a wealth of information for the study of the full readout chain. The TRB3 DAQ exhibited a high efficiency and stability. No crashes happened during the whole experiment (around 150 hours). Less than one in a million events was lost, only caused by errors in the digitization (random bit error) [57] (see Fig. 5.4). On average only 1% of the hits per event were incomplete (only leading or trailing edge information registered).

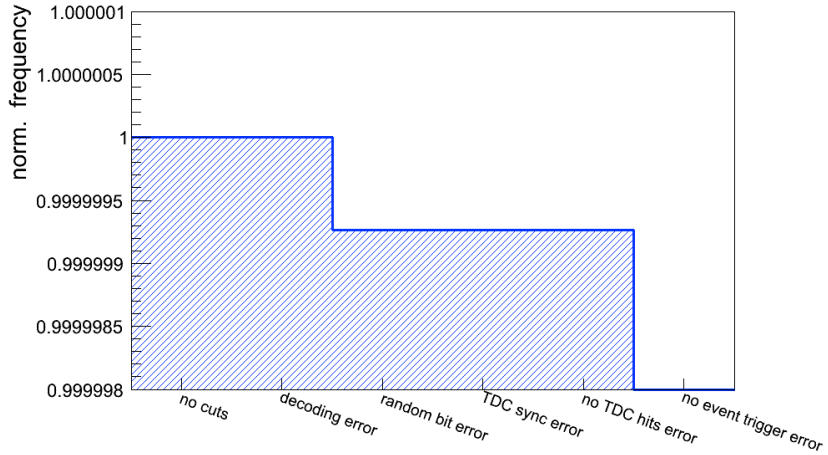

Figure 5.4: Normalized frequency of TRB3 error conditions.

The low noise background conditions did not require any time windows by the TRB3 DAQ. Nevertheless, in the analysis a time window was required to select only the relevant hits. A typical time spectrum for about 2.5×10^6 events and all TDC channels is shown in Fig. 5.5. The signal coming from the MCP-PMTs and the plastic scintillator coincidence, indicated in the figure, are well above the noise background, allowing an easy definition of the time window (set to [-400,-50] ns). The broad structure at around 0 ns is noise caused by the TRB3 interrupt.

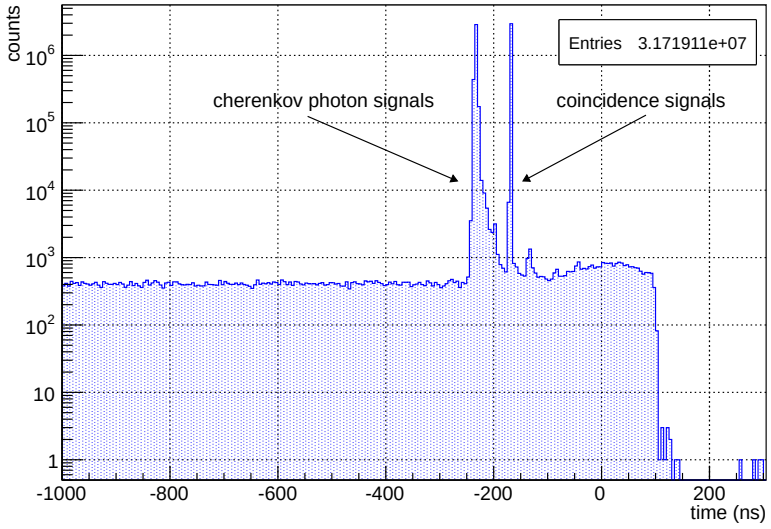

Figure 5.5: Time spectrum for about 2.5×10^6 events using all the 512 TDC channels.

A scan of the individual thresholds was performed on a random channel to verify the behaviour found in Section 4.1.1. Four different threshold levels were used to extract the average peak position of the ToT spectra. The result in Fig. 5.6 shows a trend qualitatively similar to the data obtained with the laser calibration. Therefore, the threshold level was set to 1.3 V as previously established.
During the beam test negligible threshold shifts were observed over an extended period of data taking (see Fig. 5.7), proving a good implementation of the PCB board. On average the power consumption of the FEE including

preamplifier Add-on cards was about 160 mW/channel.

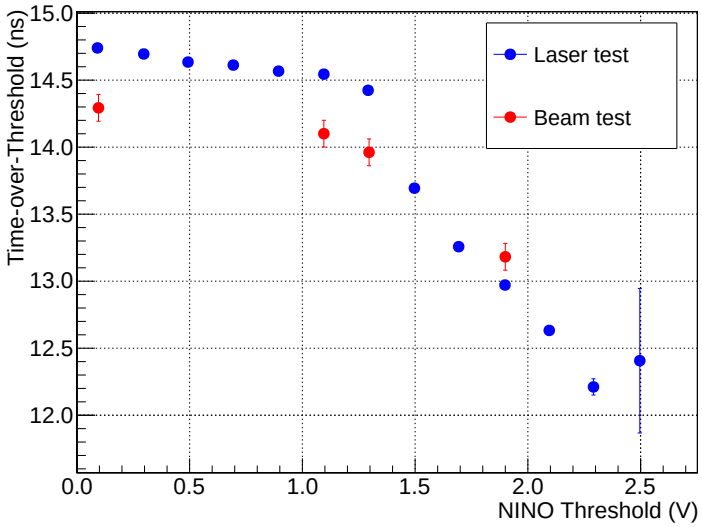

Figure 5.6: ToT response to MCP-PMT signals as a function of the threshold.

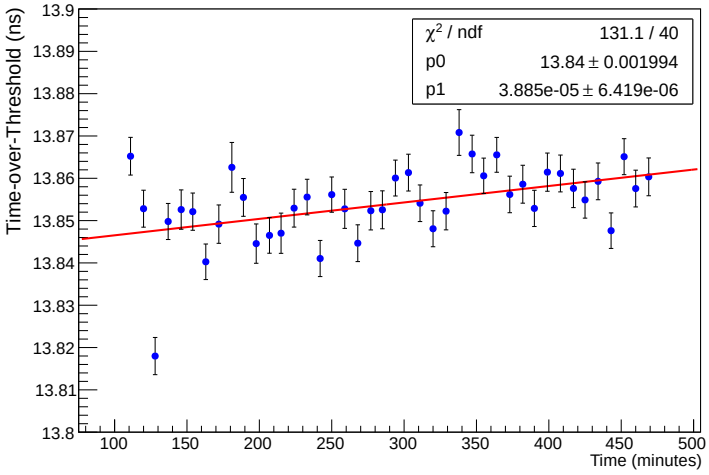

Figure 5.7: Measured ToT over an extended period of data taking. The trend shows a good overall stability.

5.1.3 Imaging capabilities

The detection of Cherenkov patterns is one of the key requirements for DIRC detectors. Even if the prototype was not optimized for imaging, this was fundamental for successive timing investigations.
During the beam test the air-gap between the bar and the stand-off volume was set to 5.7 cm. This value was calculated with simple optical formulae in order to focus the Cherenkov photons onto the detector array (more details can be found in [51]).
A Monte Carlo simulation based on ray tracing [77, 78] was employed to set a proper position for the MCP-PMT array. All the imaging data analysis was performed with a specific framework developed with ROOT/C++ [79]. Results for three different incidence angles (57°, 60° and 90°) are shown in Fig. 5.8, where each intensity plot on the left is an overlay of two million events. The corresponding simulations are shown on the right and qualitatively agree with the data. For example, as expected, at 90° no Cherenkov photons were detected. At 57° and 60°, the image moves accordingly. A detailed view of data and simulations together is shown in Fig. 5.9 for the 57° measurement. The holes in the pattern (especially on the central FPGAs) may be due to imperfections of the optical connection of MCP-PMTs and stand-off volume.
Large gaps between the MCP-PMTs are the reason for a low detection efficiency. The gaps were needed to observe the arcing pattern using the available number of photodetectors. As the next section shows, a low light yield has clear advantages for studying the FEE response. The number of hit pixels per event, which can be considered in first approximation as the number of detected photons, was measured at 57°, 60° and 90°, see Fig. 5.10. As expected from the imaging, there are mainly no hits per event at 90°. The difference between 57° and 60° comes mainly from the MCP-PMTs number 0 and 2. The average number of detected photons is summarized in Table 5.2.

Table 5.2: Average number of detected photons at different angles.

Angle (°)	Detected photons
90	0.2
60	2.1
57	3.3

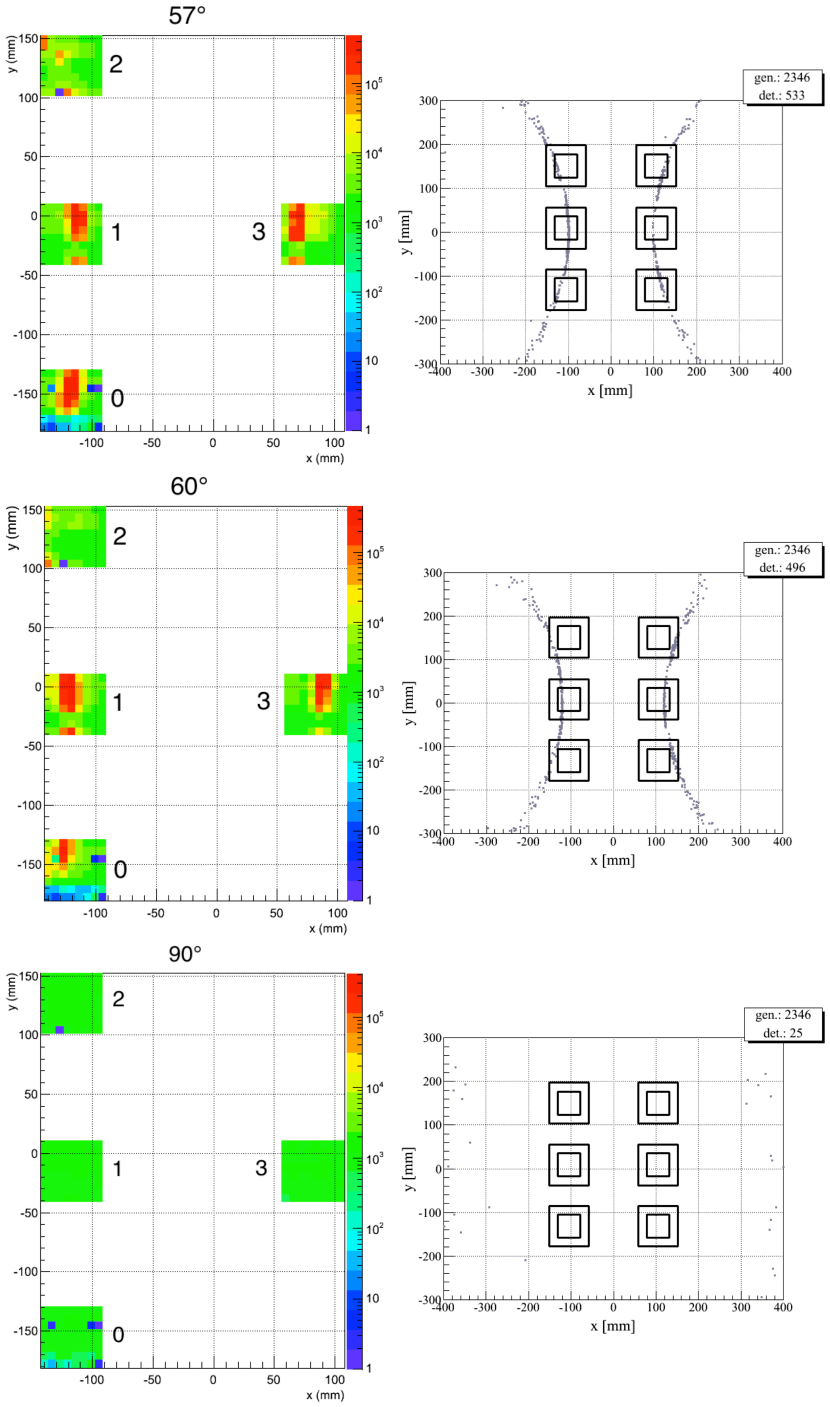

Figure 5.8: Observed Cherenkov pattern at different incidence angles and corresponding simulations. The plots on the left are an overlay of two million events. The six boxes on the simulations indicate the possible positions of the MCP-PMTs on the expansion volume.

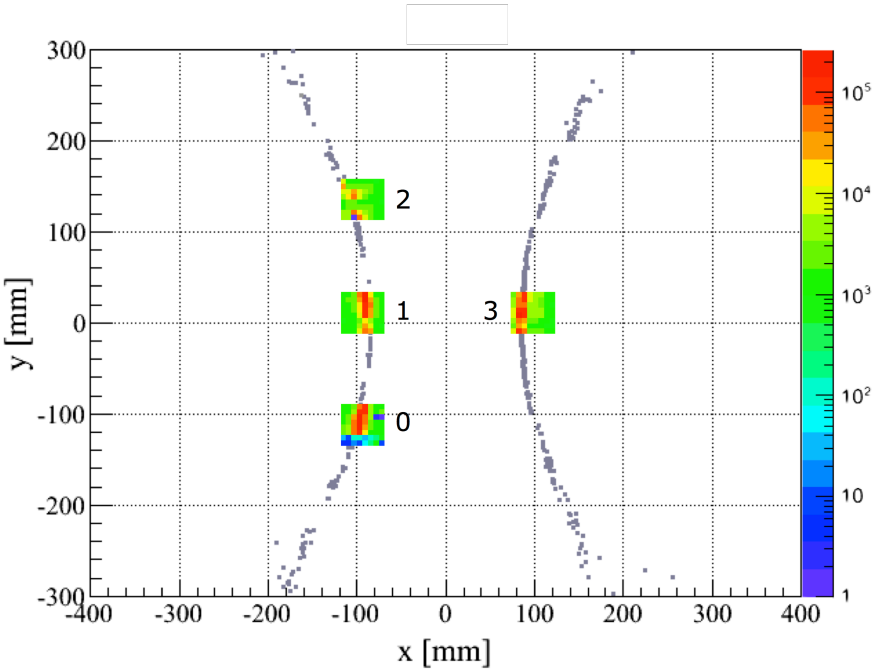

Figure 5.9: Observed Cherenkov pattern at 57°. Monte Carlo simulation is shown in grey.

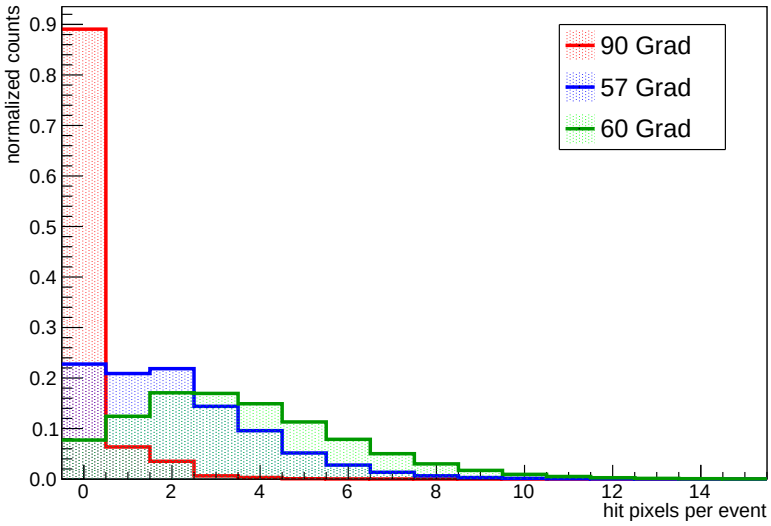

Figure 5.10: Number of hit pixels at different incidence angles.

A mirror attached to the open end of the radiator bar allowed the study of larger incidence angles ($> 90°$). The prototype was rotated to 120°, so that backward going photons were reflected and transported to the stand-off volume with a path similar to the 60° case. The result in Fig. 5.11 (a) qualitatively agrees with the expectation, but shows a larger width (three-four red columns instead of two) probably caused by imperfections on the optical path through the mirror or by the larger number of reflections inside the bar. The different path length between 60° and 120° can be calculated

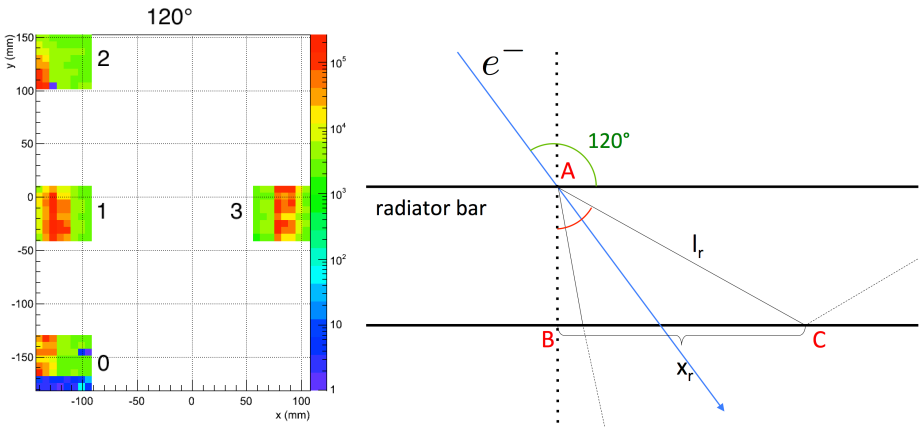

(a) (b)

Figure 5.11: (a) event display at 120°. (b) schematic view of the radiator bar and the Cherenkov light path.

with the additional number of reflections. Assuming the impact point of the beam is centred on the bar, an additional length $\Delta X = 830$ mm has to be considered. The effective path length of the light inside the bar can be calculated with the help of the scheme in Fig. 5.11 (b). It can be shown that the angle $\widehat{BAC} = 120° - \theta_c = 120° - 47.14° = 77.14°$, and $x_r = 74.46$ mm. The path length for each reflection is $l_r = 76.38$ mm, while the total number of reflections is:

$$N_{reflections} = \frac{\Delta X}{x_r} = 11.14 \tag{5.1}$$

The real path length ΔL and its propagation time Δt are defined as:

$$\Delta L = N_{reflections} \cdot l_r; \;\; \Delta t = \frac{\Delta L}{c/1.47} \approx 4.2 \text{ ns}. \tag{5.2}$$

The arrival time was measured choosing a pixel with high statistics in the central MCP-PMTs. In this way, photons propagating in the plane of the beam, where the approximation is valid, are selected. Fig. 5.12 shows the time spectra at 60° and 120°. The data are fitted on the peak region with a Gaussian function, and the mean values are $t_{60°} = -106.1 \pm 1.4$ ns and $t_{120°} = -101.7 \pm 1.4$ ns. The measured time difference is:

$$\Delta t_{measured} = t_{120°} - t_{60°} = 4.4 \pm 2.0 \text{ ns}, \tag{5.3}$$

where the scintillators used as timing reference cause the poor time resolution. The result agrees well with the expectations and not only it shows that the system is well understood but it also demonstrates that backward and forward going photons are distinguishable, using the timing information. Further details, like multiplicity studies with and without the mirror can be found in [51].

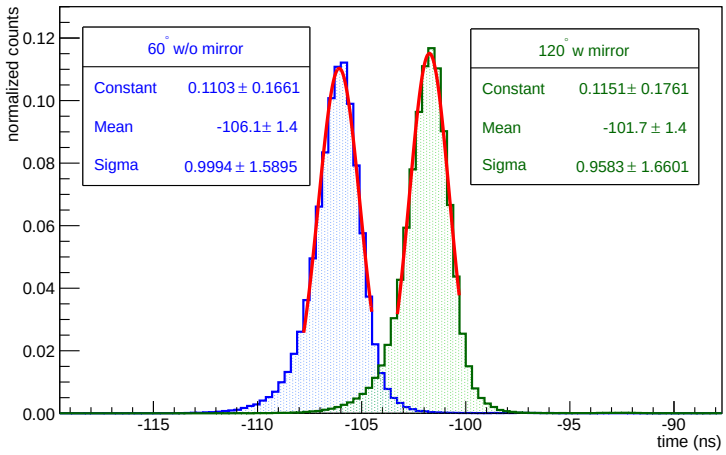

Figure 5.12: Photon arrival time for one MCP-PMT channel at prototype angle of 60° and 120°.

5.1.4 FEE Timing Resolution

The FEE contribution σ_{FEE} to the SP timing resolution can be described as the quadratic sum of several components:

$$\sigma^2_{FEE} = \sigma^2_{NINO} + \sigma^2_{preamplifier} + \sigma^2_{TRB3}, \tag{5.4}$$

where $\sigma_{preamplifier}$, σ_{NINO} and σ_{TRB3} are the preamplifier, the discriminator and the DAQ components respectively.
The charge sharing of SP between neighbouring pixels of an MCP-PMTs can be easily used to measure σ_{FEE}. The anode structure of MCP-PMTs allows the sharing of the electron cascade between pixels. The effect becomes relevant when the photon hits the photocathode around the "imaginary" boundary between two pixels. When this happens, the transition time spread is the same for the considered pixels. Thus, in first approximation, their time difference is affected only by the electronics. The low number of detected photons per event, reported in Table 5.2, guarantees the identification of charge sharing as SP events, because the probability of having two photons hitting the same pixel is negligible. Two neighbouring channels inside the Cherenkov pattern in MCP-PMT 1 were chosen for this analysis. The pixels were readout by different FEE to avoid electronic crosstalk. The ToT of the two pixels is plotted in Fig. 5.13 and shows a correlation caused by the charge sharing. The spectrum of the time differences is shown in Fig. 5.14, before and after a

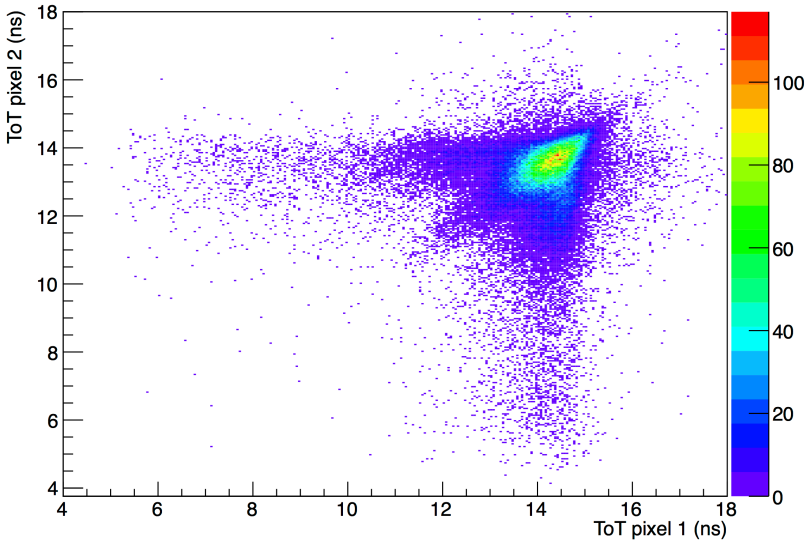

Figure 5.13: Scatter plot of the ToT for two neighbouring pixels.

time walk correction. Both histograms are fit with a sum of two Gaussians, taking into account the presence of uncorrelated events or an imperfect walk correction. The timing resolution σ_{FEE} is taken as the standard deviation of

the narrow peak. The walk correction improves σ_{FEE} by about 70%, with an excellent value of $\sigma_{FEE} \approx 53$ ps.

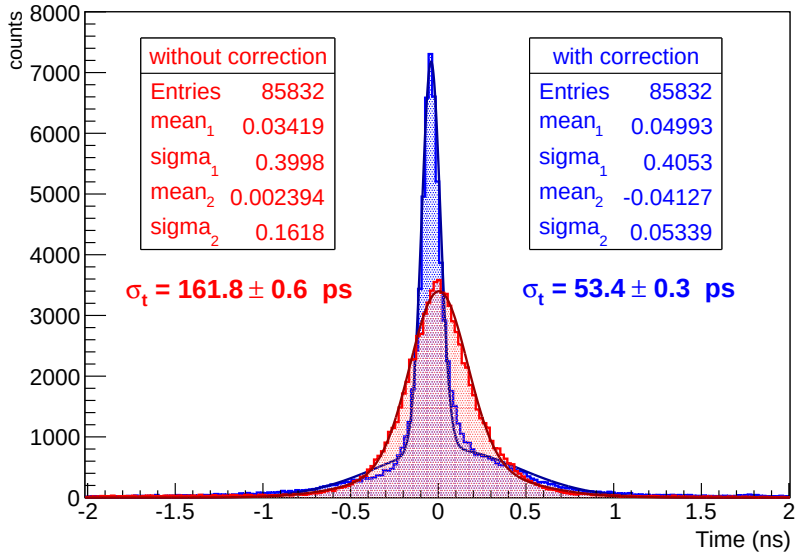

Figure 5.14: Measured timing resolution σ_t between neighbouring MCP-PMT pixels: uncorrected data (red), corrected data (blue).

The different running conditions (e.g. temperature and gain), between the laser characterization and the test experiment, require an optimization for the coefficients of $t_{cor}(ToT)$ in Eq. 4.6. Ideally, a fast laser pulse homogeneously distributed over the focal plane could help to calibrate the coefficient, but this feature was not implemented in the setup. Nevertheless, the technique proposed in 4.1.2 can be used as well. Starting from the slope m, its value was arbitrarily varied looking for a minimum of the corrected timing resolution σ_{FEE}. Fig. 5.15 shows a minimum of σ_{FEE} at 30% steeper slope from the original m value for two distinct pixels in two different MCP-PMTs. This simple algorithm further improves the timing resolution to $\sigma_{FEE} \approx 40$ ps on average.
The timing performance of the FEE was monitored over an extended period of time in order to study possible fluctuations. In particular, σ_{FEE} (without optimization) was chosen as observable. The results for a period of eight hour demonstrated a stable behaviour, as shown in Fig. 5.16.

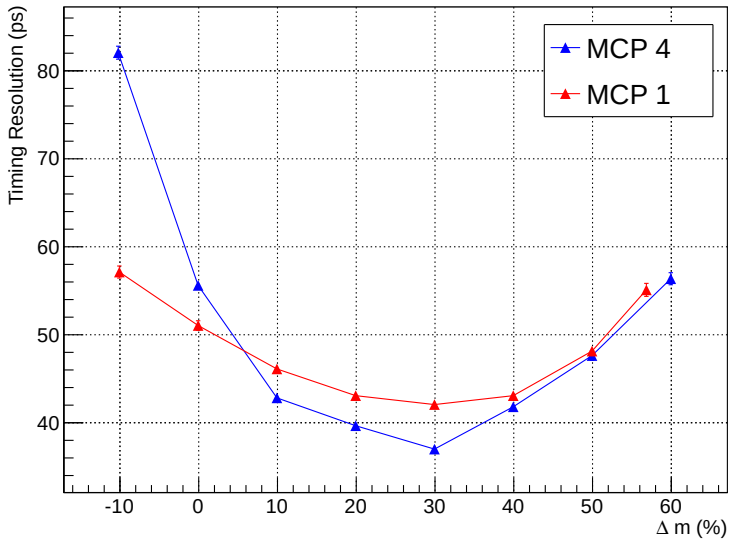

Figure 5.15: Optimization for the slope parameter of the time walk correction. The red and blue dots show the result for two different pixels in two MCP-PMTs.

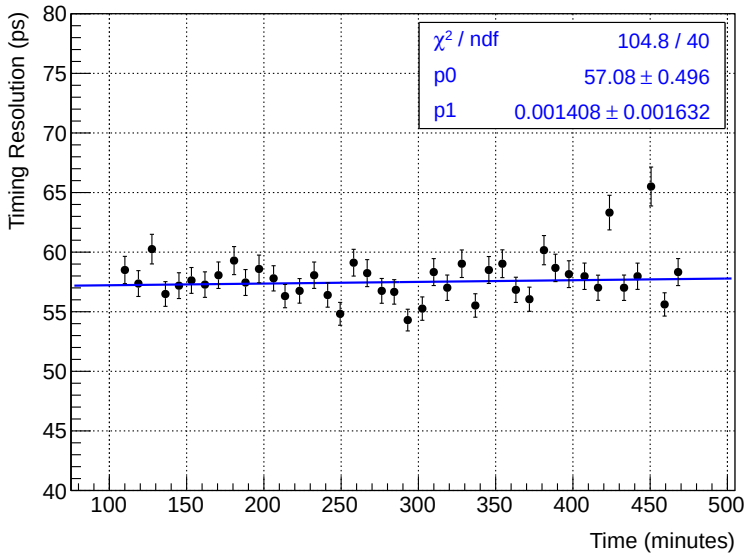

Figure 5.16: Measured σ_{FEE} over a extended period of data taking.

The sensitivity of the FEE was studied with different MCP-PMT gains as well. Fig. 5.17 shows the average ToT for SP events at different gain levels and, as expected, a direct proportionality is observed. The timing resolution, as shown in Table 5.3, gets worse at lower MCP-PMT gain.
The lifetime of MCP-PMTs depends on the integrated anode charge, thus on the used gain [49]. A new version of the XP85112 ensures high timing performance and extended lifetime at a gain of 1×10^6 [80]. The substantial difference between the old series of MCP-PMT (used in this thesis) and the new is shown in Fig. 5.18. The quantum efficiency remains stable up to almost 6 C/cm^2, which corresponds for the Barrel DIRC to 12 years of operation at a MCP-PMT gain of 1×10^6.
Nevertheless, running at lower gain will increase the lifetime of MCP-PMTs [49]. This could particularly useful in case of rates higher than the expected ones. Recent studies for the TOP of Belle II show that high timing resolution can be achieved at intermediate gain levels ($\sim 5 \times 10^5$) [81]. Similar results are expected in this case. Indeed, the charge Q at the discriminator input (see Table 5.3) for a gain of 5×10^5 is well above the range where high jitter compromises the NINO performance ($\sigma_{jitter} >> 20$ ps for $Q < 200$ fC) [63]. Conversely, the input charge at a gain of 1×10^5 is too low. Preamplifier Add-on cards with higher gain ($g > 13$) could be used to overcome the limit.

Table 5.3: Timing resolution σ_{FEE} and expected input charge for the discriminator card at different MCP-PMT gains.

Gain	σ_{FEE} (not corrected)	Q
1×10^5	190 ps	83 fC
5×10^5	175 ps	416 fC
1×10^6	161 ps	832 fC

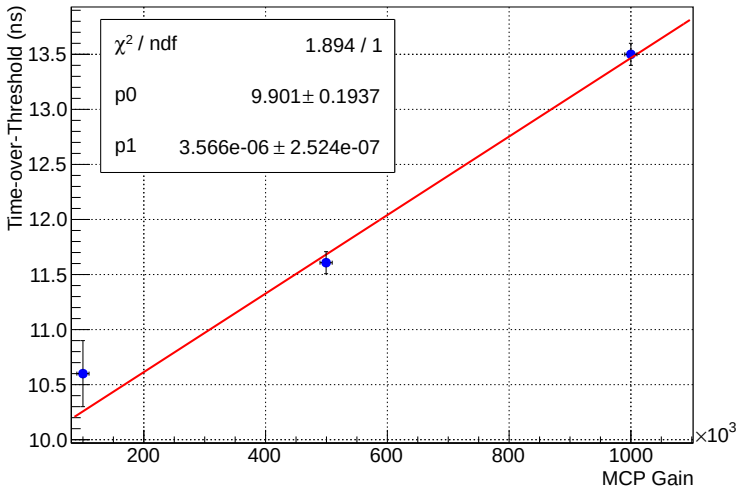

Figure 5.17: Average ToT for FEE events at different MCP-PMT gains. The threshold value was set to 1.3 V.

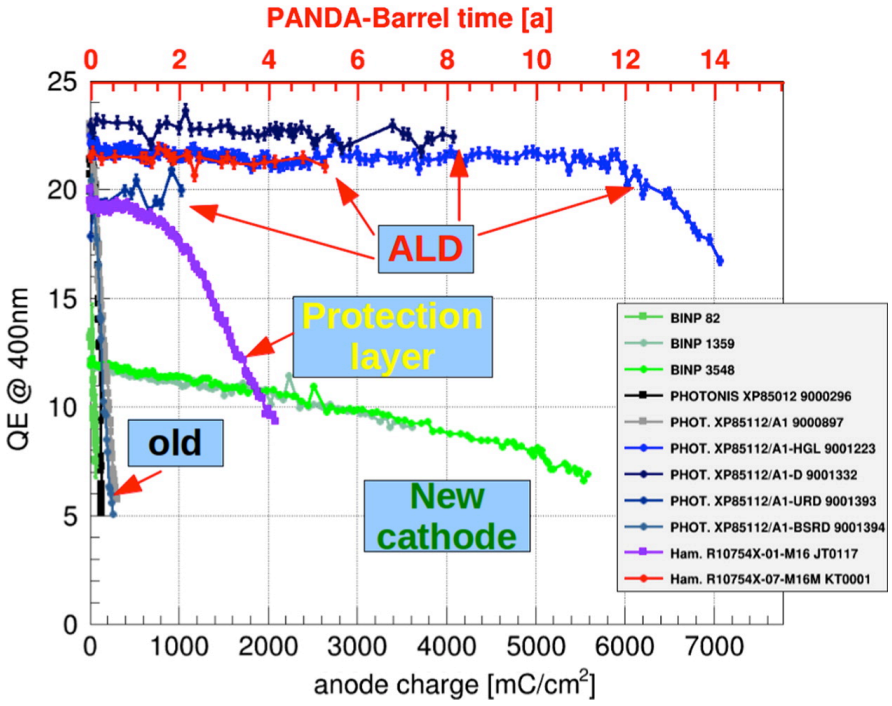

Figure 5.18: Comparison of the lifetime for different MCP-PMTs (XP85112 with ALD coating in blue) [80]

5.1.5 DIRC Timing Resolution

The timing resolution of the prototype $\sigma_{prototype}$ was measured considering the time differences of pixels from different MCP-PMTs in the horizontal plane ($y \approx 0$). This allows the selection of photons with a symmetric path from the radiator to the focal plane. The results in Fig. 5.19 are obtained with the

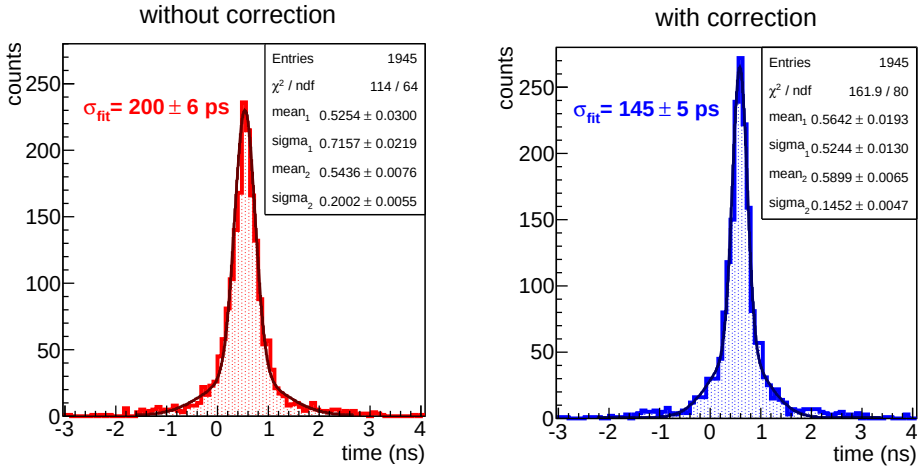

Figure 5.19: Measured timing resolution σ_t between different MCP-PMTs: uncorrected data (red), corrected data (blue).

same fitting technique exploited for σ_{FEE}. In this case the timing resolution corresponds to $\sigma_{prototype} = \sigma_t/\sqrt{2}$. The walk correction reduces the value of $\sigma_{prototype}$ from about 141 ps down to 103 ps improving the performance by about 25%.
The Monte Carlo simulation used for the Cherenkov pattern estimates the timing contribution of the imaging optics to $\sigma^{sim}_{propagation} \approx 63$ ps (see Fig. 5.20). The measured resolution $\sigma^{meas}_{propagation}$ can be obtained in first approximation by:

$$\sigma^{meas}_{propagation} = \sqrt{\sigma^2_{prototype} - \sigma^2_{FEE} - \sigma^2_{MCP-PMT}} \approx 87 \text{ ps} \tag{5.5}$$

where $\sigma_{prototype} \approx 103$ ps, $\sigma_{FEE} \approx 40$ ps and $\sigma_{MCP-PMT} \approx 37$ ps [49]. The difference between simulation and measurement is mainly due to a synchronization jitter between the FPGAs of different TRB3 boards, and can be

estimated as

$$\sqrt{\left(\sigma^{meas}_{propagation}\right)^2 - \left(\sigma^{sim}_{propagation}\right)^2} \approx 60 \text{ ps}. \tag{5.6}$$

Considering the $\sqrt{2}$ factor used to determine $\sigma_{prototype}$, the result is in good agreement with the laboratory tests (see Section 3.1.1). A summary of the measured timing resolutions can be found in Table 5.4.

Table 5.4: Summary of the measured timing resolutions.

Timing resolution	not corrected (ps)	corrected (ps)
intrinsic σ_{FEE}	161.8 ± 0.6	40 ± 1
SP (laser studies)	130.0 ± 0.9	84 ± 0.5
DIRC prototype	141 ± 4	103 ± 4

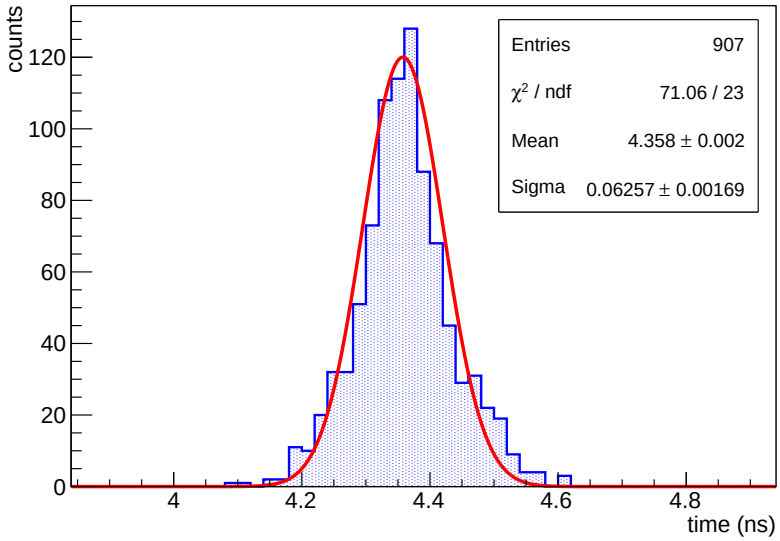

Figure 5.20: Single pixel time spectrum generated by a ray-tracing Monte Carlo simulation. A Gaussian fit is applied to the data.

The obtained results of the FEE are excellent. The high flexibility and the modular design of the cards do not impair the required high performance. The simple operation of the full readout chain adequately suits a complex detector like the PANDA Barrel DIRC. This is also confirmed by the imaging studies and the excellent behaviour of the system. In particular, the FEE allows an easy calibration of the individual thresholds, which show a good stability over an extended period of time.
In the presented studies, a threshold calibration channel by channel was not necessary but this FEE feature will be important in the final detector. For example, the gain difference between the MCP-PMT pixels [49] could be taken into account to obtain a homogeneous response.
The intrinsic resolution of the electronics is significantly high. To achieve this, the time-walk correction based on ToT plays a key role, but its effectiveness strongly depends on the used parameters. In the final detector every channel (almost 15,000 in total) will require a fine tuning of the correction function in order to maximize the timing resolution. As shown, this can be done using a simple optimization method without the need of additional pulsed laser sources for the calibration.
The achieved timing resolution of the prototype meets the requirement of the Barrel DIRC. The excellent value of $\sigma_t = 103 \pm 4$ ps enables the use of chromatic corrections (see Section 1.2), thus increasing the angular resolution for SP events. The measured resolution outclasses the results obtained by the FDIRC prototype which reports several hundreds ps [21]. The results are comparable with the evaluated resolution of the TOP prototype for Belle II [82]. This is particularly significant because the TOP uses waveform sampling chips (see Section 1.4).
The main contribution to the timing resolution is the synchronization jitter between different TRB3 boards. In the final detector, modified TRB3 boards will reduce this jitter from $\sim$ 90 ps to almost $\sim$ 30 ps (see Section 3.1.1), thus further improving the timing resolution to $\sigma_t \sim 80$ ps.

5.2 Beam test with a Scintillator Array

The results of the previous section clearly show that the FEE meets the requirements of DIRC detectors. The performance must be verified for scintillator arrays as well.
A major challenge was set by the dynamic range of the electronics, which was initially tuned for SP events and it was tested only with the relatively small signals of MIPs (see Section 4.2.1). Therefore, a test with larger signals (e.g. neutrons) was needed to prove the real flexibility of the FEE. Another open question was wether the deposited charge measurement with ToT could provide PID information. For these reasons, a beam test using an NDet prototype was performed at MAMI.
A high rate of several MHz per channel is certainly among the strongest requirements of the NDet (see Table 1.2). This was investigated in depth using high beam currents. The performed studies are shown in the following sections.

5.2.1 The NDet prototype

The response of the FEE to scintillator signals was investigated with the NDet prototype. The 3-spectrometer setup of the A1 Collaboration [26] allowed the possibility of coincidence measurements in pion electroproduction

$$e^- + p \rightarrow e^{-'} + n + \pi^+$$

between the π^+ (measured by Spectrometer B) and the neutron hitting the detector. The electron $e^{-'}$ was scattered in the beam dump for the considered kinematics.

The NDet was composed of a metal frame which held two layers of plastic scintillator bars (64 bars per layer), placed atop each other and parallelly aligned, as schematically illustrated in Fig. 5.21. The prototype had an active volume of about $1 \times 1 \times 0.06\ m^3$ (length, width, height). As explained in Section 1.3, each bar is read out by three WLSs which are connected via commercial optical connectors to three clear fibers (on both sides). The clear fibers are then connected with an adapter mask to the 64 channel MAPMTs. The bar-pixel mapping avoided neighbouring bars being readout by neighbouring pixels, in order to disentangle possible crosstalk. The prototype was instrumented with a total of four MAPMTs (two per layer), set to an operating voltage of 800 V (corresponding to $\sim 10^6$ gain). A black plastic wrapping

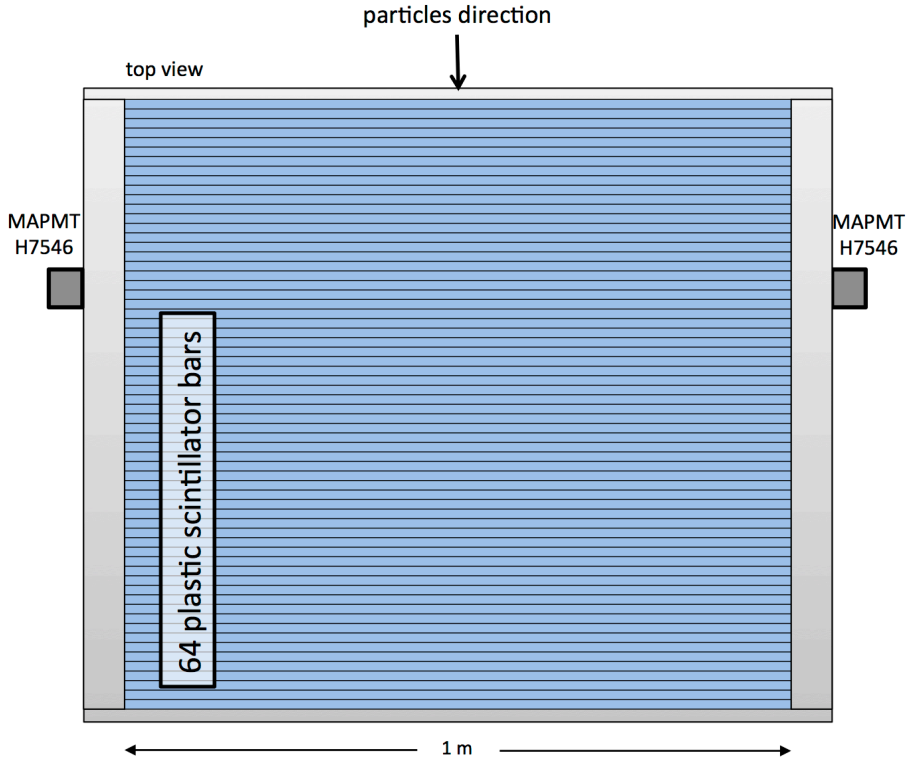

Figure 5.21: Top view of one layer of the neutron detector prototype. 64 scintillator bars with three WLSs each are readout with two 64 ch MAPMT (three fibres per pixel). Commercial optical connectors and clear fibers ensure the connection of the WLSs to the MAPMT.

shielded the prototype from ambient light.
The electronics readout did not require the use of preamplifier Add-on cards, as indicated by the FEE characterization in Section 4.2. A total of 16 discriminator cards with an additional input resistor of 50 Ω, to match the impedance of the MAPMTs, were used. The modification reduced the input charge by approximately 20%. Dedicated PCB adapters were used to connect the cards to the MAPMTs. During the setup particular attention was paid to the grounding scheme within the A1 setup, as ground loops increase the noise level.
The DAQ system was realized with three TRB3s (one master and two slave boards), programmed to read out the 256 NDet channels and the coincidence

signal from the spectrometers. An additional signal from the spectrometers included the A1 trigger number. This was used as an external trigger and to synchronize the acquisition of the TRB3 with the A1 setup. The beam test was the first integration test of the TRB3 into the existing DAQ of A1. All major problems connected to the data transfer and grounding mismatch were successfully solved with the collaboration of the TRB3 Group.
The combination of the high rate on the NDet and low A1 trigger rate (< 500 Hz) required the use of a time window to avoid saturation of the TRB3 buffers. The length (~ 1 μs) and the range were set according to the kinematic conditions and to minimize the number of multiple hits per channel and the A1 trigger latency (~ 500 ns).
The NDet prototype was placed in the forward region of the A1 experimental area, as pictured in Fig. 5.22. A metal support held the detector at the height of the target (~ 3 m), at a distance of ~ 10 m. The prototype covered a horizontal angle of $\sim 6°$. The prototype was positioned at an angle $\alpha = 48°$, which was determined by the kinematic conditions. Various settings were studied, using longitudinally polarized electrons of 855 MeV provided by MAMI.

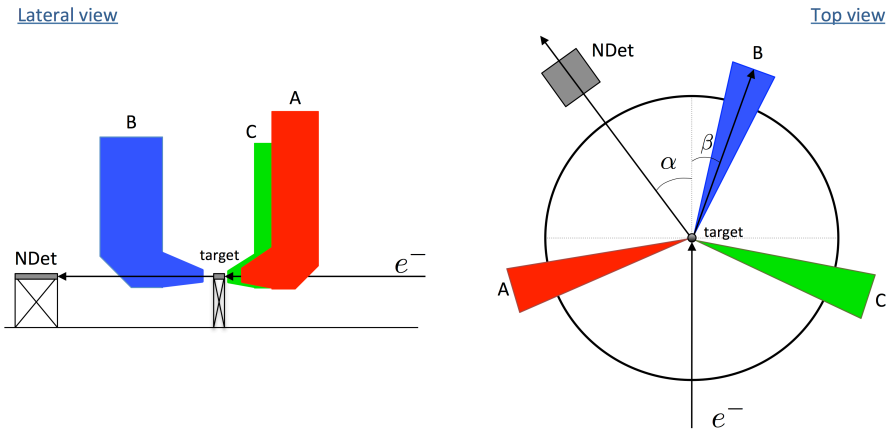

Figure 5.22: Lateral and top view of the experimental area (not drawn to scale). A, B and C indicate the spectrometer positions. Spec. B was used for the coincidence measurement with the NDet.

5.2.2 General results

The beam test provided important information for the full readout chain with plastic scintillators. The TRB3 DAQ showed an excellent performance and adaptability; for example, less than seven in a million events were lost, mainly caused by random bit errors or no matched hits [57] (see Fig. 5.23). These results are comparable with the previous studies for the DIRC (see Section 5.1.2).

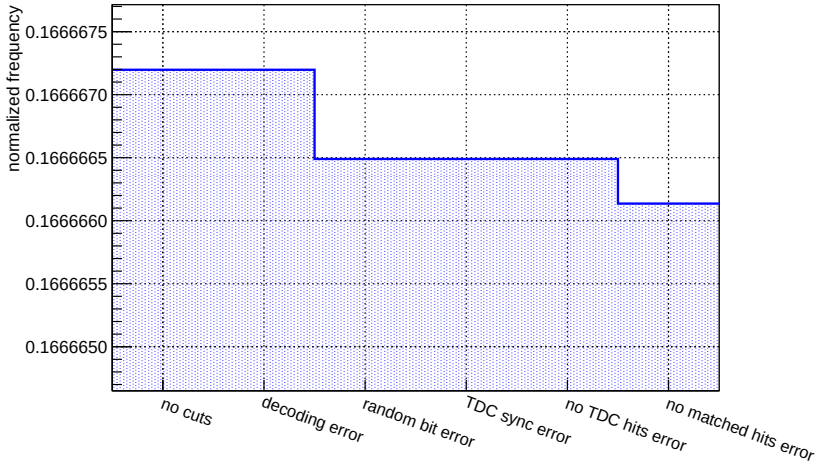

Figure 5.23: Normalized frequency of TRB3 error conditions.

The timing response of the prototype was first studied for all the channels, like in the case of the DIRC. Fig. 5.24 shows the time overlay of all the TDC channels for 10 minutes of data taking. The peaks at ~ -500 ns, ~ -900 ns and ~ -1000 ns belong to the A1 time reference, neutrons and MIPs, respectively. The difference is caused by the different trigger time of π^+ and protons in the A1 setup. The MIPs are mainly background electrons from the elastic scattering

$$e^- + p \rightarrow e^- + p.$$

The timing spectrum allows an easy definition of the online timing windows to [-1200, 150] ns. In particular, 150 ns were added before the MIPs to collect unperturbed data and 75 ns after the A1 trigger (at 0 ns) as required by the

used TDC design [57]. In the offline analysis, the reference time (-600 ns) was subtracted from the arrival time to get rid of the timing jitter of the trigger (around 10 ns).

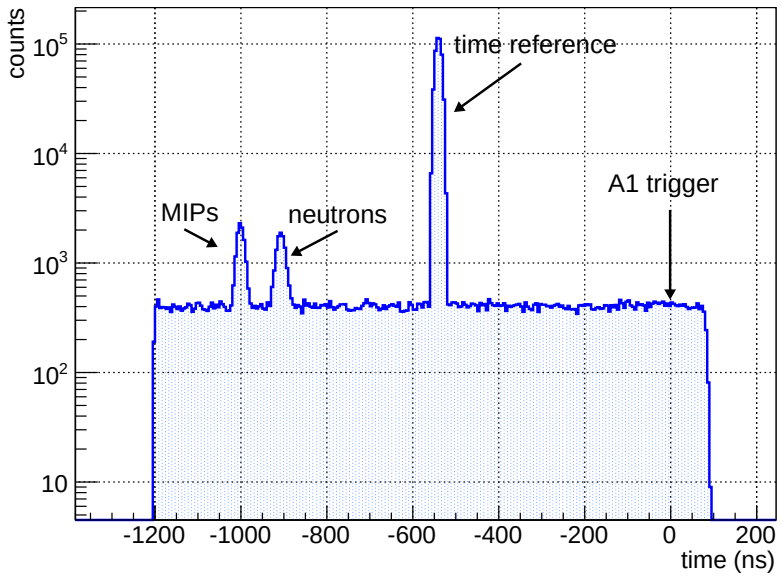

Figure 5.24: Time spectrum of all the channels over 10 minutes data taking.

The FEE ran smoothly without any problems, as in the previous case. The threshold setting required a calibration. In fact, the first data showed an irregular ToT response for the majority of the channels. A calibration based on count rates was applied with the following steps:

1. a channel with a high signal to noise ratio was chosen as reference;
2. a kinematic setting with MIPs only was selected in order to have a homogeneous signal in all scintillator bars;
3. the individual thresholds were set in order to match the count rate of the reference channel.

The method provided a good homogeneity of the ToT for all TDC channels, as shown in the scatter plot in Fig. 5.25.

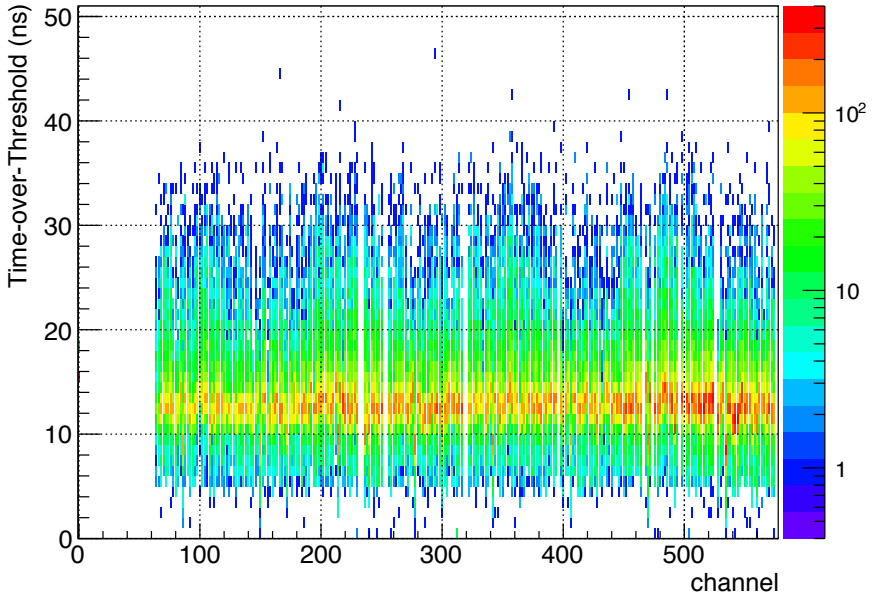

Figure 5.25: ToT response as a function of the TDC channels after threshold adjustment.

5.2.3 Time-over-Threshold response

One of the key requirements for the NDet is the PID of MIPs and neutrons based on the measurement of the deposited charge. The ToT method is commonly used to measure the deposited charge in silicon detectors. Conversely for plastic scintillators, to the best knowledge of the author, only a non-linear ToT method has been proposed by [55]. Moreover, the ToT has never been used for large arrays like the NDet prototype. Prior experiments with a similar detector concept using an ADC-based readout had difficulties due to pile-up effects caused by the high rates [83].
The ToT response to different particles species could be investigated with simple cuts on the arrival time, as explained in the previous section. Fig. 5.26 shows the ToT spectrum as a function of the arrival time (relative to the A1 trigger at 0 ns), where all scintillator bars contribute to the plot. The structure between [-500,-400] ns belongs to MIPs, which are mainly electrons from elastic scattering. The events inside [-400,-300] ns correspond to neutrons. The continuous band around ToT$\approx$ 12 ns is due to uncorrelated background,

e.g. photons. The background events were reduced by applying a simple

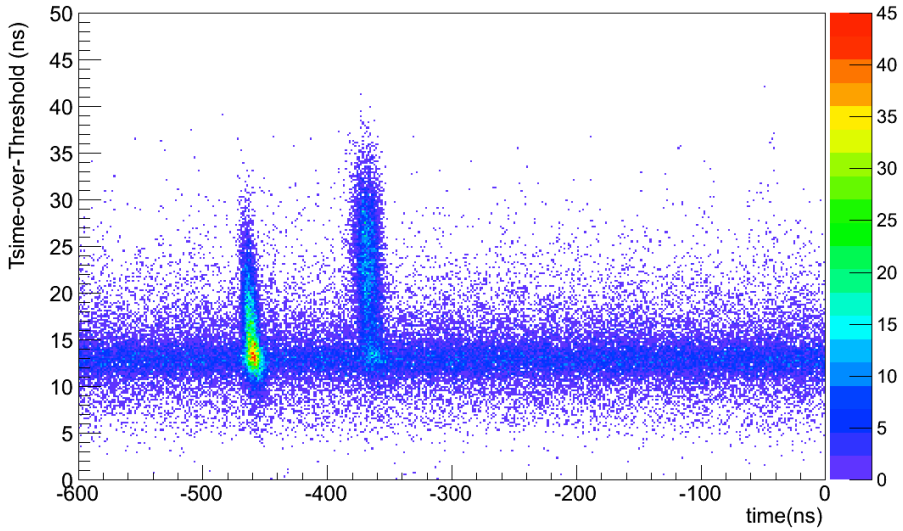

Figure 5.26: ToT response as a function of the relative time to the A1 trigger. The structures between [-500,-400] ns and [-400,-300] ns belong to MIPs and neutrons, respectively, while the continuous band with ToT≈ 12 ns is interpreted as background signals.

algorithm, in which only a coincidence between left and right PMT channel of a scintillator within a time window of 60 ns was accepted. The result in Fig. 5.27 shows a clear noise reduction. The impact of the method was calculated using a ToT-projection of the time interval [-600,-550] ns, as shown in Fig. 5.28. With the integrals of raw (R) and coincidence (C) spectra the background suppression can be defined as follows:

$$bkg_{sup} = 1 - \frac{R}{C} = (85.7 \pm 0.7)\%, \tag{5.7}$$

where the error is calculated with the error propagation of C and R.
The ToT spectra for MIPs, neutrons and background were studied selecting the corresponding regions of interest. Fig. 5.29 shows considerable differences for the ToT. In particular, the response to neutrons is characterized by a larger ToT average with respect to MIPs. Normalizing both spectra and taking into account a cut around the crossing point (≈ 20 ns), the fraction of MIPs in the neutron sample amounts to $(27.7 \pm 0.7)\%$.

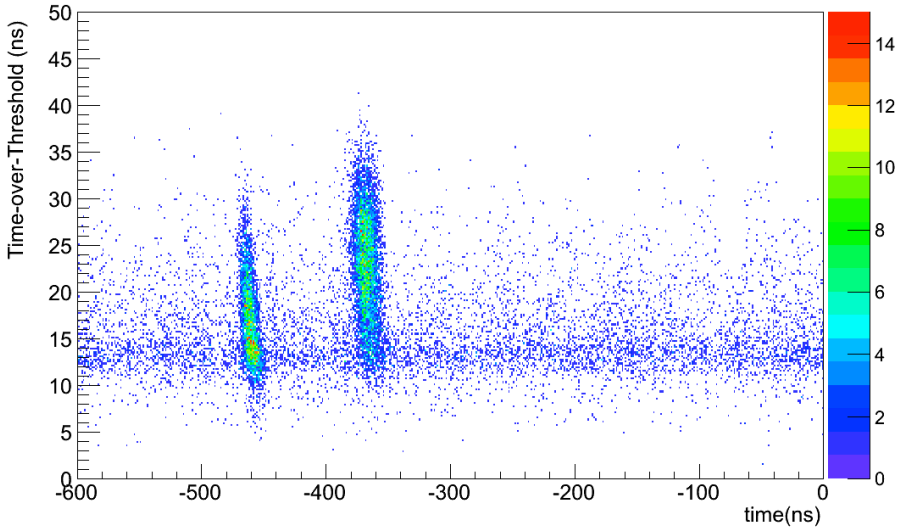

Figure 5.27: Result of the background suppression algorithm applied to the data shown in Fig. 5.26.

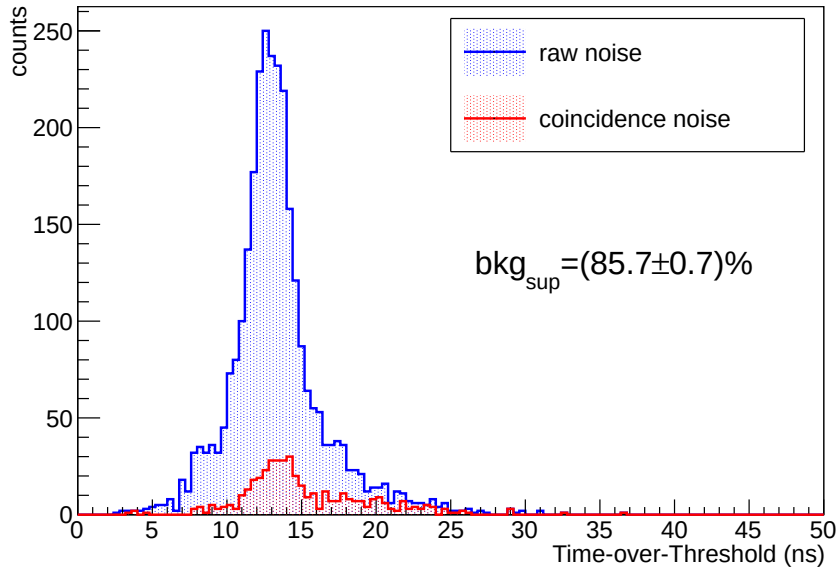

Figure 5.28: ToT spectra of raw and suppressed background events.

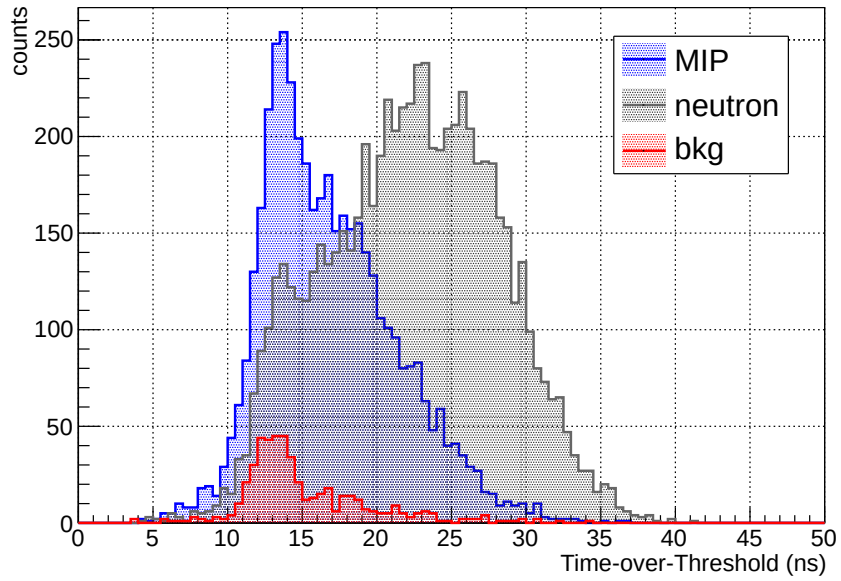

Figure 5.29: ToT response to different particle species.

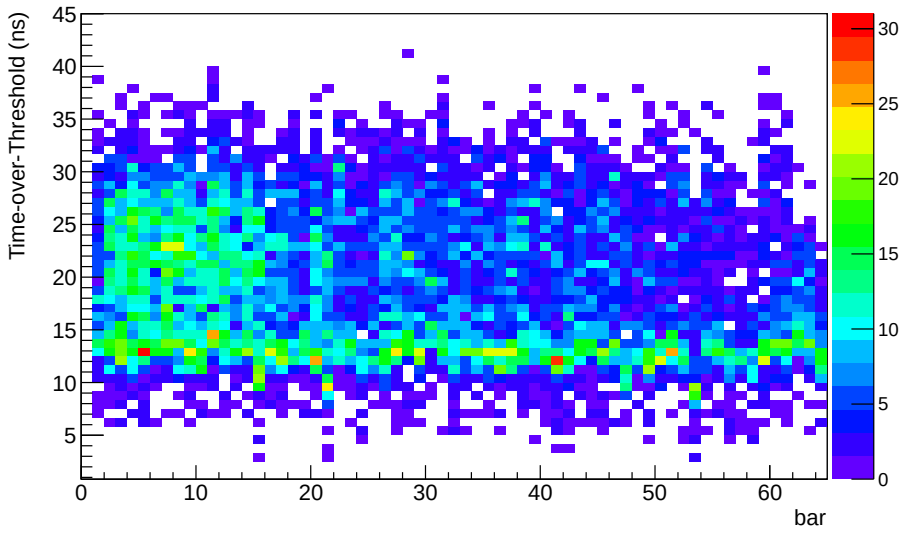

Figure 5.30: ToT response of the scintillator bars along the NDet prototype.

The ToT spatial distribution was also expected to provide additional information to disentangle neutrons and MIPs. The results in Fig. 5.30 show the ToT spectra of incoming particles across the layers. The homogeneous band at ToT≈ 15 ns is due to MIPs which penetrate the entire detector depth. The neutrons cause an excess of events at higher ToT values (20-30 ns), which is observed between the 2^{nd} and the 15^{th} bar.
A dedicated GEANT simulation [84] was used to verify the behaviour of the energy deposit as a function of the bar layer (see Fig. 5.31). Considering the kinematic conditions of the experiment with neutrons at a kinetic energy of approximately 100 MeV, the expectations fully agree with the observations, and predict also the behaviour of the first bar not showing a ToT excess for neutrons.

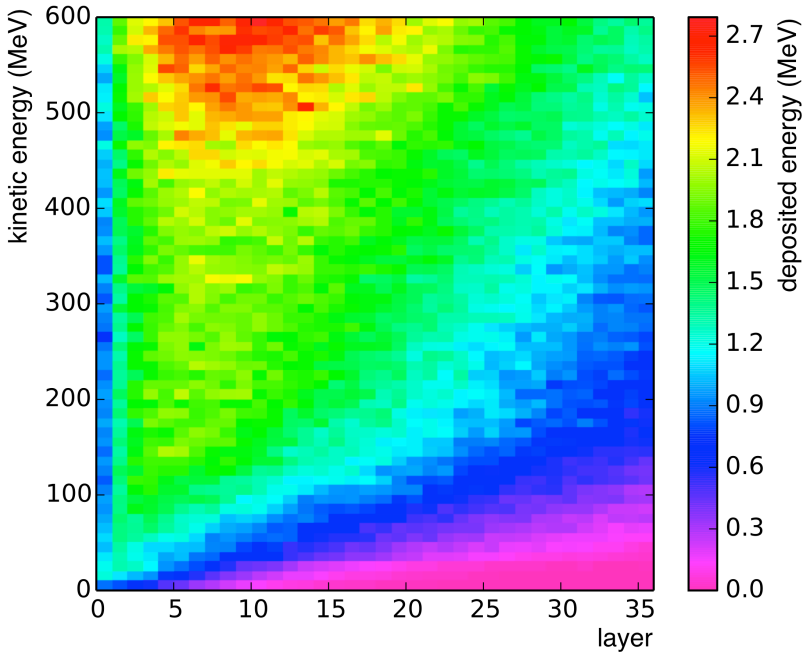

Figure 5.31: Simulation of the deposited energy of neutrons per layer [84]. In the test experiment the kinetic energy of neutrons was approximately 100 MeV.

The measured ToT spectra do not show any saturation effects (see Section 4.2.1). The result proves that the dynamic range of the FEE is sufficient

for the tested NDet prototype.

5.2.4 Timing performance

The timing performance of the NDet was investigated considering the time difference between left and right PMT channels of the bars. In principle, this analysis would not be possible without knowing the particle track. However, the small acceptance of the spectrometers allowed a selection, within a few cm, of particles hitting the middle of the prototype. Fig. 5.32 shows the timing spectra for a bar hit by neutrons (according to the previous results). The Gaussian fit shows a large timing resolution of $\sigma_t \approx 4$ ns, compatible with approximately 1/3 of the bar width. Previous investigation with a radioactive source (see Section 4.2.2) reported a similar result with much less uncertainty of the particle impact point. The poor timing performance is caused most likely by a low light yield of the prototype.

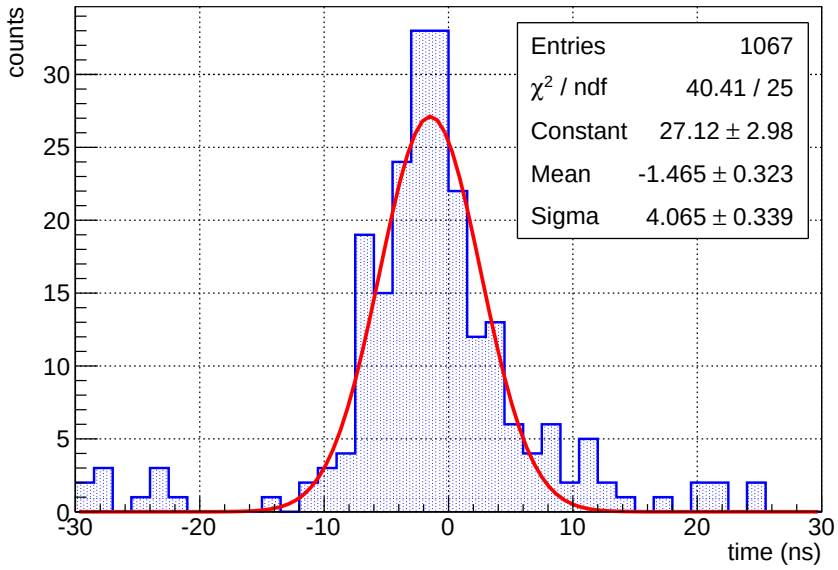

Figure 5.32: Timing resolution of the bar for neutrons.

Furthermore, this hypothesis was confirmed by the low number of hit bars per event, as shown in Fig. 5.33, where the number of left-right coincidences per event are displayed for neutrons and MIPs. Both curves show a peak

at 1, thus excluding the possibility of efficient particle tracking in this test experiment. The tracking is also limited by particles scattered outside the prototype due to its small acceptance.

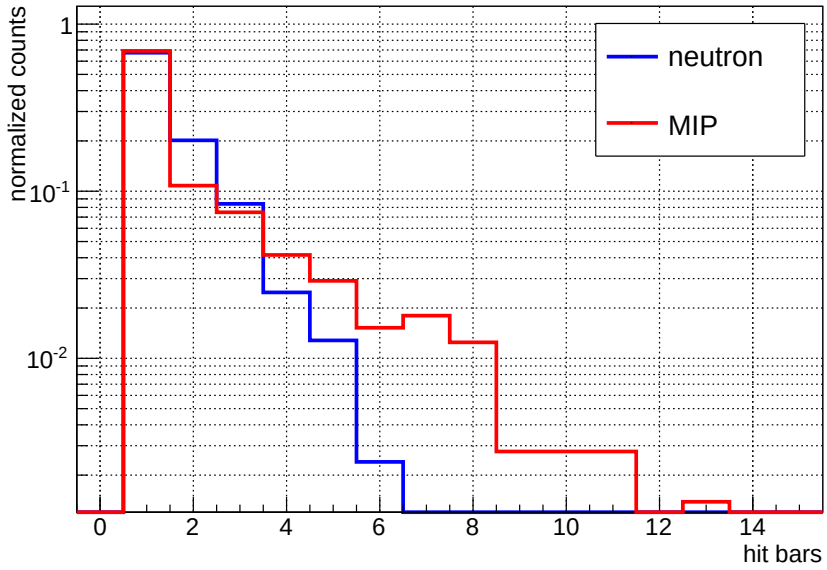

Figure 5.33: Number of hit bars per event for MIPs and neutrons.

5.2.5 Rate Capability

The main requirement for the NDet is a high count rate per channel on the order of several MHz. The NINO ASIC can sustain rates larger than 10 MHz [63, 64]. However, the single ended scheme adopted for the FEE had to be validated for such high rates. A high beam current (approximately 10 μA, with a luminosity of $\sim 10^{38}$ cm^{-2}s^{-1} [84]) as used for a previous measurement of the neutron electric form factor at A1 [37] was chosen for the studies. Typically three different problems can occur at high rates:

I. the ring buffer of the TDC channels fills up and the TRB3 starts to drop the older hits;

II. the FPGA buffer gets full and some of the channels are not stored;

III. the maximum event size is reached and the event is closed, loosing the rest of the information.

For event rates of several MHz with a 500 Hz trigger the first issue (I) cannot be solved by design and part of the information *outside* the region of interest is lost. Setting a limit for the number of hits per channel outcomes the second problem (II), while the third (III) is addressed by an online timing window. Considering the trigger window of $T = 1.2$ μs set for the TRB3 readout, and the number of hits per channel N_{hits}, the average rate could be reconstructed as follows:

$$rate = \frac{N_{hits}}{T}. \tag{5.8}$$

The result is shown in Fig. 5.34. A fit with a gaussian distribution gives a mean count rate of 2.8 MHz per channel. Peaks up to 12 MHz were observed in the online monitor of the TRB3. Under these conditions no saturation effects or ToT artifacts were discovered, which confirms the high rate capability of the developed FEE.

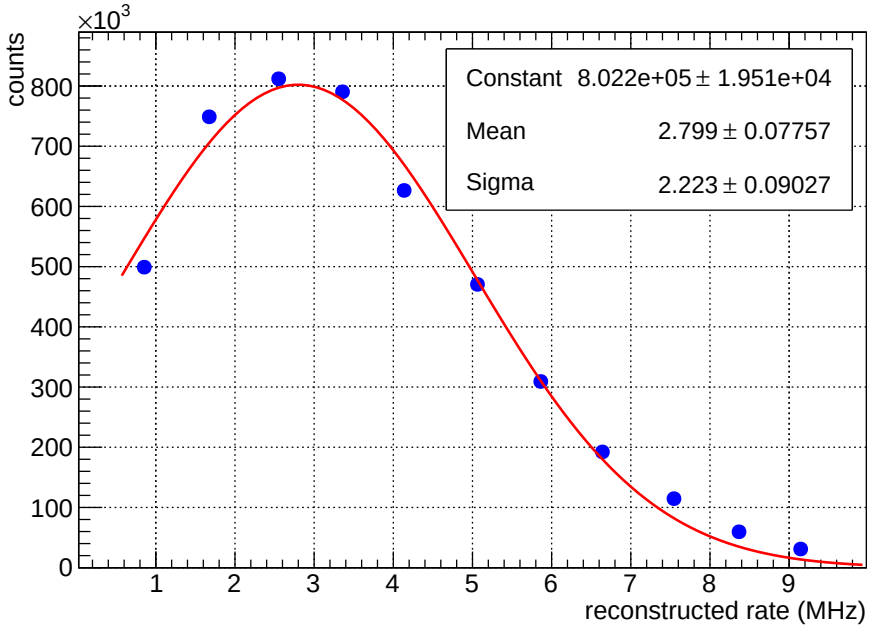

Figure 5.34: Reconstructed rate for a high beam current setting (approximately 10 μA).

The results presented in this section clearly indicate that the electronics meets the requirement of the A1 NDet. Like in the DIRC case, the full readout chain achieves high performance with smooth operation.
The response of the whole prototype was made homogeneous using the individual threshold of the FEE. This feature will be even more important in the final detector, where a uniform response will be crucial for tracking capability.
The implementation of thresholds in the discriminator boards also keeps the design simple. Alternatives like Add-on cards with adjustable amplifiers (or attenuators) would have much larger dimensions [85] and will not fit the general requirements of multi-purpose FEE (see Section 1.1). Moreover, large dimensions make the electronics integration in compact detectors difficult.
As the results show, the dynamic range of the electronics satisfies a broad range of applications and it classifies this FEE as multi-purpose. The ToT information successfully provides a measurement of the deposited charge in plastic scintillator. The PID performance in the final NDet will be also enhanced by the ToT distribution along the bars.
More studies are needed to establish the timing resolution of the NDet. However, this is only connected to the low light yield of the used prototype. Indeed, recent studies have shown that the low light yield of the prototype was caused by the manufacturing process of the scintillator bars. Since the timing resolution in scintillators scales as $1/\sqrt{N}$, where N is the number of detected photoelectrons [86], an improved resolution is expected for the new prototype and the final detector.
The advantage of discriminator logic becomes clear at high rates. The absence of a gate, like in ADC chips, reduces undesirable effects like pile-up. The FEE achieved a counting rates up to almost 12 MHz without showing side effects. This electronics outclasses the rate capability of the single-purpose FEE used for the NeuLAND experiment.
This excellent result is a mandatory ingredient for the measurement of the neutron FFs with unprecedented resolution.

Chapter 6

Future Developments

The previous chapters show the potential of the developed FEE with significantly different types of detectors. Currently, new interesting applications are under investigation, exploiting and enhancing the FEE performance. In the next pages, an example of a fast start counter based on the detection of Cherenkov light will be described and the preliminary results obtained in a test experiment will be presented.

Recently, a new category of FEE based on FPGAs and ToT method became available. The same characterization techniques developed for the NINO FEE were useful for the early study of this new FEE. The results could be directly compared to the performance of the NINO, as presented in the second part of this chapter.

6.1 A Fast Start Counter

The measurement of ToF has played an important role in particle physics. Nowadays, a new category of detectors, which uses the Cherenkov effect, aims at reaching unprecedented timing resolutions on the order of tens of ps. Such performance will allow a broad range of applications. For example, proton detectors with high timing resolutions (10 ps) could be used in ATLAS and CMS to study central exclusive reactions, like $p + p \rightarrow p + p + H$ [87].
A precise ToF system for PID in beam tests is reported in this section. The aim was the identification of charged kaons and pions in mixed particle beams. Considering a flight length of 6 m at 3 GeV/c, a timing resolution in ToF

measurements below 60 ps is needed to achieve 3σ separation.
The detector is inspired by the QUARTIC design [88]. In this case, small fused silica bars ($90 \times 6 \times 6$ mm^3) are coupled to a 64 channel MCP-PMT with 10 μm pore structure. The small pore diameter enhances the timing performance compared to the 25 μm MCP-PMT used for the DIRC prototype. The particle beam enters the radiator bars with an angle approximately equal to the Cherenkov angle θ_c; e.g. particles at $\beta \approx 1$ enter the prototype with an angle $\theta = acos(1/n) \approx 48.3°$, as schematically shown in Fig. 6.1 (a). Part of the emitted light propagates along the bar axis and reaches the photodetector without any reflections. As a consequence, the timing spread caused by the radiator is minimized, and the light reaches the MCP-PMT at the same time (isochronous design). The direct connection also enhances the photon yield, thus increasing the timing performance. The final timing resolution improves with the number of hit radiator bars N as:

$$\sigma_t = \frac{\sigma_{1 \text{ bar}}}{\sqrt{N}}, \tag{6.1}$$

where $\sigma_{1 \text{ bar}}$ is the timing resolution obtained with only 1 bar. The original QUARTIC experiment obtained a timing resolution of 88 ps for a high energy proton beam (120 GeV) and a similar setup [89].

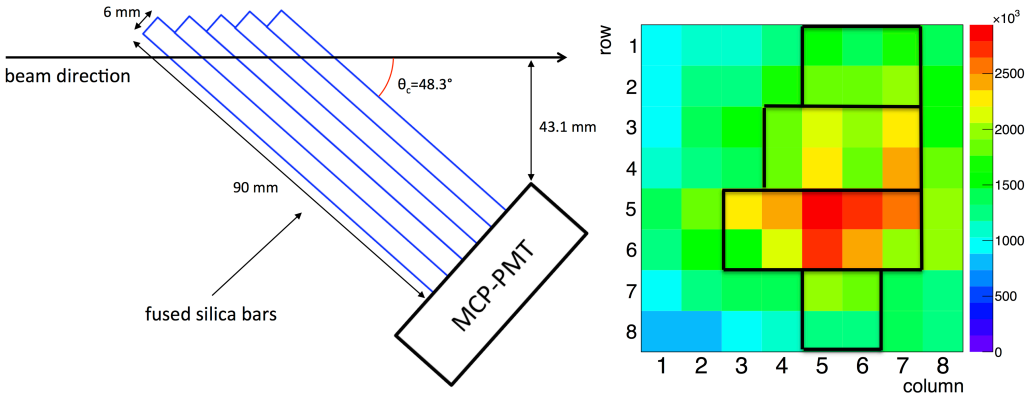

(a) (b)

Figure 6.1: (a) schematic view of the QUARTIC design used for the test experiment. (b) Gain uniformity of the used MCP-PMT [90]. The black lines delimit the pixels connected to radiator bars.

A test experiment with two such counters was performed at the X1 beam line of MAMI, in the test area described previously in Section 5.1. The counters were assembled with 28 radiator bars each, using different configurations with 2, 3, 4, 5 bars to systematically study the effect of the material budget and verify Eq. 6.1. The pixels with higher gain were connected to the radiator bars, as shown in Fig. 6.1 (b).
The FEE together with the TRB3 DAQ contributes for 39 ps when the proper walk correction is applied (see Section 5.1.4). In order to minimize the impact of a synchronization jitter to less than 20 ps, the TRB3 was modified accordingly, as described in Section 3.1.1. As in the case of the DIRC prototype, the MCP-PMTs were equipped with preamplifier Add-on and discriminator cards.

In two days of data taking several systematic studies were done to optimize gain and threshold settings, and to investigate light attenuation in the bars. The preliminary results show an excellent efficiency close to 1 on photon detection. Fig. 6.2 shows the intensity plots for 20,000 events of the two MCP-PMT used in the two fast counters. The beam hits the detectors in rows equipped with 5 radiator bars each. The difference in counts between the two unit depends on the material budget. In particular, the second unit detects a wider beam due to multi-scattering. Observation event-by-event, showed the evidence of cross-talk between rows. Ongoing studies will disentangle the contributions of electronical and optical cross-talk. Nevertheless, the measured ToT allows to identify the pixel with larger signals and thus to select the right hits.

A preliminary estimate of the timing resolution was obtained considering the average time differences between the different bars. A total of 5 independent bar combinations was used and the corresponding time spectrum is shown in Fig. 6.3. A final interpretation of the average time will require a precise absolute time calibration, which is planned for the future. However, the preliminary timing resolution can be extracted from the Gaussian fit and is $\sigma_t \approx 79$ ps. The value surpasses the QUARTIC result without considering any major corrections. Indeed, only a ToT cut was applied in the preliminary analysis. Advanced time walk corrections are carefully under investigation which is not part of this thesis [91].

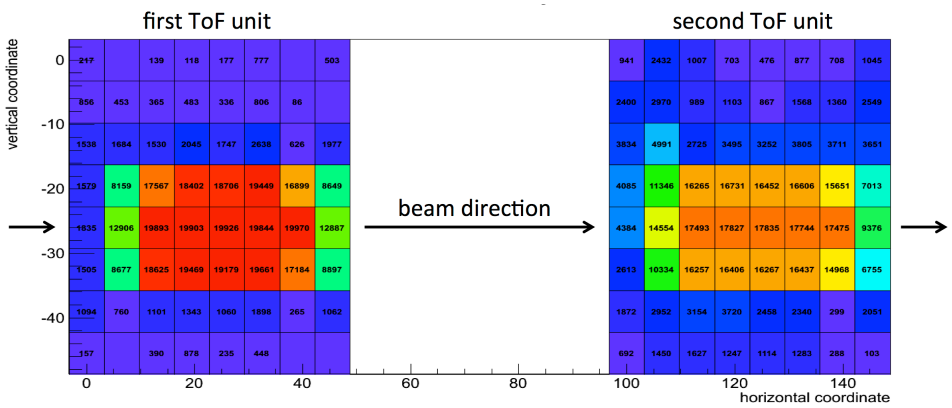

Figure 6.2: Overlay of 20,000 events in the two fast counter units studied in the test experiment. The arrows indicate the beam directon.

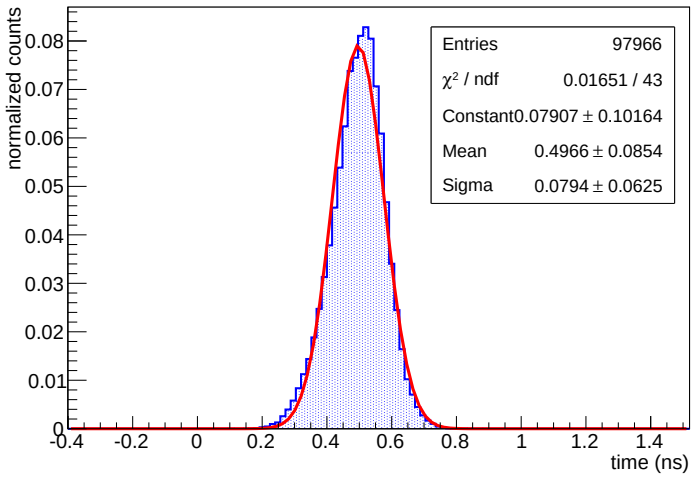

Figure 6.3: Average ToF for 5 bar combinations. The Gaussian fit is used to calculate the timing resolution.

The result clearly shows the high flexibility of the FEE. Its design, originally developed for the Barrel DIRC, proves high performance for the readout of this prototype. The different input signals due to a higher light yield, with respect to imaging Cherenkov counters, is perfectly matched by the FEE without any adjustments. The setup will be investigated at CERN to achieve the first measurement of its PID performance.

6.2 FPGA-based FEE

The technological progress in the field of ASICs will soon bring new chips with better characteristics than the NINO. The same philosophy of fast discriminators and triggerless readout will be applicable. In the field of electronics for SP detection an alternative to the NINO could be the CLARO chip, currently under development for the RICH upgrade of LHCb [92]. On the other hand the development of ASICs with new transistor technology always requires large investments.
An alternative way is offered by FEE designs based on FPGAs, which shift the problem from hardware to software. Indeed, such devices allow the realization of circuits which can be tuned to the desired application with a firmware update.
An example is the first generation of the PaDiWa card (Panda Dirc Wasa),

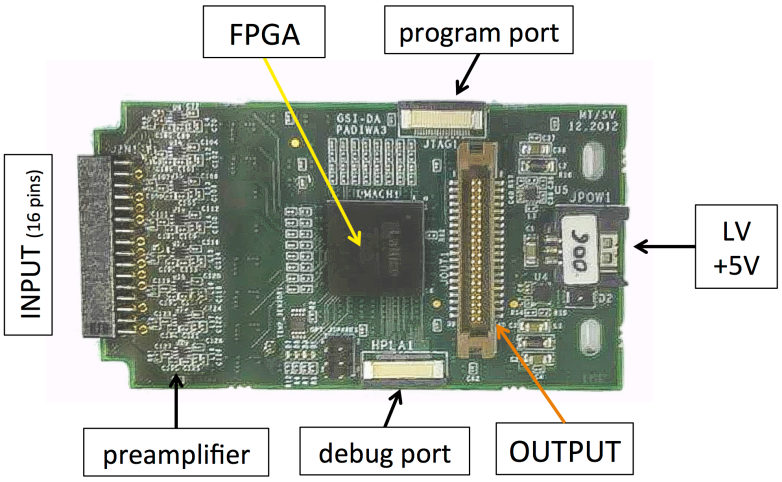

Figure 6.4: Photo of the PaDiWa card.

which became available during the thesis, and was developed at GSI by the TRB3 Group [93, 94]. The card is a PCB (9.5 cm long, 5.2 cm wide, see fig. 6.4) which integrates a fast preamplifier[1] (23 dB, up to 2.2 GHz bandwidth) and an FPGA[2]. Each card has 16 input channels, with a power consumption of 80 mW/channel (half of the NINO FEE when used with preamplifier Add-on).

[1]NXP, BGA2803
[2]Lattice MachXO2

The FPGA performs the task of threshold generation, discrimination, LVDS transmitter and self-trigger generation. In particular, the thresholds are generated using the FPGA as a DAC through a pulse width modulator followed by a low pass filter. The discrimination stage is implemented using the LVDS input buffers. The output and the slow control is fully based on LVDS signals and can be easily configured with TRB3 setups. The board features also a temperature sensor for online monitoring and threshold stabilization.
The possibility of reprogramming PaDiWa opens the way to multiple applications. For example the board can be used as coarse TDC with a timing precision of 500 ps RMS. ADC firmwares are a possibility as well, which will soon be available.
The first studies involving PaDiWa have been focussing on the board optimization for SP signals. The procedure developed during the thesis were applied to this FEE. A complete characterization was carried out with the laser setup described in Section 4.1. Like in the previous case, a linear trend of the leading edge time as function of ToT was found, as shown in Fig. 6.5. A linear fit to the profile allowed the extraction of the time walk parameters.

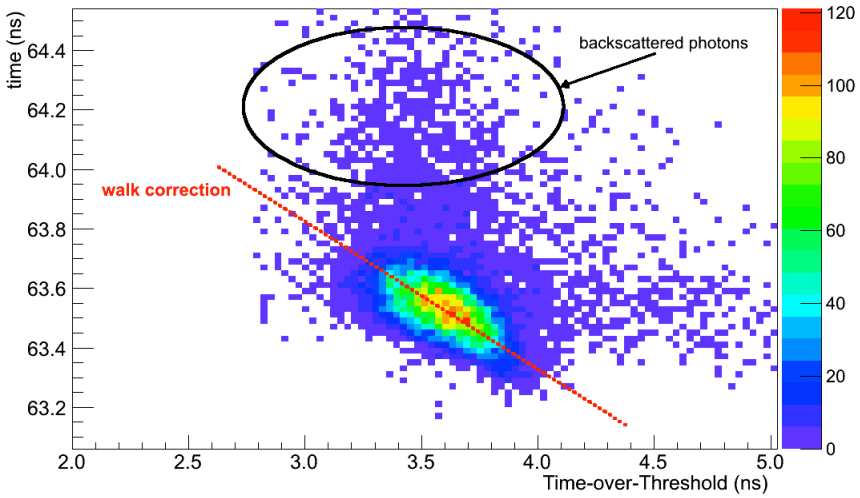

Figure 6.5: Scatter plot of the arrival time of photons as a function of ToT.

The corrected time spectrum, see Fig. 6.6, shows a timing resolution of about $\sigma_{fit} \approx 78$ ps, with a gain of 13.3% compared to the raw time.

Following Eq. 4.8 and 4.9, the PaDiWa timing resolution is $\sigma_{FEE} \approx 54$ ps. The result outperforms the FEE based on NINO by 25%, showing high potential for this new technology.

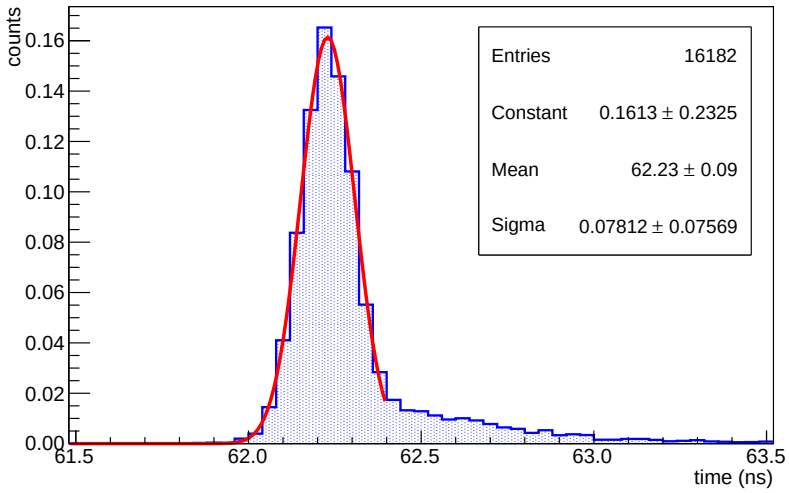

Figure 6.6: PaDiWa time spectrum after time walk correction.

Further tests in the use of large PaDiWa setups revealed major problems, which are currently under investigation. The efficiency of the card was also observed to be lower than the NINO FEE, with unstable results caused by a complicated threshold setting procedure.
Apart from small design mistakes which require a second iteration of R&D, the main concern about PaDiWa is the robustness of FPGAs in radiation environments. Indeed, this could severely limit the range of detectors which can be equipped. More studies to investigate the radiation hardness of the PaDiWa FPGA are ongoing. Designs with radiation hard FPGAs will also be considered in the future.

Chapter 7

Conclusion

Can a clever FEE design be successfully used for the readout of significantly different detectors? The presented results demonstrate that the need of expensive developments of new ASICs for single-purpose FEE can be reduced by adapting existing high performance chips. Smart designs allow new features not available in the original circuit, thus enhancing its initial performance and broadening the range of applications of the FEE.
The versatile concept of a fast discriminator was chosen to realize a precise, trigger-free and low power FEE. In particular, the NINO chip was selected as core component for its unique timing capabilities. Single ended input and individual thresholds were implemented successfully. A preamplifier Add-on card was also designed to increase the dynamic range of the FEE and, thus, expanding the possible range of applications.

The response to single photon events, essential for imaging Cherenkov detectors, was first investigated with a fast laser pulser, allowing a detailed characterization of the FEE. The ToT information was successfully exploited to correct the time walk, obtaining a timing resolution for the whole readout chain of 84.0 ± 0.5 ps. During a test experiment with a small scale DIRC prototype, the FEE achieved an excellent intrinsic resolution of 40 ± 1 ps and a detector timing resolution of $\sigma_{prot} \sim 100$ ps. The obtained performance meets the strong requirements of detectors like the Barrel DIRC of PANDA.

The results of the A1 NDet studies proved the versatility of the FEE design, which can be also used to read out plastic scintillator arrays. The ToT could be used as a simple ADC-method to measure the deposited energy and

to identify MIPs and neutrons. The observed neutron distribution along the NDet prototype fully agreed with a Monte Carlo simulation. An additional tuning of the FEE could improve the achievable resolution, which was limited in the current prototype by the scintillator light yield. Further investigations on a new design with higher light yield will be performed in the future. The FEE met the most demanding requirement of high count rates, obtaining an average of 2.8 MHz per channel (with peaks up to 12 MHz) without any signal degradations.

The presented results provide a clear proof of concept of multi-purpose FEE using discriminators and ToT information. A clever and simple design exploits existing ASICs in applications beyond their original scope. The performance is excellent for all considered detectors. Ongoing studies on fast ToF detectors confirm the high flexibility of this FEE. The result of this studies demonstrates the great potential of this approach in FEE development.

[...] *"Illud in his rebus vereor, ne forte rearis*
impia te rationis inire elementa viamque
indugredi sceleris. quod contra saepius illa
religio peperit scelerosa atque impia facta.
Aulide quo pacto Triviai virginis aram
Iphianassai turparunt sanguine foede
ductores Danaum delecti, prima virorum.
Cui simul infula virgineos circum data comptus
ex utraque pari malarum parte profusast,
et maestum simul ante aras adstare parentem
sensit et hunc propter ferrum celare ministros
aspectuque suo lacrimas effundere civis,
muta metu terram genibus summissa petebat.
Nec miserae prodesse in tali tempore quibat,
quod patrio princeps donarat nomine regem;
nam sublata virum manibus tremibundaque ad aras
deductast, non ut sollemni more sacrorum
perfecto posset claro comitari Hymenaeo,
sed casta inceste nubendi tempore in ipso
hostia concideret mactatu maesta parentis,
exitus ut classi felix faustusque daretur.
Tantum religio potuit suadere malorum." [...]

Lucrezio, *De Rerum Natura*, 80-101.

Appendix A

Signal Characterization

The following plots refer to Section 2.1.3.

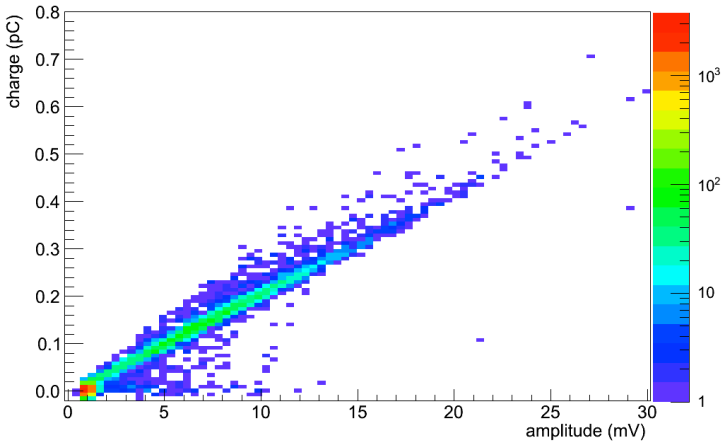

Figure A.1: Scatter plot showing the amplitude as function of the charge for an MCP-PMT under SP conditions (colors according to the intensity). The red spot at low charge is produced by pedestal noise [51].

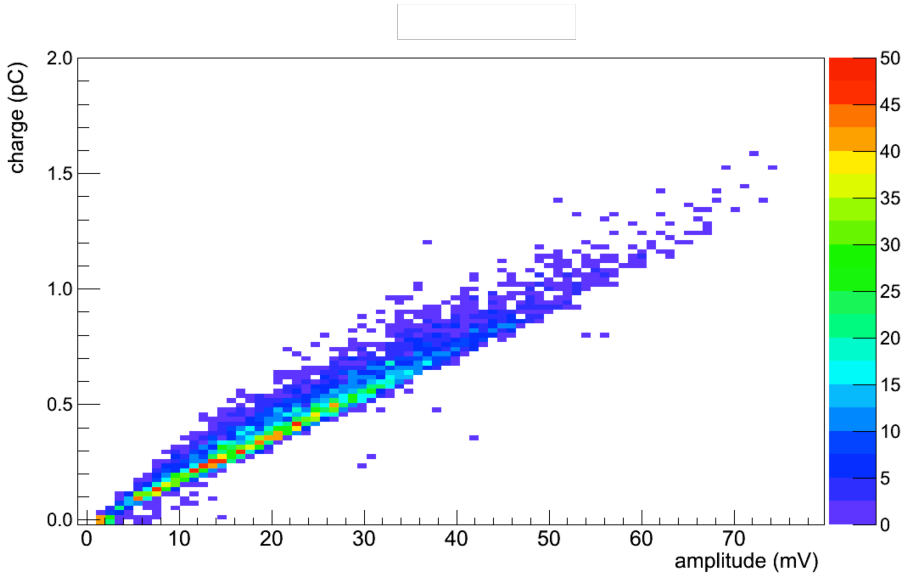

Figure A.2: Scatter plot showing the amplitude as function of the charge for an MCP-PMT with NDF 4.0 (colors according to the intensity) [51].

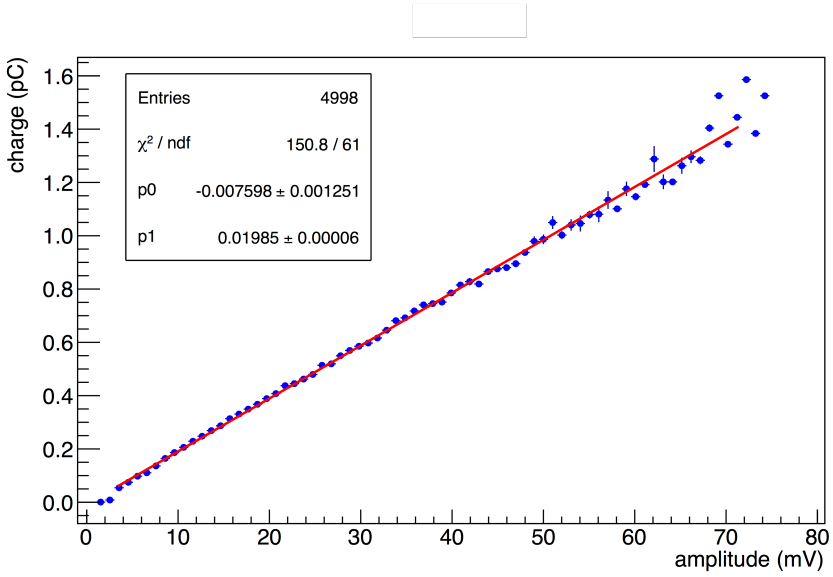

Figure A.3: Profile of the previous plot fit with a straight line [51].

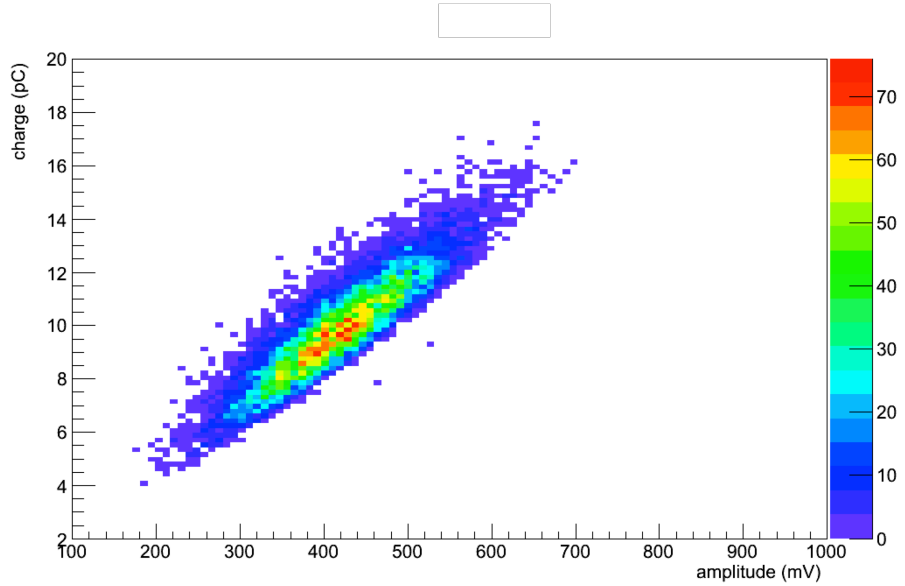

Figure A.4: Scatter plot showing the amplitude as function of the charge for an MCP-PMT with NDF 3.0 (colors according to the intensity) [51].

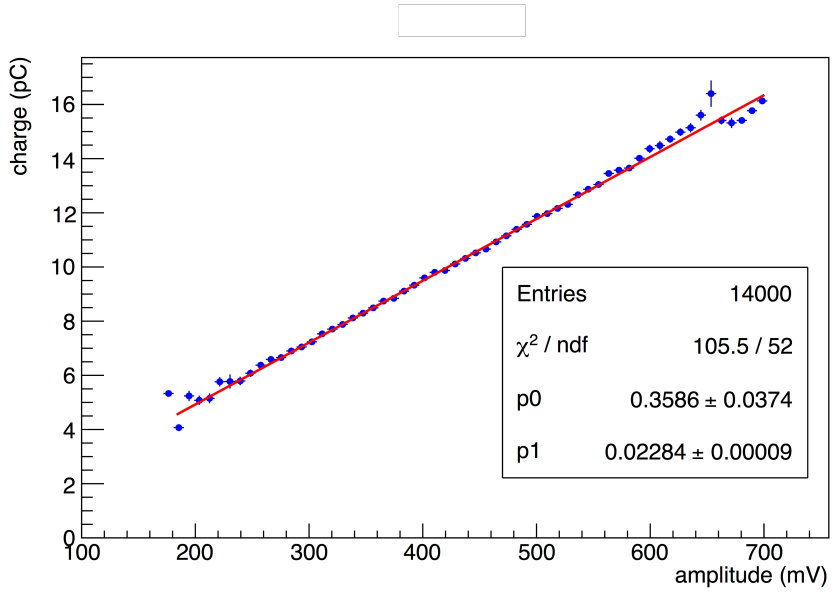

Figure A.5: Profile of the previous plot fit with a straight line [51].

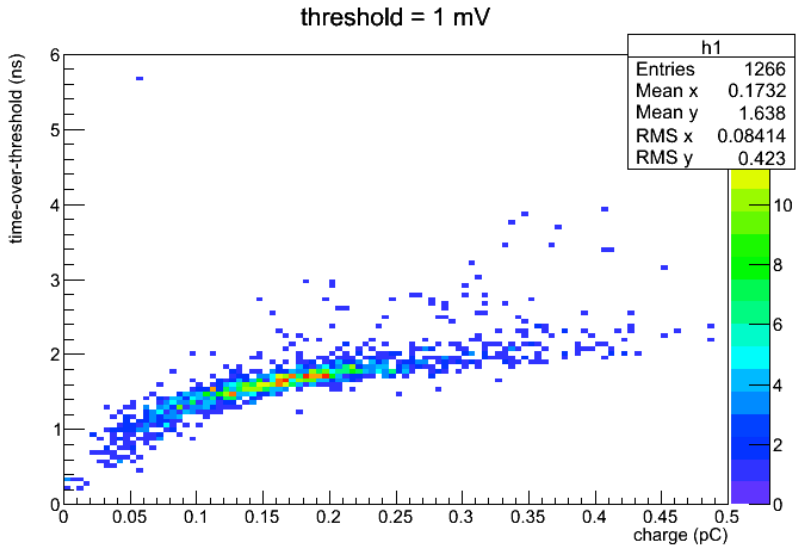

(a)

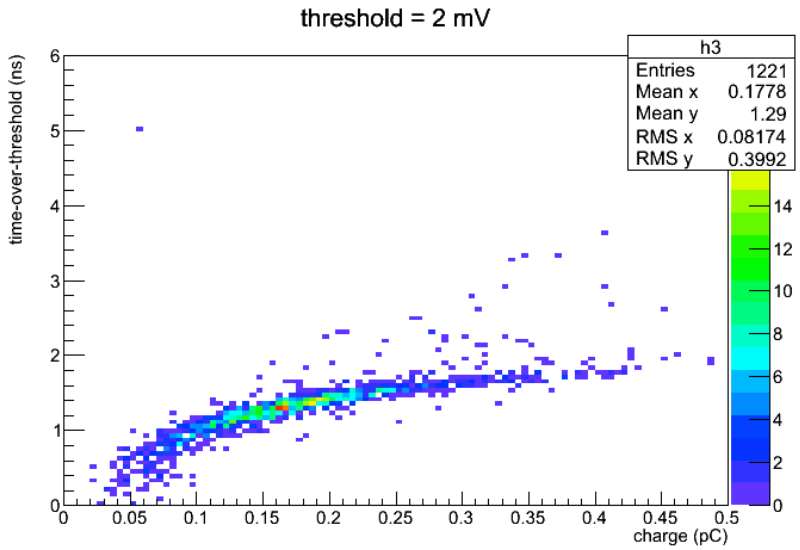

(b)

Figure A.6: Scatter plot showing the amplitude as function of the ToT at the threshold level of 1 mV (a), 2 mV (b) [51].

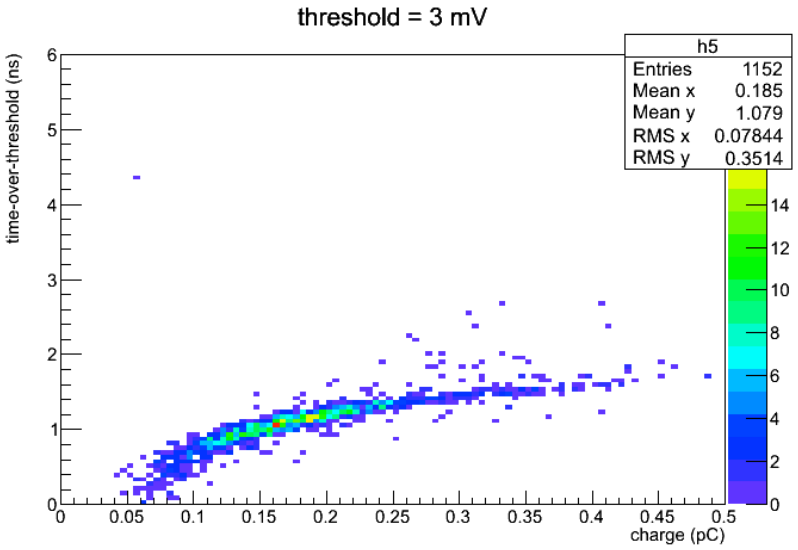

(a)

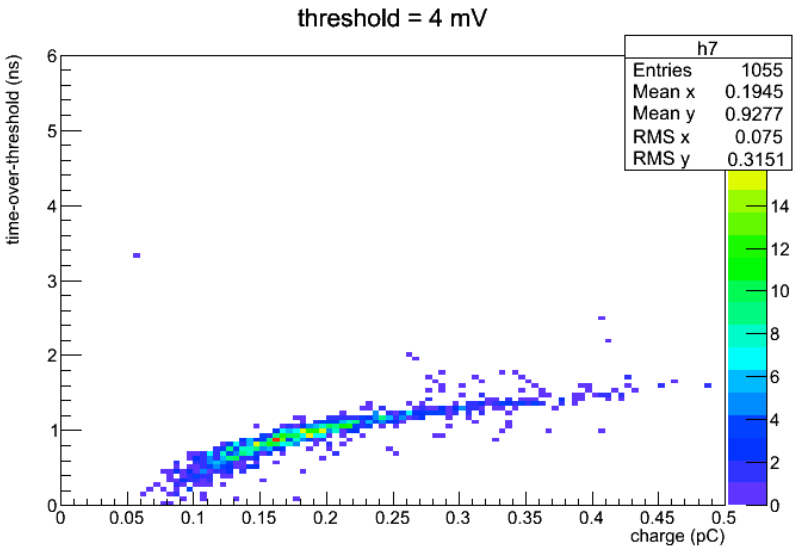

(b)

Figure A.7: Scatter plot showing the amplitude as function of the ToT at the threshold level of 3 mV (a) and 4 mV (b) [51].

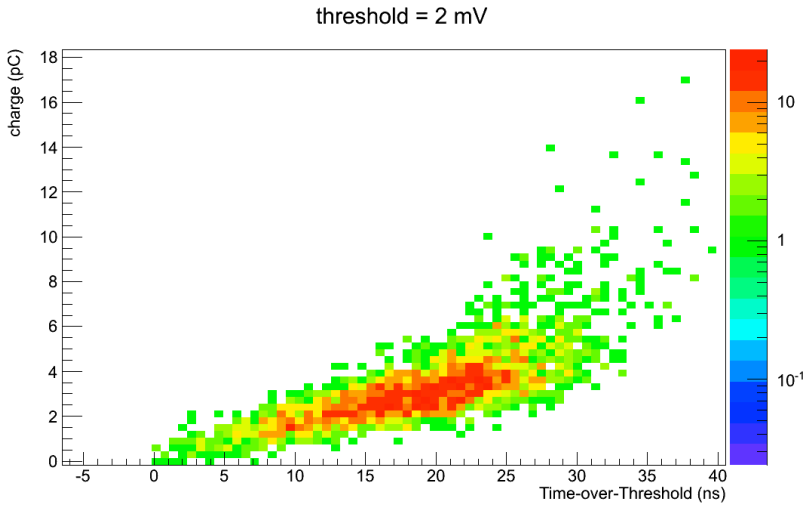

Figure A.8: Intensity plot of charge as function of ToT. The threshold on the amplitude is 2 mV.

Appendix B

Electronics layouts

B.1 TRB3 synchronization

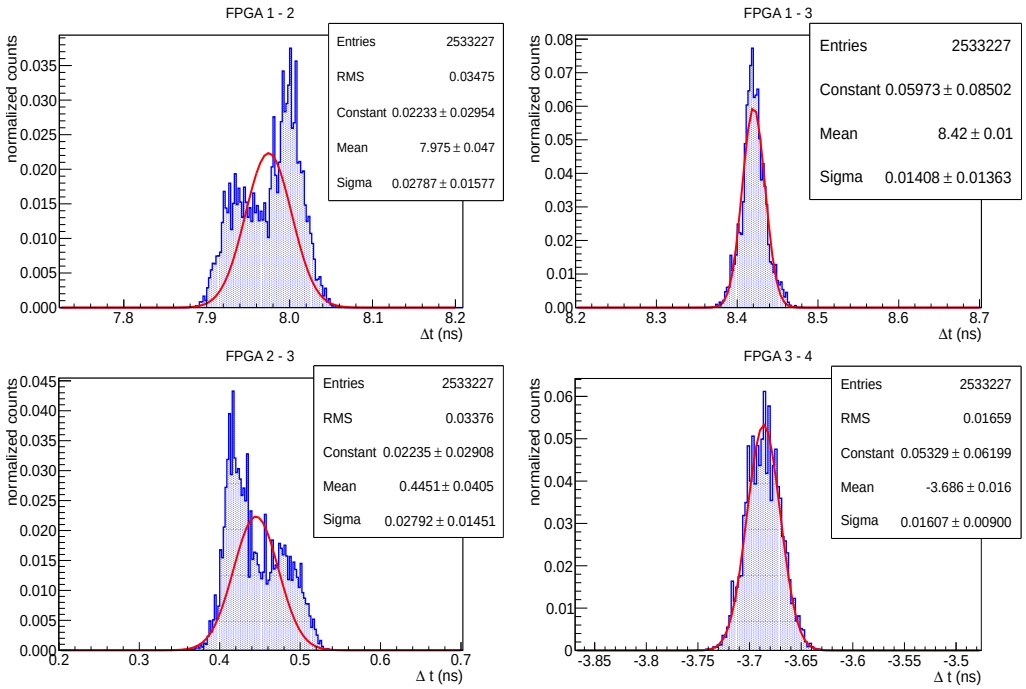

Figure B.1: Synchronization precision between FPGA 1 & 2, FPGA 1 & 3, FPGA 2 & 3 and FPGA 3 & 4.

B.2 FEE Schematics

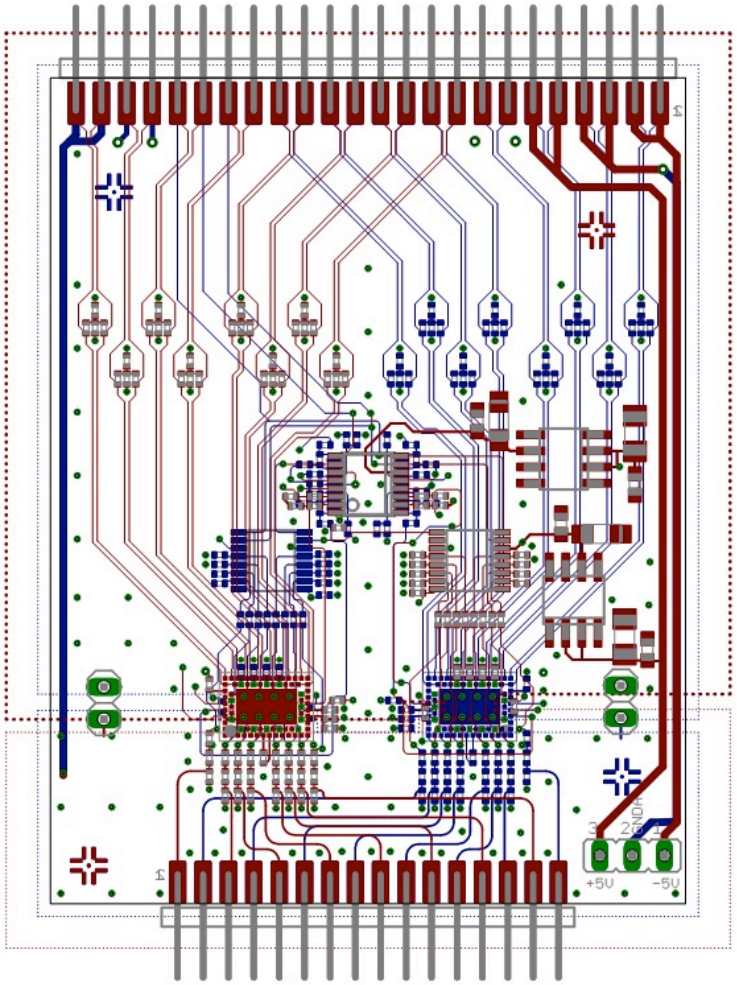

Figure B.2: Layout drawing of the the discriminator.

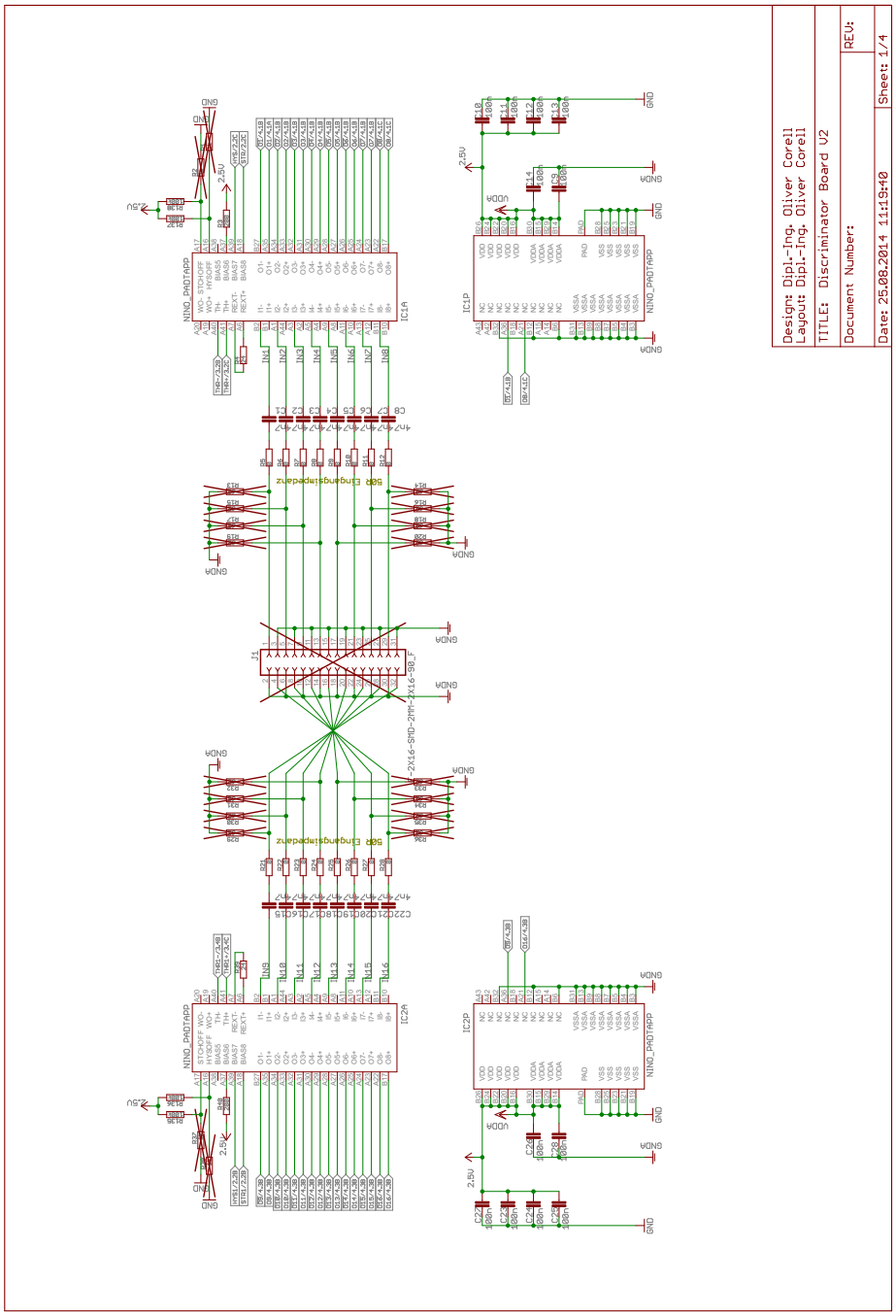

Figure B.3: *1st part*: discriminator board schematics.

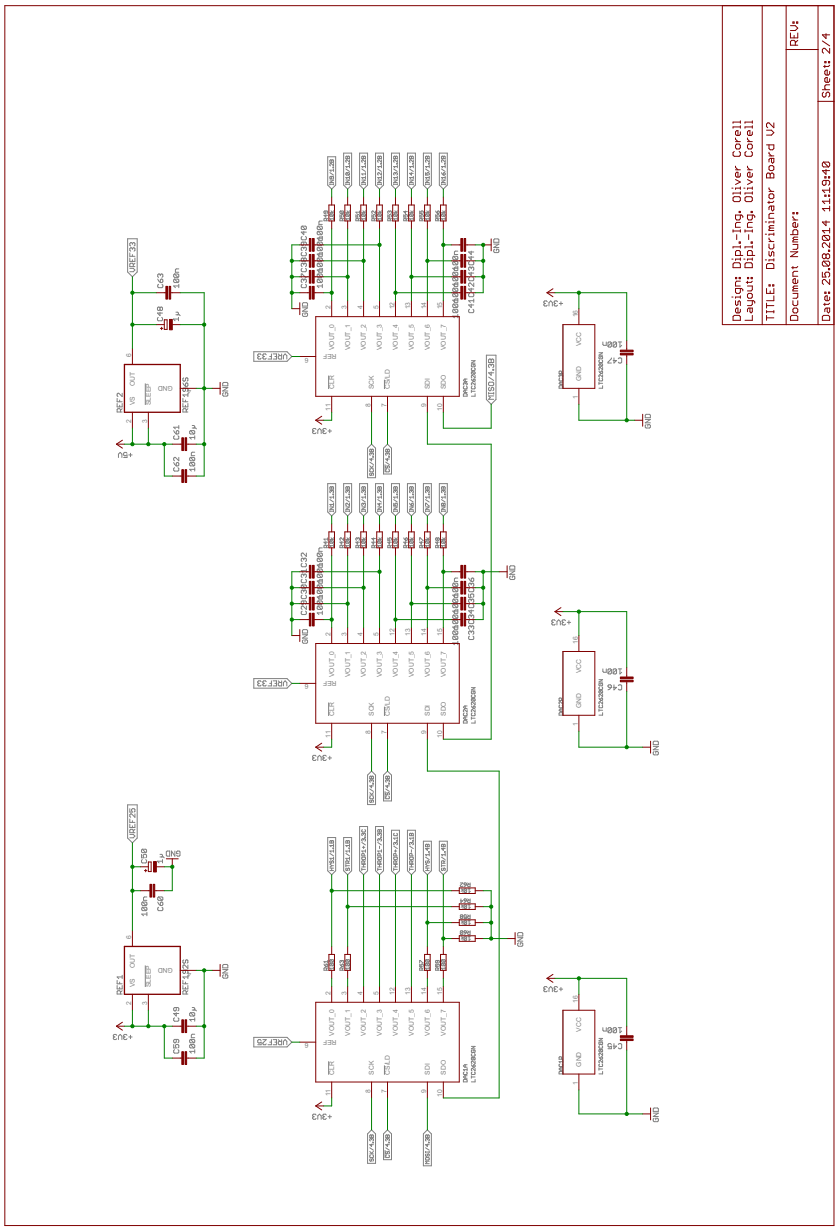

Figure B.4: *2nd part*: discriminator board schematics.

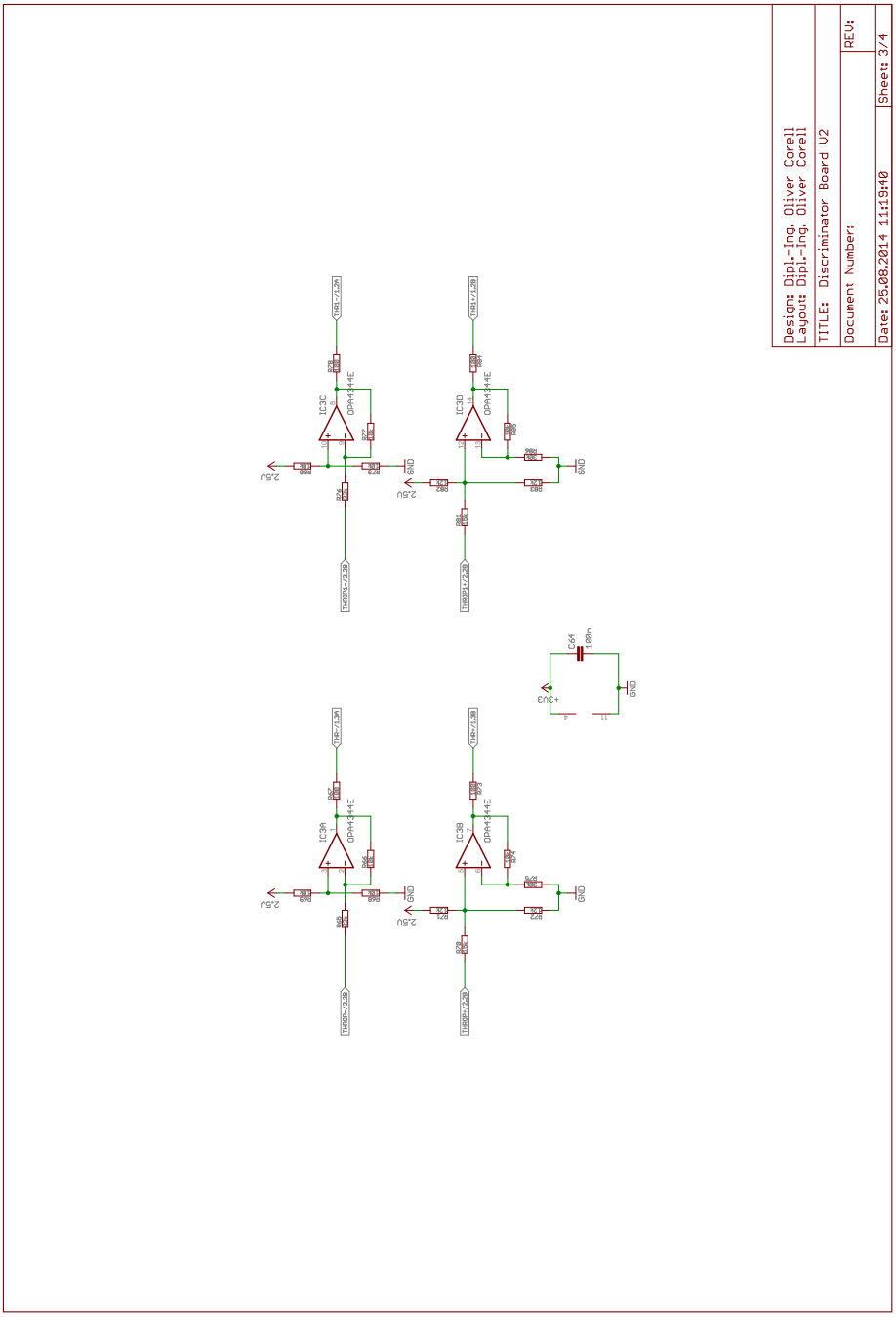

Figure B.5: *3rd part*: discriminator board schematics.

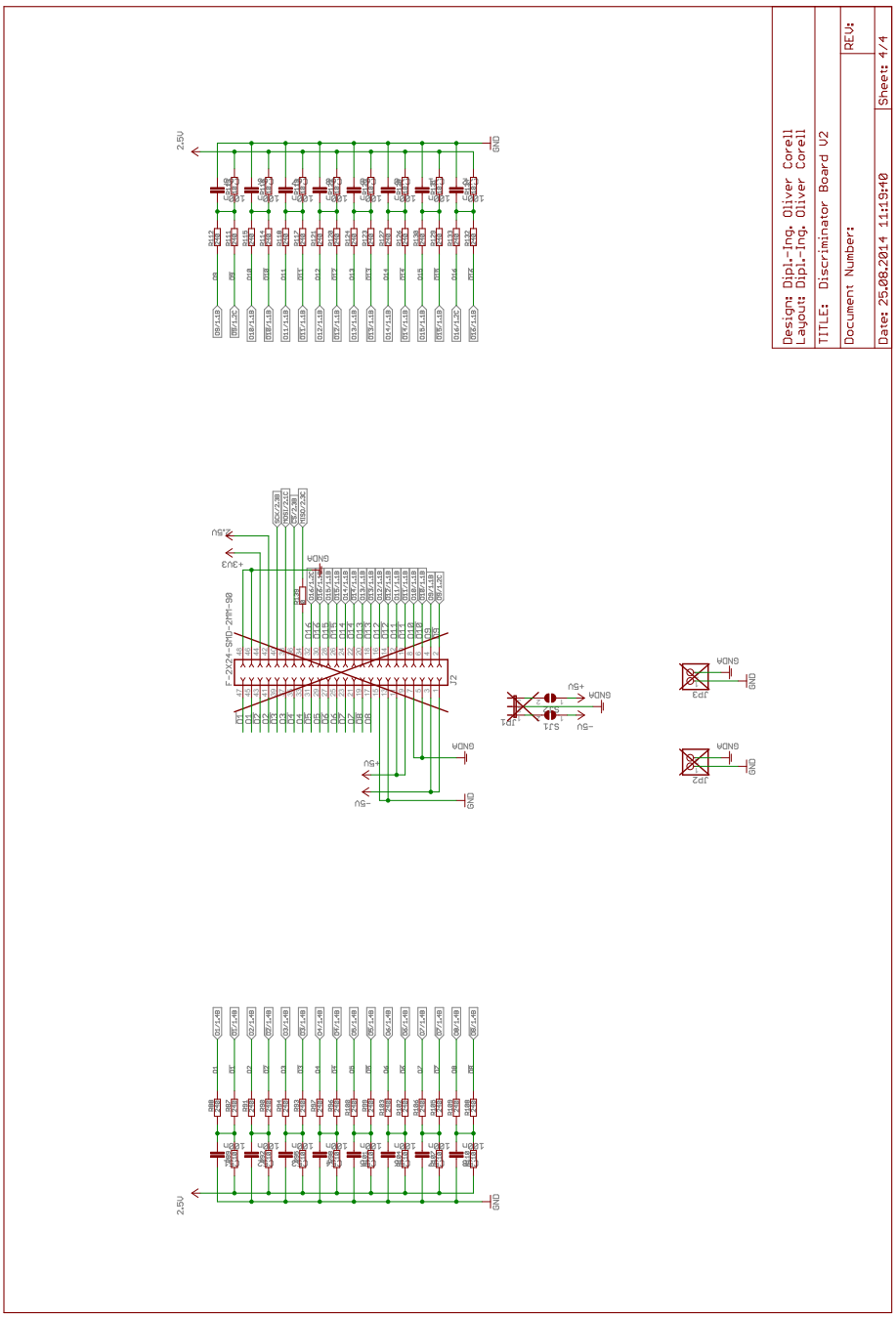

Figure B.6: 4^{th} *part*: discriminator board schematics.

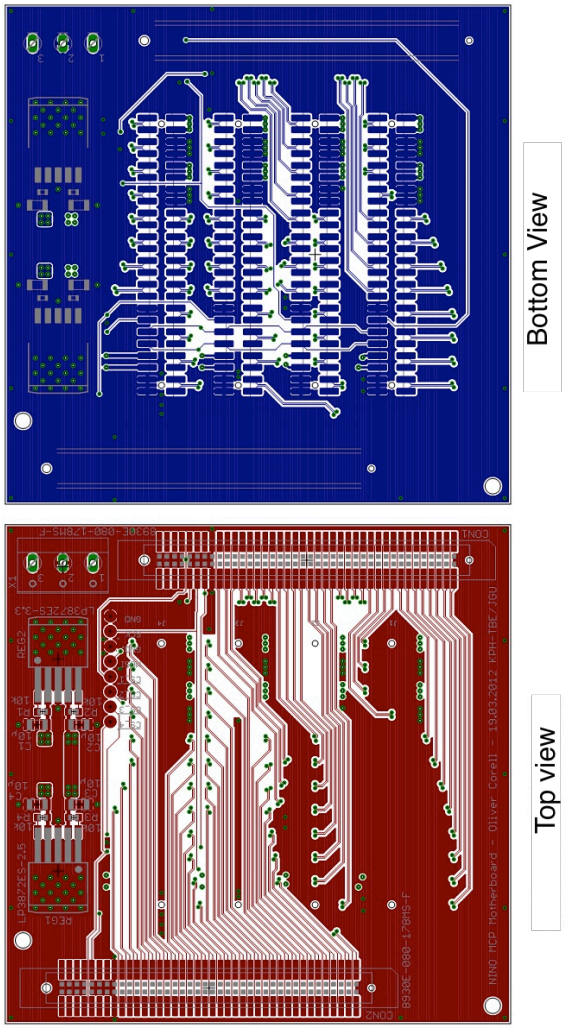

Figure B.7: Top and bottom view of the layout drawing for the FEE mother board.

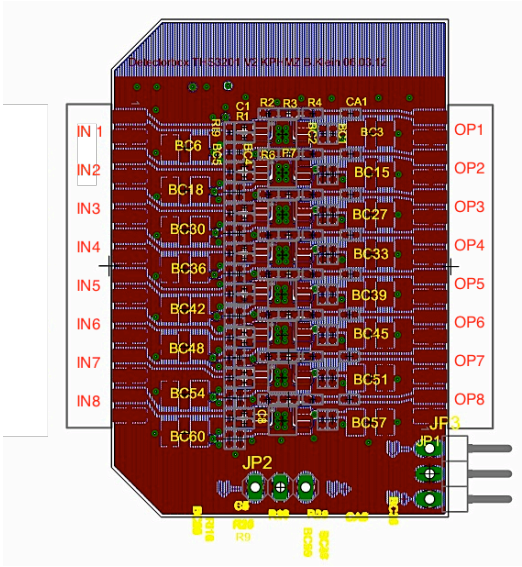

Figure B.8: Layout drawing of the preamplifier.

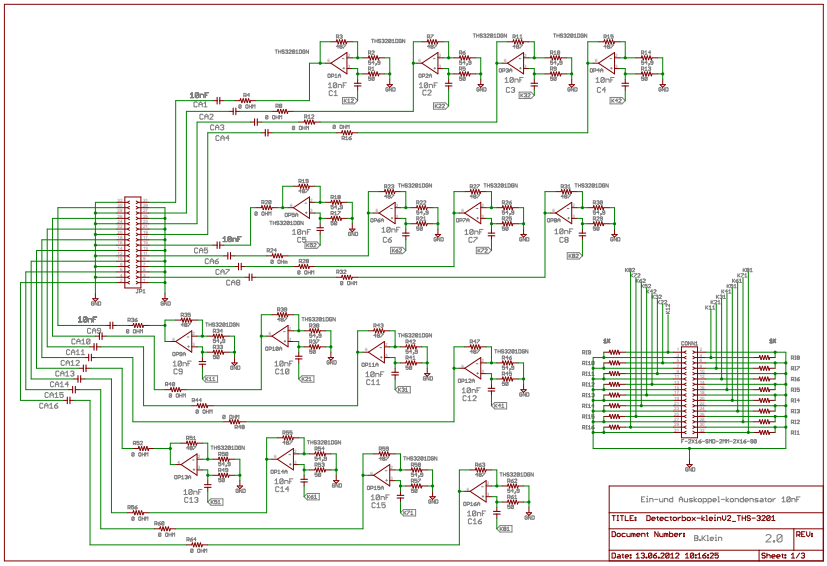

Figure B.9: *1st part*: preamplifier board schematics.

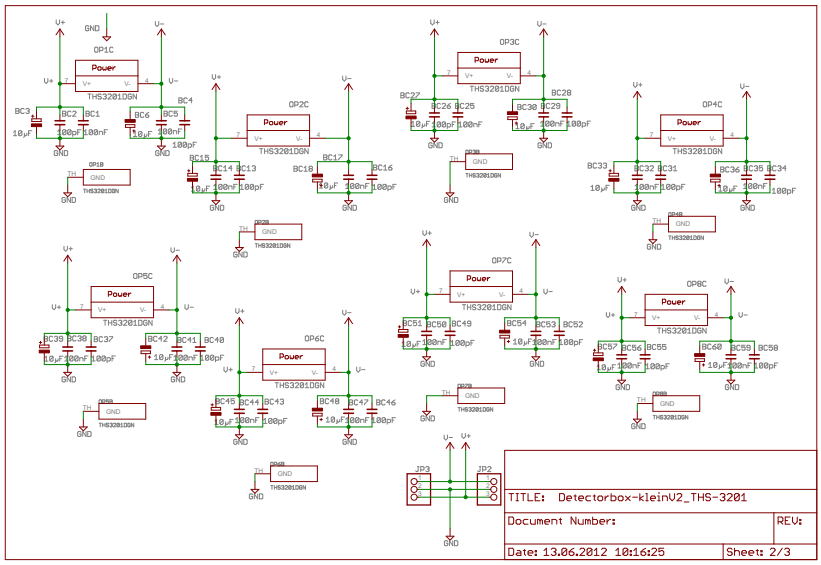

Figure B.10: *2nd part*: preamplifier board schematics.

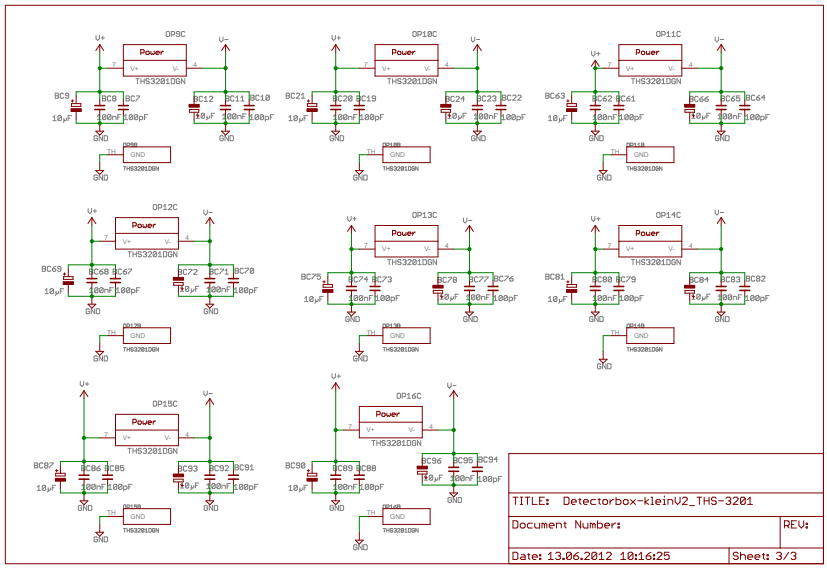

Figure B.11: *3rd part*: preamplifier board schematics

Bibliography

[1] ATLAS Collaboration, "Observation of a new particle in the search for the Standard Model Higgs boson with the ATLAS detector at the LHC," *Phys. Rev. Lett.*, no. B716, pp. 1–29, 2012.

[2] CMS Collaboration, "Observation of a new boson at a mass of 125 GeV with the CMS experiment at the LHC," *Phys. Rev. Lett.*, no. B716, pp. 30–61, 2012.

[3] Z. Wang, "Recent results at BESIII," *Nucl. Instr. Meth. Proc.*, no. 258–259, pp. 129–134, 2015.

[4] A. Vinokurova, "Study of exotic states in charmonium family at Belle," *Nuclear and Particle Physics Proceedings*, no. 258-259, pp. 135–138, 2015.

[5] "Perspectives of Nuclear Physics in Europe," 2010. [Online]. Available: http://www.nupecc.org/pub/lrp10/lrp2010_final_hires.pdf

[6] G. De Geronimo, "Trends in front-end ASICs for particle physics," in *TIPP 2014 Conference, Amsterdam*, 2014, http://indico.cern.ch/event/192695/session/1/contribution/433.

[7] M. Hoek et al., "The PANDA Barrel DIRC detector," *Nucl. Instr. Meth.*, no. A766, pp. 9–13, 2014.

[8] PANDA Collaboration, "Physics performance report for panda: Strong interaction studies with antiprotons," *ArXiv*, no. 0903.3905, 2009.

[9] M.Thiel et al., "Development of a neutron detector for A1@ MAMI," *Proceedings of Science (Bormio 2012)*, 2012. [Online]. Available: http://pos.sissa.it/archive/conferences/160/010/Bormio2012_010.pdf

[10] A. Jankowiak et al., "The Mainz Microtron MAMI – Past and future," *Eur. Phys. J. A*, no. 28, pp. 149–160, 2006.

[11] "Facility for Antiproton and Ion Research," http://www.fair-center.eu/fileadmin/fair/publications_FAIR/FAIR_Broschuere_autumn2013_V3_72dpi.pdf, 2013.

[12] S. Lange et al., "New Studies of XYZ States at PANDA," *ArXiv*, no. 1311.7597v1, 2013.

[13] PANDA Collaboration, "Technical design report for the PANDA (AntiProton Annihilations at Darmstadt) Straw Tube Tracker," *Eur. Phys. J. A*, no. 49, 2013.

[14] ——, "Technical Design Report for the: PANDA Micro Vertex Detector," *ArXiv*, no. 1207.6581, 2012.

[15] O. Merle et al., "Development of an Endcap DIRC for PANDA," *Nucl. Instr. Meth.*, no. A766, pp. 96–100, 2014.

[16] I. Tamm, "Radiation emitted by uniformly moving electrons," *J. Phys. USSR.*, no. 1, p. 439, 1939.

[17] T. Ypsilantis, J. Seguinot, "Theory of ring imaging Cherenkov counters," *Nucl. Instr. Meth.*, no. A343, pp. 30–51, 1994.

[18] P. Glässel, "The limits of the ring image Cherenkov technique," *Nucl. Instr. Meth.*, no. A433, pp. 17–23, 1999.

[19] B. N. Ratcliff, "Imaging rings in Ring Imaging Cherenkov counters," *Nucl. Instr. Meth.*, no. A502, pp. 211–221, 2003.

[20] I. Adam et al., "The DIRC particle identification system for the BaBar experiment," *Nucl. Instr. Meth.*, no. A538, pp. 281–357, 2005.

[21] B. Dey et al., "Design and performance of the focusing DIRC detector," *Nucl. Instr. Meth.*, no. A775, pp. 112–131, 2015.

[22] K. Inami et al., "TOP counter for particle identification at the Belle II experiment," *Nucl. Instr. Meth.*, no. A766, p. 58, 2014.

[23] N. Harnew, "TORCH: A Large-Area Detector for Precision Time-of-Flight Measurements at LHCb," *Nucl. Instr. Meth.*, no. A37, pp. 626–633, 2012.

[24] Schott AG, "Optical Glass Data Sheets," 2013.

[25] A. Lehman et al., "Improved lifetime of microchannel-plate PMTs," *Nucl. Instr. Meth.*, no. A766, pp. 138–144, 2014.

[26] K. I. Blomqvist et al., "The three-spectrometer facility at the Mainz microtron MAMI," *Nucl. Instr. Meth.*, no. A403, p. 263, 1998.

[27] H. Herminghaus et al., "The Design of a Cascaded 800 MeV Normal Conducting C.W. Race Track Microtron," *Nucl. Instr. Meth.*, no. 138, p. 1, 1976.

[28] K.H. Kaiser et al., "Harmonic Doubled Sided Microtron (HDSM)," *Nucl. Instr. Meth.*, no. A593, p. 159, 1976.

[29] J. Bernauer, "Measurement of the elastic electron-proton cross section and separation of the electric and magnetic form factor in the Q^2 range from 0.004 to 1 $(\mathrm{GeV/c})^2$," Ph.D. dissertation, Johannes Gutenberg-Universität Mainz, 2010.

[30] C. Perdrisat, V. Punjabi, and M. Vanderhaeghen, "Nucleon Electromagnetic Form Factors," *Prog. Part. Nucl. Phys.*, no. 59, pp. 694–764, 2007.

[31] "MIT Bates Linear Accelerator Center." [Online]. Available: http://mitbates.lns.mit.edu/bates/control/main

[32] "ELSA Electron Accelerator." [Online]. Available: http://www-elsa.physik.uni-bonn.de/index_en.html

[33] "CEBAF at JLab." [Online]. Available: https://www.jlab.org/research

[34] M. O. Distler, J. C. Bernauer, T. Walcher, "The RMS charge radius of the proton and Zemach moments," *Phys. Lett. B*, no. 696, pp. 343–347, 2011.

[35] F.J. Ernst, R.G. Sachs, and K.C. Wali, "Electromagnetic form factors of the nucleon," *The Physical Review*, no. 119, 1960.

[36] H. Gao et al., "Measurement of the neutron magnetic form-factor from inclusive quasielastic scattering of polarized electrons from polarized He-3," *Phys. Rev. C*, no. 50, pp. 546–549, 1994.

[37] B. S. Schlimme et al., "Measurement of the Neutron Electric to Magnetic Form Factor Ratio at $Q^2 = 1.58$ GeV^2 Using the Reaction $^3He(e, e^{'}n)pp$," *Phys. Rev. Lett.*, no. 111, 2013.

[38] C. Herberg et al., "Determination of the neutron electric form factor in the $D(e, e^{'}n)p$ reaction and the influence of the nuclear binding," *Eur. Phys J. A*, no. 5, pp. 131–135, 1999.

[39] M. Ostrick et al., "Measurement of the Nucleon Electric Form Factor $G_{E,n}$ in the Quasifree ^{2}H($\overrightarrow{e}$,$e^{'}\overrightarrow{n}$)p Reaction," *Phys. Rev. Lett.*, vol. 83, no. 2, pp. 276–279, 1999.

[40] C. Sfienti, H. Merkel et al., "DFG Neutron Detector Proposal," 2013, unpublished.

[41] M. Andrew, "128 channel waveform sampling digitizer/readout in the TOP counter for the Belle II upgrade," *PoS(TIPP2014)*, no. 171, 2014.

[42] G. Varner, "Deep sampling CMOS Digitizers," in *Picosecond timing Workshop*, 2010, http://indico.cern.ch/event/114351/contribution/16/material/slides/0.pdf.

[43] T. Aumann, "Technical Report for the Design, Construction and Commissioning of NeuLAND: The High-Resolution Neutron Time-of-Flight Spectrometer for R^{3}B," 2011. [Online]. Available: http://www.fair-center.de/fileadmin/fair/publications_exp/NeuLAND-TDR-Web.pdf

[44] K. Koch, "A New Multi Channel Front-End Board for TOF Experiments with Excellent Timing Resolution ," 2004. [Online]. Available: https://www-alt.gsi.de/informationen/wti/library/scientificreport2004/PAPERS/INSTMETH-12.pdf

[45] ——, "TRIPLEX, an Upgrade for the TacQuila System," 2010. [Online]. Available: http://controls.gsi.de/informationen/wti/library/scientificreport2010/PAPERS/PHN-IS-EE-07.pdf

[46] Advanced Laser Diode Systems A.L.S. GmbH, "Picosecond Injection Laser (PiLas)," 2003. [Online]. Available: http://www.alsgmbh.com/

[47] Hamamatsu Photonics K. K, "Photomultipliers Tubes. Basic and Applications," 2007. [Online]. Available: https://www.hamamatsu.com/resources/pdf/etd/PMT_handbook_v3aE.pdf

[48] PHOTONIS USA Pennsylvania, Inc., "Photo Detector XP85012," 2012. [Online]. Available: http://www.photonis.com/attachment.php?id_attachment=40

[49] A. Lehman et al., "Systematic studies of micro-channel plate PMTs," *Nucl. Instr. Meth.*, no. A639, pp. 144–147, 2011.

[50] "ROOT Data Analysis Framework." [Online]. Available: https://root.cern.ch

[51] C. Rosner, "Charakterisierung des optischen Systems und der Ausleseelektronik fr den Barrel-DIRC Detektor an PANDA," Master's thesis, Johannes Gutenberg-Universität Mainz, 2013.

[52] E. H. Bellamy et al., "Absolute calibration and monitoring of a spectrometric channel using a photomultiplier," *Nucl. Instr. Meth.*, no. 339, pp. 468–476, 1994.

[53] "Particle Data Group," 2014. [Online]. Available: http://pdg.lbl.gov/

[54] William R. Leo, *Techniques for Nuclear and Particle Physics Experiments*. Springer Science & Business Media, 1994.

[55] T. Orita, "A new pulse width signal processing with delay-line and non-linear circuit (for ToT)," *Nucl. Instr. Meth.*, no. A648, pp. 24–27, 2011.

[56] C. Ugur et al., "264 Channel TDC Platform Applying 65 Channel High Precision (7.2 psRMS) FPGA Based TDCs," *IEEE*, 2013.

[57] "TRB3 Manual," 2014. [Online]. Available: http://jspc29.x-matter.uni-frankfurt.de/docu/trb3docu.pdf

[58] J. Kalisz, "Review of methods for time interval measurements with picosecond resolution," *Metrologia*, no. 41, p. 17, 2004.

[59] C. Ugur et al., "Implementation of a High Resolution Time-to-Digital Converter in a Field Programmable Gate Array," *Proceedings of Science (Bormio 2012)*, 2012. [Online]. Available: http://pos.sissa.it/archive/conferences/160/015/Bormio2012_015.pdf

[60] C. Ugur et al., "A 16 channel high resolution (<11 ps RMS) Time-to-Digital Converter in a Field Programmable Gate Array," *JINST*, no. 7, 2012.

[61] E. Oberla et al., "A 15 GSa/s, 1.5 GHz bandwidth waveform digitizing ASIC," *Nucl. Instr. Meth.*, no. A735, 2014.

[62] S. Ritt, "The role of analog bandwidth and S/N in timing, talk at The Factors that Limit Timing Resolution in Photodetectors, University of Chicago," in *The Factors that Limit Time Resolution in Photodetectors, Chicago*, 2011.

[63] F. Anghinolfi et al., "Nino, an ultra-fast, low-power, front-end amplifier discriminator for the time-of-flight detector in alice experiment," *Nucl. Instr. Meth.*, no. A533, pp. 183–187, 2004.

[64] "CERN Knowledge Transfer Webpage: NINO." [Online]. Available: http://knowledgetransfer.web.cern.ch/technology-transfer/external-partners/nino

[65] M. Piccini, "The NA62 RICH Detector," in *IEEE Nuclear Science Symposium*, 2009.

[66] S. Riordan et al., "Hall A Annual Report 2012," *ArXiv*, no. 1302.4324v1, 2013.

[67] M. Despeisse, "Multi-Channel Amplifier-Discriminator for Highly Time-Resolved Detection," *IEEE Transactions on Nuclear Science*, vol. 58, no. 1, 2011.

[68] Texas Instruments, "1.8 GHz, low distortion, current-feedback amplifier." [Online]. Available: http://www.ti.com/lit/ds/symlink/ths3201.pdf

[69] R. Mancini, editor in chief, of Texas instruments, "Op amp for everyone," 2002. [Online]. Available: http://e2e.ti.com/cfs-file.ashx/__key/

telligent-evolution-components-attachments/00-18-01-00-01-20-34-88/op-amps-for-everyone.pdf

[70] "Heaviside Step Function, Wolfram Math Word." [Online]. Available: http://mathworld.wolfram.com/HeavisideStepFunction.html

[71] "Levcon, level converter, gsi, darmstadt." [Online]. Available: https://www.gsi.de/work/organisation/wissenschaftlich_technologische_abteilungen/experiment_elektronik/elektronik_entwicklung/digitalelektronik/module/sonstige/levcon.htm

[72] "Go4." [Online]. Available: http://go4.gsi.de

[73] M. Cardinali et al., "Frontend electronics for high-precision single photoelectron timing using FPGA-TDCs," *Nucl. Instr. Meth.*, no. A766, pp. 231–234, 2014.

[74] K. Aulenbacher et al., "The Design of a Cascaded 800 MeV Normal Conducting C.W. Racetrack Microtron," *Nucl. Instr. Meth.*, no. A391, p. 498, 1997.

[75] "Mami-b accelerator webpage." [Online]. Available: http://portal.kph.uni-mainz.de/B1/accelerator.php

[76] Heraeus, "Quartz Glass for Optics, Data and Properties, $HQS.MO\_01.0/E/04.2013$," 2013.

[77] M. I. Ferretti Bondy, "Charakterisierung eines Prototyp Detektors zur Teilchenidentifikation des PANDA-Experiments," Master's thesis, Johannes Gutenberg-Universität Mainz, 2012.

[78] R. Hohler, "Prototyp-Radiatoren eines Barrel-DIRC für das PANDA-Experiment," Ph.D. dissertation, Goethe-Universität Frankfurt, 2011.

[79] The ROOT Team (CERN), "TH2Poly library." [Online]. Available: https://root.cern.ch/root/html/TH2Poly.html

[80] F. Uhlig et al., "Breakthrough in the lifetime of microchannel plate photomultipliers," *Nucl. Instr. Meth.*, no. A, in Press, 2014.

[81] S. Hirose et al., "Performance of the MCP-PMT for the Belle II TOP counter in a magnetic field," *Nucl. Instr. Meth.*, no. A766, pp. 163–166, 2014.

[82] T. Hayakawa et al., "Performance tests of a full scale prototype of the Belle II TOP counter with cosmic muons and 2.1 GeV/c positron beam," *Nucl. Instr. Meth.*, no. A766, pp. 255–258, 2014.

[83] B. S. Schlimme, "Messung des elektrischen Neutron-Formfaktors in der Reaktion ^{3}He(e,e'n)pp bei $Q^2 = 1.58$ (GeV/c)^2," Ph.D. dissertation, Johannes Gutenberg-Universität Mainz, 2012.

[84] Private communication with M. Schoth (November 2014).

[85] Private communication with W. Lauth (April 2015).

[86] M. Moszynski and B. Bengtson, "Status of timing with plastic scintillation detectors," *Nucl. Instr. Meth.*, no. 158, pp. 1–31, 1979.

[87] USCMS collaboration, "Forward Physics with Rapidity Gaps at the LHC," *JINST*, vol. 4, no. P10001, 2009.

[88] M. G. Albrowa et al., "Quartz Cherenkov Counters for Fast Timing: QUARTIC," *JINST*, vol. 7, no. P10027, 2012.

[89] P. M. Duarte, "QUARTIC: an ultra-fast time-of-flight counter," Master's thesis, The University of Texas at Arlington, 2007.

[90] Private communication with A. Lehmann (December 2014).

[91] M. Dickescheid, "Fast light acquiring start hodoscope," Master's thesis, Johannes Gutenberg-Universität Mainz, 2015, in progress.

[92] C. Gotti, M. Fiorini et al., "CLARO-CMOS: a fast, low power and radiation-hard front-end ASIC for single-photon counting in 0.35 micron CMOS technology," *Proceedings of Science (TIPP 2014)*, 2014. [Online]. Available: http://pos.sissa.it/archive/conferences/213/177/TIPP2014_177.pdf

[93] C. Ugur et al., "TRB3 Platform for Time, Amplitude and Charge Digitisation," in *TIPP 2014 International Conference, Amsterdam*, 2014, https://indico.cern.ch/event/192695/session/10/contribution/241.

[94] J. Michel et al., "FPGA based read-out systems," in *FAIR 2014 International Conference, Worms*, 2014, https://indico.gsi.de/contributionDisplay.py?sessionId=25&contribId=161&confId=2443.

List of Figures

1.1 Block diagram of frontend signal processing. A detector produces short tension (or current) pulses which are preprocessed by the FEE and then digitized by the readout electronics (e.g. a TDC). 2

1.2 Layout of the PANDA detector consisting of a target spectrometer, surrounding the interaction region, and a forward spectrometer to detect particles emitted in the forward region. The antiproton beam enters the apparatus from the left side [8]. . . 6

1.3 Schematic cross section of the PANDA TS. Both, the Barrel DIRC and the Endcap DIRC are highlighted (in blue and red, respectively) and their polar acceptance is indicated by the dashed lines. The STT adjoins the Barrel DIRC on the inside and the EMC on the outside. In the forward direction the GEM tracking detector and the Endcap EMC surround the Endcap DIRC [7]. 7

1.4 (a) Schematic of typical Cherenkov reference frames with respect to the particle path. (b) Schematic of a radiator bar illustrating the DIRC reference frame. The particle trajectory is shown as a line connected by dots; representative trajectories of Cherenkov photons are shown by lines with arrows [19]. 8

1.5 Schematic drawing of the Barrel DIRC baseline design. The focussing optics using high-refractive index material is shown in the inset. [7] 11

1.6 The A1 hall. The three big spectrometers A (red), B (blue), C (green) are visible. The thin upstream beam pipe comes in from the right [29]. 13

1.7 Existing data on neutron FFs, G_E^n (a) and G_M^n (b) [30]. 15

1.8 (a) GEANT4 simulation of the neutron detector hit by a proton [40]. (b) schematic of the A1 spectrometer arrangement. The grey square shows a possible position of the A1 NDet (not drawn to scale). 17
1.9 Picture of one bar end with three WLSs. 18

2.1 (a) 3D CAD-Model of the light-tight box. (b) photo of the box interior with laser collimator and MCP-PMT (plus optional electronics) fixed on the optical breadboard. 24
2.2 (a) schematic structure of an MCP. (b) multiplication process along an MCP channel; an electron hits the channel wall and produces a cascade proportional to the voltage V_D up the output electrode [47]. 26
2.3 Schematic structure of an MCP-PMT. A photon (purple) hits the photocathode and produces an electron which generates an avalanche of secondary electrons which is collected by the anodes matrix. 27
2.4 Design of the Planacon XP85012 MCP-PMT (units: mm): the 8×8 pixel matrix is shown in the top view. The output pins are grouped into four columns with 2 mm pitch [48]. 28
2.5 Typical spectral response (a) and gain curve (b) of the XP85012 MCP-PMT [48]. 28
2.6 Typical MCP-PMT response for SP signals (overlay of 100 pulses) [51]. 29
2.7 Amplitude spectrum of SP events [51]. 30
2.8 Logarithmic charge spectrum of the MCP-PMT under SP laser illumination. The data have been fitted with Eq. 2.10 and they show on average 0.36 photoelectrons per event [51]. . . . 33
2.9 Schematic view of an MCP-PMT signal. In this model the pulse shape is considered as an isosceles triangle. 34
2.10 Charge profile as function of the signal amplitude. The linear fit demonstrates the equivalence between the two quantities [51]. 35
2.11 ToT as a function of the signal charge. Curve is a fit according to Eq. 2.13 where the red part indicates the fit range [51]. . . 36
2.12 Time-walk effect for threshold triggering in case of MCP-PMT-like signals. 37
2.13 Profile of the arrival time as function of the deposited charge. A fit with Eq. 2.15 is performed (red line). 37

2.14 Scatter plot of the arrival time as function of the ToT for an MCP-PMT under SP conditions (colors according to the intensity). 38
2.15 Profile of Fig. 2.14. A linear fit shows a good agreement between the data and the triangle-like model for MCP-PMT signals. 39
2.16 Schematic view of the cosmic ray setup. 40
2.17 Logarithmic charge spectrum of the XP2900 under SP laser illumination. The data are fit with Eq. 2.10 and show an average of 0.39 photons per event. 41
2.18 (a) response of the PMT to MIP signals (overlay of 100 waveforms). (b) intensity chart of the same overlay. 42
2.19 Simple exponential model for scintillation signals. 43
2.20 Charge distribution for MIPs as function of the pulse amplitude. The quadratic polynomial shows negligible impact of $p2$ proving a good linearity. 43
2.21 Charge distribution for MIPs as function of the pulse ToT. The data agree with the exponential model of Eq. 2.21. Within the grey lines also a simple straight line can be used for the fit. 45
2.22 MIP charge spectrum of the PMT. 45

3.1 Block diagram of the FEE concept. The pulse $V(t)$ produced by a detector is processed by the FEE which encodes the information with a time signal in LVDS logic. The TRB3 acquires the FEE output with a precise TDC. 48
3.2 Photo of the TRB3 board. Four peripheral FPGAs (red) can be programmed as TDC or hub. A central FPGA (light blue) controls the board and acts as a CTS unit. Several connectors allows high versatility. Two ethernet sockets provide input and output trigger connections. 48
3.3 Tapped delay line method [56]. 50
3.4 Synchronization time precision between the different FPGAs. . 52
3.5 Synchronization precision between FPGA 1 & 4 **(a)** and 2 & 4 **(b)**. The double peak structure in **(b)** is caused by the power supply close to FPGA 2. 52
3.6 Synchronization precision between FPGA 1 of the two TRB3s. . 53
3.7 Functional block diagram for one channel of the NINO chip [63]. 55
3.8 Top view of the discriminator PCB (8 cm long, 6 cm wide). . . 56
3.9 Preamplifier schematics for one channel. A 50 Ω termination is applied before the NINO chip. 57

3.10 Preamplifier Add-on and discriminator cards connected. 58
3.11 Amplitude response of the preamplifier Add-on card to MCP-PMT-like pulser signals. 59
3.12 FEE feedback to signal inputs at different threshold levels, in agreement with the model of Eq. 3.3. Linear fits denote the characteristic slope of the circuit from which t_{amp} is extracted. 61
3.13 Correlation of signal amplitude and individual threshold voltage setting for a single channel. 61
3.14 NINO response to a square pulse with different widths. The saturation of the FEE (preamplifier and discriminator cards) occurs at 13 pC. 62
3.15 NINO ToT response as function of the input charge generated by a pulse generator. 63

4.1 Schematics for the full readout test using fast laser setup calibrated to SP. 66
4.2 Intensity plot of the MCP-PMT with the laser spot focussed in the centre: (a) at ND 5.0 (approximately 500,000 events), (b) at ND 3.0 (approximately 50,000 events). 67
4.3 Intensity plot of the MCP-PMT with the laser defocussed laser spot around the centre. This image was produced using Go4, another analysis software package available for the TRB3 [72] . 68
4.4 Scatter plot of the photon arrival time as a function the channel number. 69
4.5 Time-over-threshold spectrum of a single MCP-PMT channel at a threshold level of 1.9 V. 70
4.6 Time-over-Threshold response to MCP-PMT signals as a function of the NINO threshold. 70
4.7 Detection efficiency at different threshold levels. 71
4.8 Arrival time of photons as function of measured ToT [73]. . . . 72
4.9 Profile of Fig. 4.8. A linear fit is applied in a range containing 90% of the events. 73
4.10 Time spectrum before (a) and after (b) time-walk correction. Back-scattered electrons inside the MCP-PMT generate the tail on the right. 74
4.11 Time resolution optimization by varying the slope parameter (m) of equation 4.6. 75

4.12 Signal characterization using cosmics. A scintillator bar is readout with a single channel PMT and the full electronics chain. Two small scintillator strips provide the trigger. 76
4.13 Time spectrum of cosmic muons traversing a scintillator bar measured with the full readout chain. The peak at 0 ns belongs to the trigger reference channel. 77
4.14 Time over threshold spectrum with (red) and without (blue) preamplifier card. After-pulses caused by saturation of the discriminator produce the peak at 12 ns. 78
4.15 Scatter plot of the arrival time of muons as a function of the measured time over threshold. The structure at positive time (>20 ns) is due to charge saturation phenomena of the discriminator. 79
4.16 Experimental setup with a ^{90}Sr source. 80
4.17 Left-right timing differences at different positions of the radioactive source. The dashed lines belong to intermediate positions (18 cm in black and 48 cm in purple). 80
4.18 Correlation between time difference and position of the strontium source along the bar. A linear distribution is used for the fit. 81

5.1 MAMI-B accelerator floor plan [75]. The arrow indicates the test area of the DIRC prototype. 84
5.2 Coincidence rate of trigger scintillators over an 11 hour period. 85
5.3 Schematic view of the DIRC prototype setup and rear view of the expansion volume. 86
5.4 Normalized frequency of TRB3 error conditions. 87
5.5 Time spectrum for about 2.5×10^6 events using all the 512 TDC channels. 88
5.6 ToT response to MCP-PMT signals as a function of the threshold. 89
5.7 Measured ToT over an extended period of data taking. The trend shows a good overall stability. 89
5.8 Observed Cherenkov pattern at different incidence angles and corresponding simulations. The plots on the left are an overlay of two million events. The six boxes on the simulations indicate the possible positions of the MCP-PMTs on the expansion volume. 91

5.9 Observed Cherenkov pattern at 57°. Monte Carlo simulation is shown in grey. 92
5.10 Number of hit pixels at different incidence angles. 92
5.11 (a) event display at 120°. (b) schematic view of the radiator bar and the Cherenkov light path. 93
5.12 Photon arrival time for one MCP-PMT channel at prototype angle of 60° and 120°. 94
5.13 Scatter plot of the ToT for two neighbouring pixels. 95
5.14 Measured timing resolution σ_t between neighbouring MCP-PMT pixels: uncorrected data (red), corrected data (blue). 96
5.15 Optimization for the slope parameter of the time walk correction. The red and blue dots show the result for two different pixels in two MCP-PMTs. 97
5.16 Measured σ_{FEE} over a extended period of data taking. 97
5.17 Average ToT for FEE events at different MCP-PMT gains. The threshold value was set to 1.3 V. 99
5.18 Comparison of the lifetime for different MCP-PMTs (XP85112 with ALD coating in blue) [80] 99
5.19 Measured timing resolution σ_t between different MCP-PMTs: uncorrected data (red), corrected data (blue). 100
5.20 Single pixel time spectrum generated by a ray-tracing Monte Carlo simulation. A Gaussian fit is applied to the data. 101
5.21 Top view of one layer of the neutron detector prototype. 64 scintillator bars with three WLSs each are readout with two 64 ch MAPMT (three fibres per pixel). Commercial optical connectors and clear fibers ensure the connection of the WLSs to the MAPMT. 104
5.22 Lateral and top view of the experimental area (not drawn to scale). A, B and C indicate the spectrometer positions. Spec. B was used for the coincidence measurement with the NDet. . . 105
5.23 Normalized frequency of TRB3 error conditions. 106
5.24 Time spectrum of all the channels over 10 minutes data taking. 107
5.25 ToT response as a function of the TDC channels after threshold adjustment. 108
5.26 ToT response as a function of the relative time to the A1 trigger. The structures between [-500,-400] ns and [-400,-300] ns belong to MIPs and neutrons, respectively, while the continuous band with ToT$\approx$ 12 ns is interpreted as background signals. 109

5.27 Result of the background suppression algorithm applied to the data shown in Fig. 5.26. 110
5.28 ToT spectra of raw and suppressed background events. 110
5.29 ToT response to different particle species. 111
5.30 ToT response of the scintillator bars along the NDet prototype. 111
5.31 Simulation of the deposited energy of neutrons per layer [84]. In the test experiment the kinetic energy of neutrons was approximately 100 MeV. 112
5.32 Timing resolution of the bar for neutrons. 113
5.33 Number of hit bars per event for MIPs and neutrons. 114
5.34 Reconstructed rate for a high beam current setting (approximately 10 μA). 115

6.1 (a) schematic view of the QUARTIC design used for the test experiment. (b) Gain uniformity of the used MCP-PMT [90]. The black lines delimit the pixels connected to radiator bars. . 118
6.2 Overlay of 20,000 events in the two fast counter units studied in the test experiment. The arrows indicate the beam directon. 120
6.3 Average ToF for 5 bar combinations. The Gaussian fit is used to calculate the timing resolution. 120
6.4 Photo of the PaDiWa card. 121
6.5 Scatter plot of the arrival time of photons as a function of ToT. 122
6.6 PaDiWa time spectrum after time walk correction. 123

A.1 Scatter plot showing the amplitude as function of the charge for an MCP-PMT under SP conditions (colors according to the intensity). The red spot at low charge is produced by pedestal noise [51]. 131
A.2 Scatter plot showing the amplitude as function of the charge for an MCP-PMT with NDF 4.0 (colors according to the intensity) [51]. 132
A.3 Profile of the previous plot fit with a straight line [51]. 132
A.4 Scatter plot showing the amplitude as function of the charge for an MCP-PMT with NDF 3.0 (colors according to the intensity) [51]. 133
A.5 Profile of the previous plot fit with a straight line [51]. 133
A.6 Scatter plot showing the amplitude as function of the ToT at the threshold level of 1 mV (a), 2 mV (b) [51]. 134

A.7 Scatter plot showing the amplitude as function of the ToT at the threshold level of 3 mV (a) and 4 mV (b) [51]. 135
A.8 Intensity plot of charge as function of ToT. The threshold on the amplitude is 2 mV. 136

B.1 Synchronization precision between FPGA 1 & 2, FPGA 1 & 3, FPGA 2 & 3 and FPGA 3 & 4. 137
B.2 Layout drawing of the the discriminator. 138
B.3 *1st part*: discriminator board schematics. 139
B.4 *2nd part*: discriminator board schematics. 140
B.5 *3rd part*: discriminator board schematics. 141
B.6 *4th part*: discriminator board schematics. 142
B.7 Top and bottom view of the layout drawing for the FEE mother board. 143
B.8 Layout drawing of the preamplifier. 144
B.9 *1st part*: preamplifier board schematics. 144
B.10 *2nd part*: preamplifier board schematics. 145
B.11 *3rd part*: preamplifier board schematics 145

List of Tables

1.1 Summary of the Barrel DIRC and the corresponding FEE requirements. 12
1.2 Summary of the NDet and corresponding FEE requirements. . . 18

3.1 Main characteristics of the NINO chip [63]. 55

4.1 Summary of the timing contributions and resolutions. 75

5.1 (a) MCP-PMT high voltages for a gain $G \approx 10^6$. The FPGA numbering follows the scheme on Fig. 5.3. (b) MCP-PMT to TRB3 channel mapping. 87
5.2 Average number of detected photons at different angles. . . . 90
5.3 Timing resolution σ_{FEE} and expected input charge for the discriminator card at different MCP-PMT gains. 98
5.4 Summary of the measured timing resolutions. 101